GEORGIA INSTITUTE OF TECHNOLOGY

OFFICE OF CONTRACT ADMINISTRATION

RESEARCH PROJECT INITIATION

Date: September 29, 1975

Project Title: High Capacity Laser Holographic Data Storage

Project No: E-21-667

Principal Investigator: T. K. Gaylord/W. R. Callen

Sponsor: National Science Foundation

Agreement Period: From 10/1/75 Until 3/31/77

12 months budget period plus 6 months for submission of required reports, etc.

Type Agreement: Grant No. ENG75-14456

Amount: $34,600 NSF
5,000 GIT E-21-337
$39,600 Total

Reports Required:

Annual Letter Technical; Final Report

Sponsor Contact Person (s):

Administrative Matters
thru OCA
Mr. Gaylord L. Ellis
Grants Officer
National Science Foundation
Washington, D. C. 20550
(202) 632-5965

Assigned to: Electrical Engineering

COPIES TO:

- Principal Investigator (2)
- School Director
- Dean of the College
- Director, Research Administration
- Director, Financial Affairs (2)
- Security-Reports-Property Office
- Patent Coordinator
- Library
- Rich Electronic Computer Center
- Photographic Laboratory
- Project File
- Other

RA-3 (9-75)

GEORGIA INSTITUTE OF TECHNOLOGY
OFFICE OF CONTRACT ADMINISTRATION

SPONSORED PROJECT TERMINATION

Posted

Date: April 28, 1977

Project Title: *High Capacity Laser Holographic Data Storage*

Project No: *E-21-667*

Project Director: *Dr. T. K. Gaylord/Dr. W. R. Callen*

Sponsor: *National Science Foundation*

Effective Termination Date: *3/31/77*

Clearance of Accounting Charges: *3/31/77*

Grant/Contract Closeout Actions Remaining:

_ Final Invoice and Closing Documents
X Final Fiscal Report
_ Final Report of Inventions
_ Govt. Property Inventory & Related Certificate
_ Classified Material Certificate
_ Other _____

Assigned to: *EE* (School/Laboratory)

COPIES TO:

Project Director
Division Chief (EES)
School/Laboratory Director
Dean/Director—EES
Accounting Office
Procurement Office
Security Coordinator (OCA) ✓
Reports Coordinator (OCA)
Library, Technical Reports Section
Office of Computing Services
Director, Physical Plant
EES Information Office
Project File (OCA)
Project Code (GTRI)
Other _____

CA—4 (3/76)

E-21-667

GEORGIA INSTITUTE OF TECHNOLOGY
SCHOOL OF ELECTRICAL ENGINEERING
ATLANTA, GEORGIA 30332

TELEPHONE: (404) 894-2901

September 14, 1976

Dr. Elias Schutzman
Engineering Division
1800 G Street, N.W.
National Science Foundation
Washington, D. C. 20550

Subject: Annual Technical Letter for
NSF Grant No. ENG75-14456
"High Capacity Laser Holographic Data Storage"

Dear Dr. Schutzman:

Please accept this Annual Technical Letter for the above grant. This is a brief interim report and includes reprints of our grant publications. A comprehensive Final Report will be sent to you about five months from now.

Progress Summary (September 1975 to September 1976)

The primary accomplishments during the last year are represented in the attached three publications. These papers describe recent experimental and theoretical results that have greatly improved the understanding of the physical processes in and the potential of volume holographic data storage and retrieval in electro-optic crystals. A most important extra dividend from this work has been the establishment of diagnostic procedures for determining the suitability of given electro-optic crystals to fulfill a specific application requirement (e.g. data recording, modulator, grating coupler, etc.)

The paper "Unified approach to the formation of phase holograms in ferroelectric crystals" describes in detail, from initial writing to saturation, the formation of holographic refractive-index gratings in electro-optic crystals. This shows in specific terms the roles of drift and diffusion of photoexcited electrons in producing internal electric fields that modulate the index of refraction.

The article "Use of dynamic theory to describe experimental results from volume holography" explains, for the first time, the complex interaction of the light waves (incident and diffracted) inside an electro-optic grating. The incident beam is diffracted inside the crystal and the resultant two beams interfere with each other producing

changes that may either add to or subtract from the existing holographic grating. These effects are extremely important in data hologram recording and in the fabrication of gratings for use in integrated optics applications.

The paper "Determination of physical parameters and processes in hologram formation in ferroelectrics" describes how the results of simple holographic experiments may be used to establish the parameters and processes occurring in a particular electro-optic crystal sample. This information is useful in that a material specimen may be analyzed with routine measurements to determine whether it is suitable for a particular application. This greatly relieves the need to fabricate an actual device in order to test it.

Personnel

The following personnel have been or now are involved in one or more aspects of this grant. Many of these people were supported with State of Georgia funds. Faculty involved are: C. O. Alford, W. R. Callen, T. K. Gaylord, G. S. Smith, and H. C. Viljoen (University of Stellenbosch). Graduate students involved are: D. E. Duncan, R. Magnusson, J. A. Maynard, S. F. Su, and J. E. Weaver. Undergraduate students involved are: E. Hammonds and C. Nicklaw. A high school student involved was: P. Small (NSF Summer Institute student).

Sponsor Visits

On August 5, 1976, Dr. Charles Polk, Director of the Engineering Division of NSF visited Georgia Tech and reviewed the experimental and theoretical work being performed on this grant.

Award

The "Outstanding Young Faculty Research Award" of the Georgia Tech chapter of Sigma Xi was awarded to Thomas K. Gaylord. This was specifically given for the published papers "Unified approach to the formation of phase holograms in ferroelectric crystals" and "Use of dynamic theory to describe experimental results from volume holography."

If any further information is needed before the Final Report, please contact me and I will be happy to supply it to you.

Very sincerely,

Thomas K. Gaylord
Associate Professor

TKG:da
Enclosures: 3 copies each of
J. Appl. Phys. 46, 5208 (1975)
J. Appl. Phys. 47, 190 (1976)
J. Appl. Phys. 47, 2757 (1976)

E-21-667

GEORGIA INSTITUTE OF TECHNOLOGY
ATLANTA, GEORGIA 30332

OFFICE OF
THE DIRECTOR OF
FINANCIAL AFFAIRS

June 1, 1977

Division of Grants and Contracts
National Science Foundation
Washington, D. C. 20550

Gentlemen:

Enclosed in triplicate is the final fiscal report for Grant Number ENG75-14456.

If you have any questions or desire additional information, please let us know.

Sincerely,

Evan Crosby
Associate Director

EC/mg

cc: Dr. T. K. Gaylord
Dr. W. R. Callen
Dr. D. T. Paris
Mr. E. E. Renfro
Mr. A. H. Becker
File E-21-667

NATIONAL SCIENCE FOUNDATION
Washington, D.C. 20550

RESEARCH GRANT BUDGET & FISCAL REPORT

Form Approved
OMB No. 99-R0013

INSTITUTION AND ADDRESS	NSF PROGRAM	GRANT PERIOD
Georgia Institute of Technology Atlanta, Georgia	Electrical & Optical Communications	*from* 10/1/75 *to* 3/31/77 REPORTING PERIOD *from* 10/1/75 *to* 3/31/77 **

GRANT NUMBER	BUDGET DUR. (MOS.)	PRINCIPAL INVESTIGATOR(S)	GRANTEE ACCOUNT NUMBER
ENG75-14456	12	Gaylord & Callen	E-21-667

	NSF Funded Man Months			NSF AWARD BUDGET	CUMULATIVE GRANT EXPENDITURES *Do Not Round*
A. SALARIES AND WAGES	Cal.	Acad.	Summ.		
1. Senior Personnel					
a. 2 (Co)Principal Investigator(s)		3	4	$ 13,309	
b. Faculty Associates					
Sub-Total				$ 13,309	$ 14,888.00*
2. Other Personnel (Non-Faculty)					
a. Research Associates—Postdoctoral					
b. Non-Faculty Professionals					
c. 1 Graduate Students				1,600	
d. Pre-Baccalaureate Students					
e. 1 Secretarial—Clerical				500	
f. 1 Technical, Shop, and Other				500	
TOTAL SALARIES AND WAGES				$ 15,909	$ 15,438.00
B. STAFF BENEFITS IF CHARGED AS DIRECT COST				1,395	1,346.42
C. TOTAL SALARIES, WAGES, AND STAFF BENEFITS (A + B)				$ 17,304	$ 16,784.42
D. PERMANENT EQUIPMENT					
As listed in proposal budget				5,000	2,267.55
E. EXPENDABLE EQUIPMENT AND SUPPLIES				1,500	2,735.79
F. TRAVEL 1. DOMESTIC (INCLUDING CANADA)					-
2. FOREIGN					-
G. PUBLICATION COSTS				500	2,291.00
H. COMPUTER COSTS IF CHARGED AS DIRECT COST					-
I. OTHER DIRECT COSTS					
					-
J. TOTAL DIRECT COSTS (C through I)				$ 24,304	$ 24,078.76
K. INDIRECT COSTS					
65% of Salaries & Wages	68% is the approved Overhead rate for the Grant Period.			10,341	10,497.84
L. TOTAL COSTS (J plus K)				$ 34,645	$ 34,576.60
M. AMOUNT OF THIS AWARD (ROUNDED)				$ 34,600	
N. CUMULATIVE GRANT AMOUNT				$	
O. UNEXPENDED BALANCE (N. BUDGET MINUS L. EXPENDITURE)					$ 23.40

REMARKS: Use extra sheet if necessary

* 3.64 Cal. Man Months
2.43 Acad. Man Months
1.26 Summ. Man Months
7.33

** No obligations were incurred outside the grant period of 10/1/75 to 3/31/77.

SIGNATURE OF PRINCIPAL INVESTIGATOR	TYPED OR PRINTED NAME	DATE
[signature]	T. K. Gaylord/W. R. Callen	5/30/77

I CERTIFY THAT ALL EXPENDITURES REPORTED ARE FOR APPROPRIATE PURPOSES AND IN ACCORDANCE WITH THE AGREEMENTS SET FORTH IN THE APPLICATION AND AWARD DOCUMENTS

SIGNATURE OF AUTHORIZED OFFICIAL	TYPED OR PRINTED NAME & TITLE	DATE
[signature]	Evan Crosby, Associate Director of Financial Affairs	5/31/77

FOR NSF USE ONLY

Organ. Code	F.Y.	Fund ID	Prog. Code	Ob. Class	O/Dres.	Award No.	Amd.	Inst. Code	Unexpended Balance	Trans.	Lot
									$		

NSF Form 98, May 1975

SUPERSEDES JULY 1971 EDITION WHICH MAY BE USED UNTIL SUPPLY EXHAUSTED

E-21-667

NATIONAL SCIENCE FOUNDATION
Washington, D.C. 20550

SUMMARY OF COMPLETED PROJECT

Form Approved
OMB No. 99R0013

Please read instructions on reverse carefully before completing this form.

1. INSTITUTION AND ADDRESS	2. NSF PROGRAM	3. GRANT PERIOD
Georgia Institute of Technology	Engineering Division	from 9/1/75 to 3/31/77

4. GRANT NUMBER	5. BUDGET DUR. (MOS)	6. PRINCIPAL INVESTIGATOR(S)	7. GRANTEE ACCOUNT NUMBER
ENG75-14456	18	T. K. Gaylord	E-21-667

8. SUMMARY (Attach list of publications to form)

The concept of very high capacity optical storage and retrieval of information is based on the fact that data can be stored in either two dimensions (on a surface) or in three dimensions (in a volume), and that for idealized conditions at visible wavelengths, the storage capacity is 4×10^8 bits/cm^2 in two dimensions and 8×10^{12} bits/cm^3 in three dimensions. High-capacity storage in volume by holographic techniques was the focus of this research grant. While of fundamental importance, this was found to be but one aspect of volume holography.

Much basic scientific information has resulted from this research. This is expanded in detail in the publications given on the attached list. This information is having an increasing effect on integrated optics and optical communications through its impact on material parameter evaluation and performance characterization of optical devices for modulation, distributed feedback, reflecting, filtering, and coupling.

The potential characteristics of volume holographic systems identified are numerous and interrelated. Some of these are:

(1) High Capacity Storage. Vast quantities of data (~10^{13} bits) may potentially be stored and randomly accessed using volume holography. This mass store may be archival, read-mostly, fast recording, or fast read-write-erase.

(2) Random Access. Using the laser holographic technique, all stored information is randomly accessible.

(3) Two-Dimensional Format. Due to the nature of optical holography, the data is inherently stored in a two-dimensional format. This may be an image (two-dimensional analog data) or a data page (two-dimensional digital data).

(4) High Transfer Rate. The holographic reconstruction process reporduces an entire page with each read-out positioning of the laser beam.

(5) Multi-Port Configuration. Entirely new processing architectures are possible with holographic optical memories due to their multi-port capability. There are several types of use for a multi-port store. These include: record access systems, simultaneously shared memory processing, and parallel processing.

(6) Analog and Digital Storage. The same volume holographic storage system may simultaneously contain stored images (analog information) and store data pages (digital information).

(7) Analog Processing. A volume holographic system is uniquely useful in analog processing as a general complex two-dimensional filter for pattern recognition (correlation by vander Lugt filtering), feature extraction, image enhancement (such as deblurring), or other types of picture processing.

See Attached Page 1

9. SIGNATURE OF PRINCIPAL INVESTIGATOR/ PROJECT DIRECTOR	TYPED OR PRINTED NAME	DATE
[illegible]	Thomas K. Gaylord	4/8/77

(8) Digital Processing. It has recently been shown that logic operations may be performed between pages of digital data stored in a volume holographic storage and retrieval system. Thus, if each page contains 10^4 bits, there are effectively 10^4 operations performed in one operational cycle. This represents true optical parallel processing of two-dimensional digital data.

1. Gaylord, T. K., "Tensor description of physical properties of crystals," American Journal of Physics, vol. 43, no. 10, pp. 861-868, October 1975.

2. Su, S. F. and Gaylord, T. K., "Refractive index profiles and arbitrary-order diffraction efficiencies of lithium niobate holograms," Journal of the Optical Society of America, vol. 65, no. 10, pg. 1220, October 1975.

3. Magnusson, R. and Gaylord, T. K., "Application of dynamic theory to the description of experimental volume holography," Journal of the Optical Society of America, vol. 65, no. 10, pg. 1219, October 1975.

4. Maynard, J. A., Gaylord, T. K., and Rust, J. H., "Data acquisition system for laser Doppler velocimeters," Review of Scientific Instruments, vol. 46, pp. 1469-1473, November 1975.

5. Su, S. F. and Gaylord, T. K., "Unified approach to the formation of phase holograms in ferroelectric crystals," Journal of Applied Physics, vol. 46, pp. 5208-5213, December 1975.

6. Gaylord, T. K. and Linxwiler, J. N., "A method for calculating the Fermi energy and the carrier concentrations in semiconductors," American Journal of Physics, vol. 44, pp. 353-356, April 1976.

7. Gaylord, T. K., Weaver, J. E., and Callen, W. R., "A mobile, rigid, vibration-isolated optics demonstration platform," American Journal of Physics, vol. 43, pp. 310-311, March 1976.

8. Magnusson, R. and Gaylord, T. K., "Use of dynamic theory to describe experimental results from volume holography," Journal of Applied Physics, vol. 44, pp. 190-199, January 1976.

9. Su, S. F. and Gaylord, T. K., "Determination of physical parameters and processes in hologram formation in ferroelectrics," Journal of Applied Physics, vol. 47, pp. 2757-2758, June 1976.

10. Gaylord, T. K., "Optical memory systems," Optical Industry and Systems Directory Encyclopedia, Pittsfield, MA, Optical Publishing Co., pp. 198-203, 1976.

11. Gaylord, T. K., Magnusson, R., and Su, S. F., "Volume holographic recording and read-out in ferroelectrics," Journal of the Electrochemical Society, vol. 123, pg. 116C, March 1976.

12. Su, S. F. and Gaylord, T. K., "Refractive-index profile and physical process determination in thick gratings in electro-optic crystals," Applied Optics, vol. 15, pp. 1947-1952, August 1976.

13. Viljoen, H. C. and Gaylord, T. K., "An electronic system for optical shutter control," Review of Scientific Instruments, vol. 47, pp. 1133-1141, September 1976.

14. Su, S. F. and Gaylord, T. K., "Time evolution and refractive-index profiles of phase holograms in electro-optic crystals," Journal of the Optical Society of America, vol. 66, pg. 1084, October 1976.

15. Magnusson, R. and Gaylord, T. K., "Dynamically-induced refractive-index non-uniformities in electro-optic holographic gratings," Journal of the Optical Society of America, vol. 66, pg. 1084, October 1976.

16. Magnusson, R. and Gaylord, T. K., "Dynamically produced refractive-index variations with thickness of volume holograms in electrooptic crystals," Applied Optics, vol. 15, pp. 3021-3024, December 1977.

SCHOOL OF ELECTRICAL ENGINEERING
Georgia Institute of Technology
Atlanta, Georgia 30332

FINAL REPORT

PROJECT NO. E-21-667

HIGH CAPACITY LASER HOLOGRAPHIC DATA STORAGE

by

T. K. Gaylord

RESEARCH GRANT ENG75-14456

1 October 1975 to 31 March 1977

Performed for

NATIONAL SCIENCE FOUNDATION
Engineering Division
Electrical Sciences and Analysis Section
Washington, D.C. 20550

TABLE OF CONTENTS

I. ABSTRACT

A program of study of high capacity laser holographic data storage in electrooptic crystals was undertaken. This study focused on the problems associated with very high capacity storage (through multiple hologram superposition in volume), optical processing of holographic stored data, and the optically-induced physical processes occurring in electrooptic crystals.

A number of important problem areas were identified and then were experimentally and theoretically investigated. The results obtained may be broadly classified in four categories: 1) Optical memory systems, 2) Optically-induced physical processes, 3) Dynamic theory of hologram formation, and 4) Instrumentation. Thus it is seen that modern research in this area encompasses many diverse fields and that only through a unification of these is one able to understand holographic storage and processing.

Single hologram and multiple hologram recording experiments were performed using the experimental configuration shown in Fig. 1. Holograms were recorded and were analyzed at wavelengths of 488nm, 515nm, and 633nm.

These experimental results along with the various theoretical results obtained are presented in this report.

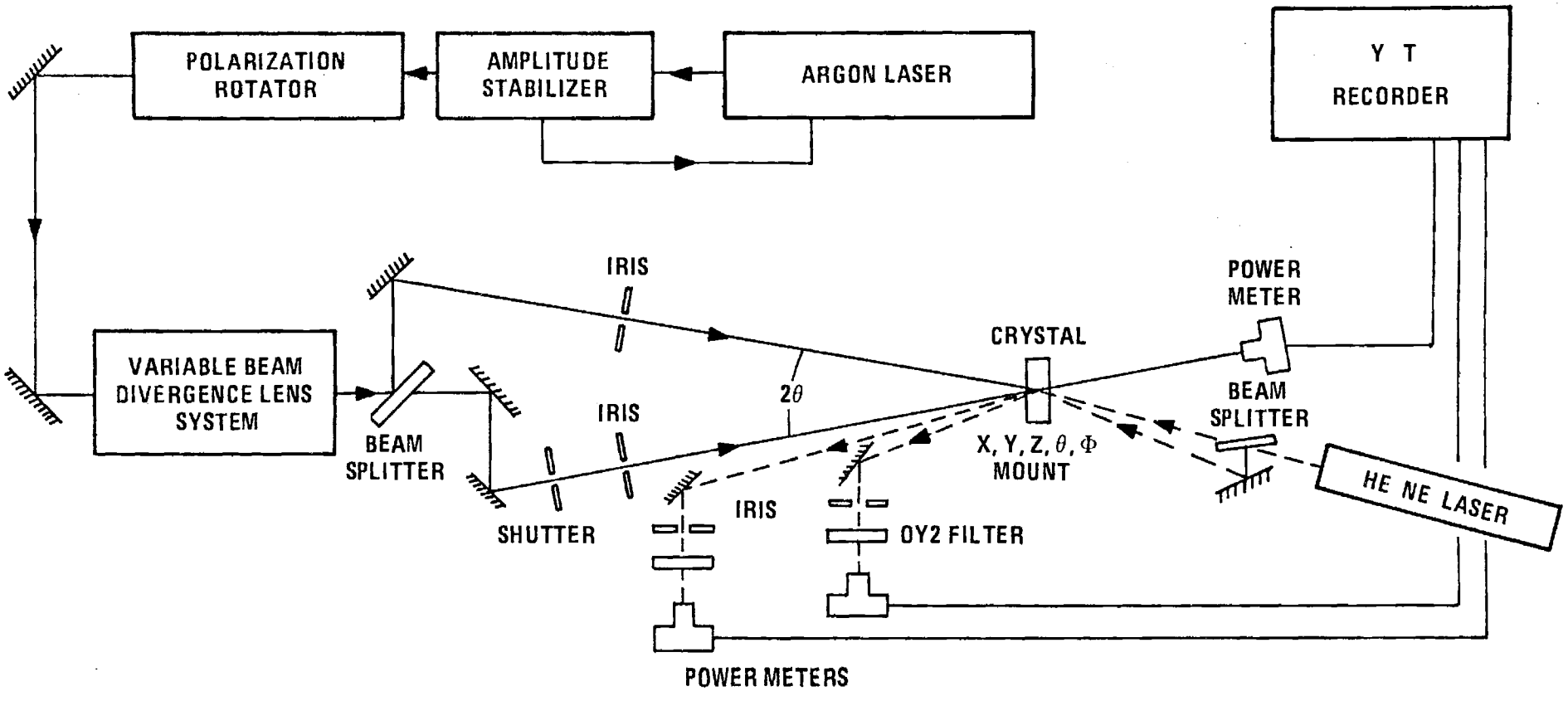

Figure 1 Experimental Configuration for Investigating Recording and Readout in Electro-Optic Crystals

II. POTENTIAL ENGINEERING APPLICATIONS

The concept of optical storage and retrieval of information received impetus from the work of P. J. van Heerden in 1963. He showed that optical information could be stored holographically in either two dimensions (on a surface) or in three dimensions (in a volume), and that for idealized conditions at visible wavelengths, the storage capacity is 4×10^8 bits/cm^2 in two dimensions and 8×10^{12} bits/cm^3 in three dimensions. High-capacity storage in volume by holographic techniques has since been the subject of much study. While of fundamental importance, this is but one aspect of volume holography. The numerous features of volume holographic systems are listed below.

Also of great importance, is the basic scientific information that is resulting from this research. This information is having an increasing effect on integrated optics and optical communications through its impact on material parameter evaluation and performance characterization of optical devices for modulation, distributed feedback, reflecting, filtering, and coupling. This is discussed after the listing of volume holographic system features.

The potential characteristics of volume holographic systems are numerous and interrelated. Some of these are:

1. High Capacity Storage. Vast quantities of data ($\sim 10^{13}$ bits) may potentially be stored and randomly accessed using volume holography. This mass store may be:
   (a) archival. The data may be stored "permanently" and have a lifetime on the order of 10^3 years. Applications might include map storage, computer software storage, defense data storage, etc.
   (b) read-mostly. The information may require changing at a slow rate.

Applications might include inventory data storage, weather prediction data storage, etc.

(c) fast recording. The storing device may be a high data rate recorder. Storage may be temporary in this mode but input data rates are very high. This would be a very fast reusable mass store for use with interrupted optical communication channels, high data rate telemetry, etc.

(d) fast read-write-erase. The mass store may be basically a large and fast computer memory. Signals are continually written, rewritten, and read out.

2. Random Access. Using the laser holographic technique, all stored information is randomly accessible. Only the deflection of a laser beam to a new location and angle is required.

3. Two-Dimensional Format. Due to the nature of optical holography, the data is inherently stored in a two-dimensional format. This may be:

(a) an image (two-dimensional analog data) or

(b) a data page (two-dimensional digital data).

4. High Transfer Rate. The holographic reconstruction process reproduces an entire page with each read-out positioning of the laser beam. Thus the entire image or data page is accessed in a single operational cycle. For example, with 10^4 bits/page and a 10^{-6} second access time, the transfer rate is 10^{10} bits/second.

5. Multi-Port Configuration. Entirely new processing architectures are possible with holographic optical memories due to their multi-port capability. That is, the stored images or data pages may be accessed by multiple users simultaneously. Operationally multiple laser beams

would read out holograms simultaneously. This is possible since the beams do not interact with each other and are not in any way impeded by each others presence. There are several types of use for a multi-port store:

(a) record access system. Many users would have simultaneous access to large blocks of information in this scheme.

(b) simultaneously shared memory processing. A processor is attached to each port of the memory in this application.

(c) parallel processing. In this configuration, the processors are interconnected. Processed signals are transferred between individual processors. This allows true digital parallel processing with a single data store (unlike Illiac IV, for example, where each processor requires its own memory).

6. Ease of Recording Two-Dimensional Information. Due to the optical nature and the two-dimensional nature of storage and retrieval in holography, it is extremely straight forward to store two-dimensional signals for processing.

7. Analog and Digital Storage. The same volume holographic storage system may simultaneously contain stored images (analog information) and stored data pages (digital information).

8. Analog Processing. A volume holographic system is uniquely useful in analog processing of two-dimensional information. The image or data page to be processed and the two-dimensional filter may both be stored in the same storage medium. The filter could be a general complex two-dimensional filter for pattern recognition (correlation by vander Lugt filtering), feature extraction, image enhancement (such as deblurring), or other types of picture processing. The filter is ready for use in

its stored condition. The image or data page needs only to be read out and optically passed through the filter at the proper angular access orientation. This represents true optical parallel processing of two-dimensional analog signals.

9. Digital Processing. It has recently been shown that logic operations may be performed between pages of digital data stored in a volume holographic storage and retrieval system. By introduction of a phase shift in the reference beam and reintroducing one of the pages as the object beam, it is possible to perform an "exclusive or" operation between each corresponding bit on the two pages. Thus, if each page contains 10^4 bits, there are effectively 10^4 operations performed in one operational cycle. This represents true optical parallel processing of two-dimensional digital data. In addition, the Boolean "or" is straightforwardly obtainable. Using the basic "exclusive or" and "or" operations, all other Boolean operations may be implemented.

Research in volume holography is contributing much new scientific information of broad value. One such area of contribution is in the determination of physical processes and parameters in electro-optic crystals. Our own work (J. Appl. Phys., vol. 47, pp. 2757-2758, 1976) has shown how the electron mobility, lifetime, generation rate, drift length, diffusion length, and dielectric relaxation time may be determined from fundamental holography experiments. This provides information and powerful diagnostic tools for all areas of optical science and engineering (such as optical communications) that utilize electro-optic materials. The potential performance characteristics of given materials can thus be estimated in advance as well as obtaining information about altering the performance through modification of the physical parameters (for example, by doping or by applying a d.c. electric field).

Another major area strongly affected by the contribution of new information from this research is integrated optics and grating components. The generation and characterization of holographic gratings is central to this research. The analysis of the externally measurable diffraction effects due to grating shape (deviations from sinusoidality in the grating vector direction) and due to variations with grating thickness (nonuniformities in the direction perpendicular to the grating vector) represent studies that have an important impact on high efficiency holographic grating fabrication and the construction of distributed feedback lasers, Bragg reflectors, Bragg filters, and optical grating couplers. This research should ultimately lead to the development of synthesis and design techniques whereby a grating component may be constructed with a given set of characteristics for a specific application.

III. OPTICAL MEMORY SYSTEMS

Optical Memory Systems

That gap between the memory system needed and existing memories has only increased. Already the need for large-capacity rapid-access storage has raced ahead of existing technology. And the need is steadily growing.

There has been what seems to be an inherent tradeoff between memory capacity and access time. Rapidly developing optical memory technology, however, promises to avoid the tradeoff and fill the gap. Figure 1 graphically represents the state of existing memories, and the expected performance of optical memories.

Storage categories

The need for mass storage may be divided into several categories. Perhaps the least demanding of these categories is archival storage or record access. In this category large amounts of data need to be stored in a central memory and occasionally accessed. Examples include libraries, insurance data, medical data, seismic data, criminal data, tax information, patent records, telephone numbers, stock market information, computer softwear packages, defense data, postal data, credit data, large inventories, etc. Numerous governmental and private organizations currently have magnetic tape libraries containing over 200,000 reels of magnetic tape. Information stored in this manner is both expensive and very slowly accessible. This category of storage primarily requires a read-only memory, as changing the data occurs infrequently by computer standards.

A second category requires high data rate recording and temporary storage. An example would be high bit rate optical communications systems. In optical communications efficient use of turbulent channels will require very high capacity, very fast, reusable mass storage for recording during temporary interruptions of these channels. Another example is data recording during a space probe fly-by. Here a great amount of data is gathered during a brief period of time. If this information could be stored, it could later be transmitted at a low bit rate to minimize transmission errors in the data. Large scale weather prediction programs are still another example where large amounts of data need to be stored temporarily.

A third category for high capacity storage is in computer memories. Present day computing systems utilize a complex hierachy of storage devices. Some of the more important of these memories are magnetic tape, disks, drums, cores, and semiconductors. The access times and storage capacities of these devices are given in Figure 1. Modern computers use a combination of the large and slow along with small and fast memories in a hierarchical structure to realize efficient computing. The optical memory, due to its very high capacity and fast random access, offers the potential of replacing a large portion of the existing memory hierarchy. This is probably the most obvious application of high capacity, rapid access optical memories.

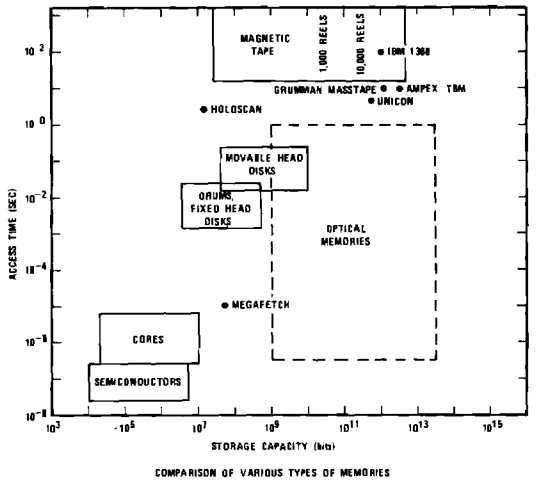

Figure 1. A graphic view of the present and future performance of various memory systems.

The development of new computer architectures is another area where optical memories will prove useful. This represents a new area based in part on the multi-port capability of optical memories [1] and will be discussed in more detail in a later section.

Today several high, capacity memories using nonoptical technology are available [19]. These include the Ampex Terabit System (TBM) and the Grumman Masstape System. These memory systems are shown in Figure 1 to have access times of about 10 seconds. The maximum storage capacities for these memories are 8.8×10^{11} bits for the Grumman Masstape and 2.9×10^{12} bits for the Ampex Terabit System. While this amount of storage is certainly adequate, the long access times make these systems unusable as rapid random access memories.

DESIGN DECISIONS

Design of an optical memory system has received much analysis (see e.g. refs. 5, 15, 17, 24, 30, 34, 35). Among the fundamental design decisions are:

1. Information should be stored in holographic form as opposed to direct image storage. In the typical configuration, the hologram will be the recording of the interference pattern between the Fourier transform of the bit pattern and a plane wave reference beam. Due to the distributed nature of the information, the storage of data in holographic form provides protection from localized loss of data due to material imperfections or dust.
2. Information should be stored in a page organized format as opposed to a three dimensional isometric view. The ability of holography to provide three dimensional views of objects is of no particular value in mass data storage. The reconstructed data will simply be in the form of two dimensional pages.
3. Information should be stored in a binary code as opposed to a pictorial representation. A page of binary data would appear as a series of bright and dark spots representing the 1's and 0's of the digital data. Pictoral representations, such as a printed page, a drawing, a map or a photograph, are also usable. However, for very high information densities, constraints on the page composer and the detector matrix favor the use of binary code.
4. Information should be stored in thick holograms as opposed to thin holograms. The theoretical storage density of two dimensional (thin) holograms is 4×10^8 bits/cm^2 (one bit per square area one wavelength on a side) whereas in three dimensional volume (thick) holograms the theoretical storage density is 8×10^{12} bits/cm^3 (one bit per cube volume wavelength on a side) [36]. Obviously for truly high capacity storage, thick holograms (such as optical crystals) need to be used instead of thin holograms (such as in photographic emulsions or metal films). Holographic memory systems have been described which utilize three-dimensional storage [10, 12]. These systems superpose many holograms at a single location inside the thick recording medium by using a different reference beam angle for each hologram. Because of their volume nature, these holograms exhibit very strong angular selectivity [13, 21]. That is, to read a hologram, the reference beam must illuminate the hologram, within a narrow angular corridor about the Bragg angle for that hologram. Illumination outside of this angular corridor produces a rapidly decreasing intensity of reconstructed data. In addition, the thicker the hologram is, the narrower the angular corridor for reconstruction becomes. The superposition of multiple holograms at a single volume location introduces the additional problem of writing new holograms in that volume without affecting those already there. When lithium niobate is used as the three dimensional storage material, this problem may be solved by the application of an external electric field [2, 28]. This greatly increases the sensitivity for writing while the sensitivity for erasure remains unchanged and at a much lower value. Thus as a new hologram is written, the other holograms at that location are only slightly erased. In addition, multiple hologram storage has been achieved in lithium niobate by applying a thermal bias [29]. This has allowed the selection of the erase/write asymmetry required for multiple hologram storage. With this technique, over five hundred holograms, each with more than 2.5% diffraction efficiency were recorded in 0.01% iron doped lithium niobate. The problem of selective erasure

TABLE 1
TYPES OF BEAM DEFLECTORS

GALVONOMETERS	ACOUSTO-OPTIC	ELECTRO-OPTIC
Moving iron galvonometer Moving coil galvonometer	Alpha-iodic acid (α - HIO_3) Lead molybdate ($PbMoO_4$) Tellurite glass Tl_3AsS_4 Water (H_2O) As_2S_3 glass TeO_2	Lithium niobate ($LiNbO_3$) Strontium barium niobate ($Sr_{0.75}Ba_{0.25}Nb_2O_6$) Nitrobenzene Potassium tantalum niobate (KTN)

of a single hologram among superposed holograms has been solved by writing a complementary hologram in which the refractive index changes cancel with those of the original hologram [20].
5. The optical memory system should contain no moving parts. This is necessary to achieve realistic operating speeds that are consistent with computer requirements. In addition, mechanical movements in a complex memory system may well reduce the reliability to an unacceptable level.

OPTICAL MEMORY COMPONENTS

To construct an optical memory five basic components are needed: an optical source, beam deflectors, a page composer, the recording material, and a detector matrix. These components are then interfaced with each other using conventional optics and electronics. The technologies associated with page composers, beam deflectors, and recording materials, overlap each other to a large extent. Specifically, it is conceivable that lithium niobate may be used in all three components.

Optical source

A laser is needed to produce the coherent, collimated light required in an optical memory system. The laser must be gated or pulsed to operate at about 10^6 pulses per second. Additionally, an average optical power of about one watt will be needed. These requirements as well as requirements on the reliability, amplitude stability, and frequency stability can all be met with existing lasers. Completely satisfactory, argon ion lasers are available. The drawbacks of this laser are its high cost (about $20,000) and its low efficiency of conversion of electrical power to optical power (about 0.1%).

Beam deflectors

An optical memory system must utilize a number of beam deflectors to accurately position the laser beams for the reading, writing, and erasing operations. This positioning process must be both quick and accurate.

As shown in Table 1, there are three basic types of deflectors: galvonometers, acousto-optic deflectors, and electro-optic deflectors. A number of examples in each of these categories are also listed. The performance of a deflector may be quantified by the resolution and the random access time. Resolution may be defined as the maximum deflection angle divided by the diffraction limited angle. This ratio gives the total number of resolvable spots or total number of resolvable angular positions. Random access time is the time required to deflect the laser beam to a new angular position.

An extensive comparison of light beam deflectors has been performed by Zook [38]. Mechanical galvonometer deflectors are too slow for fast access memory applications (which require an access time of approximately one microsecond). Acousto-optic and electro-optic deflectors, on the other hand, can be constructed to achieve the necessary access times. These devices, however, lack the resolution attainable in galvonometers and must frequently be cascaded to achieve the number of resolvable locations needed. For example, an electro-optic deflector has been built capable of resolving a two dimensional array of 1024 X 1024 spots using twenty stages of deflection with an access time of 0.8 microseconds. [23].

Page composer

The input device for the optical memory is a page composer (block data composer), which converts digital electrical signals directly into a two dimensional optical array of bits. The page composer will be located in the object beam of the two beam holographic configuration. Reconstruction of the recorded data will duplicate the array of 1's and 0's (bright and dark spots) generated by the page composer.

There are a number of characteristics that the page composer must possess. These requirements include: 1. High frame speed—it must be possible to rapidly change the data page in the page composer. The change time ideally must be in the microsecond range. 2. High resolution—The size of each bit in the page composer needs to be small. Sizes in the range of 10 to 100 microns would be suitable. 3. Large aperture—The total area of the page composer transverse to the laser beam needs to be large enough to accommodate the number of bits per page desired. For many applications the bit array size should be in the range of 64 X 64 elements to 1024 X 1024 elements. 4. High contrast ratio—The achievement of a high contrast ratio relaxes the subsequent requirements on the recording material and the detector matrix. A contrast ratio of 100 to 1 or greater is desirable and this has been achieved in a number of page composer type devices. 5. Stability—The characteristics of page composer materials must not be degraded by exposure to high intensity light (the object beam). 6. Uniformity—Material nonuniformities in the block data composer must be below the minimum level associated with the onset of readout errors in the memory system.

A wide variety of approaches exist for the construction of page composers. A number of these approaches are listed in Table 2. Obviously, a large number of physical effects and a large number of materials are potentially usable in page composers. Liquid crystal block data composers [27, 37] appear to be very useful. RCA has constructed a 1024 bit liquid crystal page composer [30]. A major problem with liquid crystal page composers has been their relatively slow frame speed (on the order of 100 ms). Lead lanthanum zirconate titanate (PLZT) block data composers [25] also appear to be very promising. These page composers, which do not suffer from a slow frame rate, have four basic modes of operation: strain biased mode, scattering mode, edge effect mode, and differential phase mode [11]. This last mode of operation eliminates the detrimental effects of background nonuniformities in the PLZT, but requires a double hologram exposure through the data mask. Two recently developed approaches to block data composers utilize a thin, deformable, membrane mirror array [8] and the thermally induced shift in the optical absorption band edge in CdS [18].

Recording material

The central element of the optical memory is the recording material. This piece of material, often rather small in size, provides the entire storage capacity of the optical memory system. Recording materials must possess a number of important characteristics to achieve the high storage capacities that have been predicted for optical memories. These requirements on the optical recording material include: 1. High sensitivity—It is desirable that only a small amount of optical energy per unit area be needed to record the hologram of a data page. Table 3 lists the necessary writing energy densities for a number of recording materials. For a practical system an energy density of about 1 milljoule/cm² or less will be needed. 2. Large diffraction efficiency—Diffraction efficiency is the fraction of the read-

TABLE 2
TYPES OF PAGE COMPOSERS*

PAGE COMPOSER CONCEPT	MATERIALS	ADDRESSING TECHNIQUES
Polarization rotation by induced birefringence (electrooptic effects)	PLZT (ceramic), $Bi_4Ti_3O_{12}$ KDP, KD*P, ADP	Electrode matrix, Electron beam, Light beam (with photoconductor)
Phase changes by formation of surface relief pattern	Thermoplastics, Photoplastics, Thin metalized membranes	Electron beam, Electrode matrix plus charge
Phase disturbances by piezoelectric excitation of reflecting surfaces	Mirrored piezoelectric crystals	Individual switches to an rf driver
Optical density change by induced absorption	Photochromics, Cathodochromics	Light beam (uv) plus flood illumination for erase, Electron beam plus flood illumination for erase
Optical scattering change by electrical agitation	Liquid crystals	Electrode matrix, Light beam (with photoconductor)
Polarization rotation by magnetooptic effects	MnBi, EuO:Fe, Ni-Fe $FeBO_3$, FeF_3	Light beam (absorption), Conductor matrix
Traveling phase changes by acoustooptic interaction (Debye-Sears and Bragg effects)	Water (and other liquids), Fused quartz (and other amorphous solids), $PbMoO_4$ (and other crystals)	Transverse interaction of coherent light and traveling acoustic waves
Thermally induced shift in absorption band edge	CdS, CdSe, As_2S_3	Electrode matrix for heating and heat sink substrate for cooling
Optical scattering by poled and unpoled regions of a ferroelectric	PLZT (ceramic)	Electrode matrix
Phase changes by variation of optical path length	Electrostrictive materials, PLZT (ceramic)	Electrode matrix, Double hologram recording method
Reflection changes from thin, deformable membrane mirror elements	Metal films over a substrate support structure	Electrode feedthrough from transistor on back of substrate

* extended version of table from H. N. Roberts, Applied Optics, vol. 11, pp. 397-404, February 1972.

ing light (reference beam) that is diffracted into the reconstructed data beam. It must be possible to record a single hologram with a large diffraction efficiency, so that in practice many holograms may be recorded at a single location, each with an equal share of the total maximum diffraction efficiency. Therefore it is desirable to have the maximum diffraction efficiency as close to 100% as possible. 3. Erasable and rewritable—For a rapid cycle read-write-erase memory system, it must be possible to continuously alter the stored data in the memory without encountering any degradation in the material characteristics. 4. Long lifetime of stored information—Stored data should persist for long periods of time before having to be refreshed. Ideally, storage should be permanent. 5. Nonvolatile storage—Data should remain recorded in the memory in the absence of system power. 6. Nondestructive readout—It should be possible to perform an essentially unlimited number of read operations without degrading or altering the stored data. 7. Three dimensional storage—To achieve very high capacity storage, the information should be stored in thick (volume) holograms. Together with the requirement of high diffraction efficiency, this means that the hologram should be a thick phase (nonabsorbing) hologram. 8. High resolution—The storage material obviously must be capable of recording the very fine (wavelength size) variations of the interference pattern produced by the intersection of

the object and reference beams.

Research and development on optical recording materials for optical memories has produced remarkable advances in the past few years. Many different types of materials, as indicated in Table 2, are contenders for recording applications. Considering all of the above material requirements, the photorefractive materials (optically induced changes in index of refraction) appear to be especially promising. These materials, often ferroelectric crystals such as lithium niobate and strontium barium niobate (SBN), have been considerably developed and improved. For example, in the first use of lithium niobate as a recording material in 1968 a writing energy density of a approximately 100 joules/cm² was required [7]. Less than six years later, doped versions of lithium niobate were shown to exhibit writing energy densities of 2 millijoules/cm² [26]. This is an improvement in sensitivity of almost 5 orders of magnitude. Similar sensitivity improvements have been reported for SBN [33]. The other needed material characteristics have all been reported in the photorefractive ferroelectrics—large diffraction efficiency [3, 7], optical erasing and rewriting [2, 14, 28], long lifetime of stored data [4], three dimensional storage [7, 13], etc. At the present time these very favorable material characteristics have not been simultaneously observed in a single sample. Further, it is still not clear that all of the desired characteristics can coexist in a single doped ferroelectric material. Tradeoffs that have not been discovered may exist between the various desired properties. Clearly, more basic research on optical recording materials is required to resolve the many remaining questions. If a single material can reliably and reproducibly be made with all of the above required properties, read-write-erase optical memories will become commercially available.

Detector matrix

An array of photodetectors is needed to convert the holographically reconstructed data into an electrical signal. This photosensitive readout array would have one photodiode or phototransistor for each bit of data in the reconstructed page. Each sensor in the array would function as a theshold detector indicating the presence or absence of light (a binary 1 or 0). All stored holograms would be read out with the same detector matrix (for a single port memory).

The photodetectors ideally must exhibit a low threshold detection power. Noise associated with the operation of the photodetector determines the lower limit of optical power needed for threshold detection. For a signal-to-noise ratio of about 10, an optical power in the range of 0.1 to 1.0 microwatts per bit will be required. Already readout arrays operating at 0.3 microwatts per bit have been constructed [6].

The second basic requirement on the detector matrix is that a large defect free array be constructable with existing technology. Modern semiconductor technology has fulfilled this requirement. Bell Laboratories has constructed a silicon-diode-array camera tube that consists of 525,000 individual photodiodes on a single silicon slice [9]. An LSI phototransistor array with 51,200 silicon phototransistors has been built [22] using multilayer interconnection techniques so that any bit can be read out in about a microsecond. Continuing advances in semiconductor technology assure the availability of high quality photodetector arrays.

A number of optical memories that have become commercially available are listed in Table 4.

Optical mass memories currently in existence include the IBM 1360 memory, introduced in 1966 but no longer in production. This Photo Digital Mass Storage System uses electron beams for recording and is read out optically. As shown in Figure 1 its trillion bits are only very slowly accessible. Precision Instrument's Unicon laser mass memory system [16] is an optical mass memory that is now commercially available. It uses an argon laser to perform bit-by-bit recording by vaporizing small holes in a metallized polyester belt. This read-only nonholographic memory has a storage capacity of 7×10^{11} bits and an average access time of somewhat less than 10 seconds.

The Holoscan read-only-memory [32] is a very efficient holographic memory used in credit card verification. Its limited capacity (1.2×10^7 bits) and limited access time (2 seconds) are quite adequate for its intended use. The 3M Company has developed the first nonmechanical, laser, holographic memory [31] to become commercially available. It is also a read-only memory. It has a capacity of 5×10^7 bits and operates at computer compatible speeds, having a random access time of 10 microseconds. This system uses a unique two dimensional scannable electron beam pumped semiconductor laser for accessing the 1024 x 1024 microhologram array.

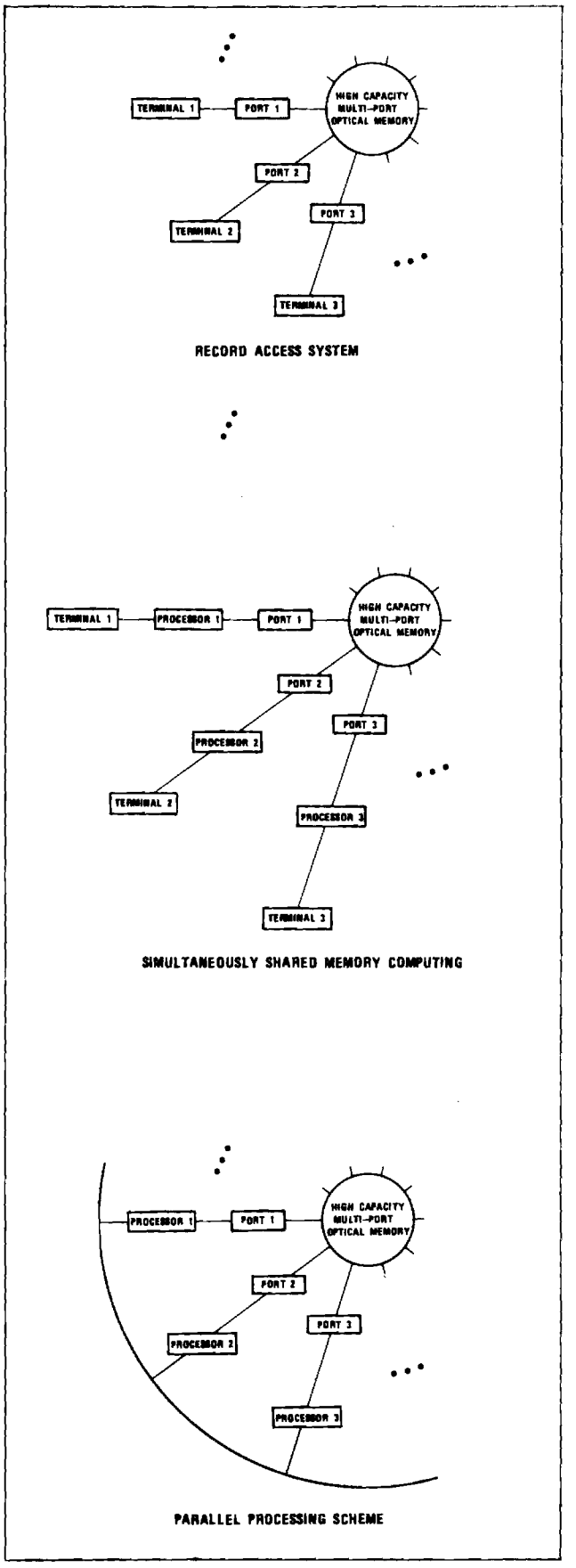

Figure 2. Possible schemes for new computer architectures using an optical memory with a multi-port access capability.

TABLE 3
REQUIRED WRITING ENERGY DENSITY FOR VARIOUS OPTICAL RECORDING MATERIALS.

MATERIAL	TYPE OF MATERIAL	WRITING ENERGY DENSITY (joules/cm²)
$Bi_{12}SiO_{20}$	Ferroelectric-Photoconductive	1×10^{-5}
Malachite Green:		
Sucrose Benzoate	Thermaplastic	2×10^{-5}
Agfa 8E70	Photographic	2×10^{-6}
Kodak 649F	Photographic	7×10^{-6}
$Bi_4Ti_3O_{12}$-ZnSe	Ferroelectric-Photoconductive	1×10^{-3}
$LiNbO_3$:Fe	Photorefractive	2×10^{-3}
$Sr_{0.75}Ba_{0.25}Nb_2O_6$	Photarefractive	6×10^{-3}
Dichromated Geletin	Photachemical	1×10^{-2}
CaF_2:Ce	Photochromic	1×10^{-2}
PLZT	Ferroelectric-Photoconductive	1×10^{-2}
KCL:Na	Photochromic	1×10^{-2}
MnBi	Magnetooptic	3×10^{-2}
$Te_{88}Ge_7As_5$	Amorphous Semiconductor	5×10^{-2}
GdIG	Magnetooptic	9×10^{-2}
EuO	Magnetooptic	9×10^{-2}
NaF	Photochromic	9×10^{-2}
CoPniFe	Magnetooptic	1×10^{-1}
$SrTiO_3$:Ni:Mo	Photochromic	2×10^{-1}
$BaTiO_3$	Photorefractive	2×10^{-1}
MnAlGe	Magnetooptic	3×10^{-1}
$Te_{81}Ge_{15}Sb_2S_2$	Amorphous Semiconductor	5×10^{-1}
PMMA (Q-doped)	Photopolymer	1
KBr	Photochromic	1
Cu_2HgI_4	Thermoplastic	3
$BaNaNb_5O_{15}$	Photorefractive	5
$As_{16}S_{86}$	Amorphous Semiconductor	5
$Bi_4Ti_3O_{12}$	Photorefractive	10
$LiNbO_3$ (undoped)	Photorefractive	100
PMMA (undoped)	Photopolymer	100

New computer architectures

Optical memories, in addition to increasing the capabilities of existing computers, promise to spur the development of new computer architectures [1]. It is conceptually simple to construct an optical memory in which any of the data pages may be accessed by multiple users simultaneously. This feature, not available in conventional memories, allows access to the memory through any of its multiple ports.

Speed, capacity, and cost relationships have determined a basic computer architecture that utilizes a hierarchical memory structure. A common way of implementing this structure has been to provide for page swaps between a local memory and the mass store, and for word (or character) swaps between the local store and the central processing unit. Such a structure has inevitably led to problems of address, replacing pages, multiple contention for pages and memory allocation. The contention problem can be relieved by building a mass memory with multiple access ports. If such a memory has simultaneous read/write capability, then each user demanding use of mass memory appears to have complete control. Problems of write protection, memory allocation and paging still remain, but the speed of the mass memory has been effectively increased by having multi-port capability.

Speed can be further enhanced by utilizing a mass memory which accesses a single page in one access cycle. This differs from mass memory devices such as disks where the page is accessed sequentially making the access time proportional to page size. A parallel transfer of a single page between the mass memory and an individual memory port coupled with the idea of multi-port simultaneous page access can provide a distinctly new storage device for parallel computation. Current methods in parallel computation utilize multiple processors and multiple memories and require many memory to memory swaps to perform array type computations. A mass memory with multi-port access capability would reduce the word exchanges and could enhance parallel computation.

Three typical applications for a multi-port memory as shown in Figure 2 are: 1. Record access — As previously discussed, many applications exist that require the storage and retrieval of large blocks of information. This can be realized very efficiently with a multi-port memory. In these systems, data would be stored in page format in the multi-port memory. Access to any page would be via a terminal through one of the memory access ports. The data requirement of each terminal is, in some applications, low enough to have one memory port support several terminals through a multiplexer. Normally these terminals are used in a read access mode and would not be allowed to perform write operations to the memory. 2. Simultaneously shared memory computing — In this application the user performs transformations on the data accessed. This adds arithmetic logic units to the architecture as shown. 3. Parallel processing — There are many scientific problems requiring enormous numbers of computations. One approach to this problem has been a multi-processor parallel computation technique. Essentially all processors are dedicated to solving one step and then, after a transfer to the appropriate processor, repeating the step-wise computation. Problems arise from synchronization and system reliability when the parallelism is carried as far as that in Illiac IV. A possible structure for parallel processing is also shown in Figure 2. Each processor is connected to the multi-port memory through a port. Transfers between processors can be made on an outer bus connecting each processor.

Summary

There has been a great deal of activity in recent years related to optical memories. Research and development have produced advances in optical memory components and the materials used in these components. In the area of recording materials, more basic research clearly is required. The other components for the optical memory are either, available or can be with additional engineering effort.

In the realm of system configurations for optical memories, there has been a sizeable effort to develop prototype memory systems. Holographic optical memories have been built by RCA Labs, Harris-Intertype, Bell Labs, Thomson-CSF, Nippon Corp., Optical Data Systems, 3M Company, and others. For the most part these are limited versions of the full scale high capacity read-write-erase memory system of the future. In addition, new computer architectures are being identified to take advantage of and efficiently use the unique capabilities that are possible in optical memories. □

References

1. Alford, C. O. and T. K. Gaylord (April 1975). The Potential of Multiport Optical Memories in Digital Computing. DIGEST 1975 INTERNL OPTICAL COMPUTING CONF. 121-123.

2. Amodei, J.J. and D.L. Staebler. (March, 1972). Holographic recording in lithium niobate. RCA REVIEW. 33:71-93.

3. Amodei, J.J., W. Phillips and D.L. Staebler (Feb., 1972). Improved electro optic materials and fixing techniques for holographic recording. APPL. OPT. 11: 390-396.

TABLE 4

COMMERCIAL OPTICAL MEMORIES

COMPANY	SYSTEM	LASER	HOLOGRAPHIC	NON-MECHANICAL	DATE
IBM	1360 Photodigital Mass Storage System	no	no	no	1966
Precision Instruments	690-212 Unicon Laser Mass Memory	yes	no	no	1971
Optical Data Systems	Holoscan	yes	yes	no	1972
3M Company	Megafetch Data Processor	yes	yes	yes	1974

4. Amodei, J.J. and D.L. Staebler (June 15, 1971). Holographic pattern fixing in electro-optic crystals. APPL. PHYS. LETTERS. 18: 540-542.

5. Anderson, L.K. (Sept., 1971). Application of holographic optical techniques to bulk memory. IEEE TRANS. MAGNETICS. MAG.-7: 601-605.

6. Assour, J.M. and R.D. Lohman (Dec., 1969). A photodetector array for holographic optical memories. RCA REVIEW. 30: 557-566.

7. Chen, F.S., J.T. LaMacchia and D.B. Fraser (Oct. 1, 1968). Holographic storage in lithium niobate. APPL. PHYS. LETTERS. 13: 223-225.

8. Consentino, L.S. and W.C. Stewart (March, 1973). A membrane page composer. RCA REVIEW. 34: 45-79.

9. Crowell, M.H. and E.F. Labuda (May-June, 1969). The silicon diode array camera tube. BELL SYS. TECH. J. 48: 1481-1528.

10. d'Auria, L., J.P. Huignard, C. Slezak and E. Spitz (April, 1974). Experimental holographic read-write memory using 3-D storage. APPL. OPT. 13: 808-818.

11. Drake, M.D. (March, 1973). PLZT matrix-type block data composers. APPL. OPT. 13: 45-79.

12. Gaylord, T.K. (Nov., 1972). The high capacity storage problem: is optical holography the answer? OPTICAL SPECTRA. 6: 25-37.

13. Gaylord, T.K. and F.K. Tittel (Oct., 1973). Angular selectivity of lithium niobate volume holograms. J. APPL. PHYS. 44:4771-4773.

14. Gaylord, T.K., T.A. Rabson and F.K. Tittel (Jan. 1, 1972). Optically erasable and rewritable solid-state holograms. APPL. PHYS. LETTERS. 20: 47-49.

15. Graf, P. and M. Lang (June, 1972). Geometrical aspects of consistent holographic memory design. APPL. OPT. 11: 1382-1388.

16. Gray, E. E. (March 1973) Permanent Storage Using Direct Laser Recording. DIGEST TOPICAL MEETING OPTICAL STORAGE OF DIGITAL DATA. MA41-MA44.

17. Hill, B. (Jan., 1972). Some aspects of a large capacity holographic memory. APPL. OPT. 11: 182-191.

18. Hill, B. and K.P. Schmidt (June, 1973). New page composer for holographic data storage. APPL. OPT. 12: 1193-1198.

19. Houston, G.B. (Oct., 1973). Trillion bit memories. DATAMATION. 19: 52-58.

20. Huignard, J.P., J.P. Herriau, and F. Micheron (1 March 1975). Coherent Selective Erasure of Superimposed Volume Holograms in $LiNbO_3$. APPL. PHYS. LETTERS. 26:256-258.

21. Kogelnik, H. (Nov., 1969). Coupled wave theory for thick hologram grating. BELL SYS. TECH. J. 48: 2909-2947.

22. Mend, W.G., E.E. McCoy and R.A. Anders (Oct., 1970). Microminiature solid-state imaging system utilizing hybrid LSI techniques. IEEE J. SOLID-STATE CIRCUITS. SC-5: 254-260.

23. Meyer, H., D. Riekmann, K.P. Schmidt, M. Rahlff, E. Schröeder and W. Thust (Aug., 1972). Design and performance of a 20-stage digital light beam deflector. APPL. OPT. 11: 1732-1736.

24. Rajchman, J.A. (March 1, 1970). Promise of optical memories. J. APPL. PHYS. 41: 1376-1383.

25. Roberts, H.N. (Feb., 1972). Strain-biased PLZT input devices (page composers) for holographic memories and optical data processing. APPL. OPT. 11: 397-404.

26. Shah, P., T.A. Rabson, F.K. Tittel and T.K. Gaylord (Feb., 1974). Volume holographic recording and storage in Fe-doped $LiNbO_3$, using optical pulses. APPL. PHYS. LETTERS. 24: 130-131.

27. Special Issue of Display Devices (Nov., 1973). IEEE TRANS. ON ELEC. DEVICES. ED-20.

28. Staebler, D.L. and W. Phillips (April, 1974). Fe-doped $LiNbO_3$ for read-write applications. APPL. OPT. 13: 788-794.

29. Staebler, D. L., W. J. Burke, W. Phillips, and J.J. Amodei (15 February 1975). Multiple Storage and Erasure of Fixed Holograms in Fe-Doped $LiNbO_3$. APPL. PHYS. LETTERS. 26:182-184.

30. Stewart, W.C., R.S. Mezrich, L.S. Cosentino, E.M. Nagle, F.S. Wendt and R.D. Lohman (March, 1973). An experimental read-write holographic memory. RCA REVIEW. 34: 3-44.

31. Strehlow, W. H., R. L. Dennison and J. R. Packard (April 1974). Holographic Data Store. J. OPT. SOC. AM. 64:543-544.

32. Sutherlin, K. K., J. P Lauer, and R. W. Olenick (June 1974). Holoscan: A Commercial Holographic ROM. APPL. OPT. 13:1345-1354.

33. Thaxter, J.B. and M. Kestigian (April, 1974). Unique properties of SBN and their use in a layered optical memory. APPL. OPT. 13: 913-924.

34. Vander Lugt, A. (July, 1973). Design relationships for holographic memories. APPL. OPT. 12: 1675-1685.

35. VanderLugt, A. (May 1975). Packing Density in Holographic Systems. APPL. OPT. 14:1081-1087.

36. van Heerden, P.J. (April, 1963). Theory of optical information storage in solids. APPL. OPT. 2: 393-400.

37. White, D.L. and M. Feldman (Dec., 1970). Liquid crystal light waves. ELECTRONICS LETTERS. 6: 837-840.

38. Zook, J.D. (April, 1974). Light beam deflector performance: a comparative analysis. APPL. OPT. 13: 875-887.

Acknowledgments

We would like to thank Dr. Thomas K. Gaylord, Assistant Professor of Electrical Engineering at the Georgia Institute of Technology and a member of the Editorial Advisory Board of the Optical Publishing Co., for providing us with this article.

IV. OPTICALLY-INDUCED PHYSICAL PROCESSES IN ELECTROOPTIC CRYSTALS

Tensor description of physical properties of crystals

T. K. Gaylord
School of Electrical Engineering
Georgia Institute of Technology
Atlanta, Georgia 30332
(Received 10 January 1975; revised 26 February 1975)

The use of tensors for describing the physical properties of crystals is not particularly widespread in undergraduate curricula. Tensor concepts, however, are unavoidable in describing the properties of anisotropic media, of which crystals are a very important example. This paper describes suggested introductory material on tensors for use in an undergraduate materials science course. Special emphasis has been placed on communicating the basic tensor concepts through the use of examples. Mathematical manipulations have intentionally been minimized.

I. INTRODUCTION AND HISTORICAL BACKGROUND

Crystals play a particularly important role in modern applied physics. They are used in the fabrication of transistors, integrated circuits, electro-optic modulators, various transducers, etc. The mechanical, electrical, and optical properties of these crystals are generally anisotropic. That is, the properties vary with direction in the material. This anisotropic behavior of crystals has been known since the beginnings of solid-state science. In fact, this behavior led to the categorization of all crystalline materials into a limited number of distinct groups.

The description of the physical properties of crystals may be concisely given in terms of tensors. It has been said, "Tensor calculus has always been the best instrument for dealing with the properties of anisotropic media."[1] The beginnings of tensor analysis can be traced to the work of Gauss in the field of differential geometry (circa 1868). Since that time tensors have been successfully applied to a number of areas of physics and engineering. These include analytical mechanics,[2] relativistic mechanics,[3] mechanics of continuous media,[4] and rotating electrical machinery.[5] These areas developed somewhat independently of each other. Simultaneously, tensor concepts were applied to describing the physical properties of crystals. The first major compilation of this information was prepared by Voigt[6] in 1910. Excellent modern summaries and reviews of the tensor description of crystal properties have since been written by Nye[7] and Smith.[8]

II. MOTIVATION FOR INTRODUCING TENSOR CONCEPTS

As our understanding of physical principles and concepts improves, so also should our ability to communicate these ideas correctly and concisely. Furthermore, the presentation of physical ideas should be consistent with the level of mathematical sophistication of the learner.

In these respects it would appear that the use of tensor concepts has been largely overlooked even though modern students are well equipped in the necessary background mathematics. Tensor ideas have been largely confined to advanced courses[9,10] and are usually not mentioned in undergraduate textbooks on materials science. However, the use of tensor concepts is essentially unavoidable in the study of solid-state science. Tensors are needed to describe general relationships between physical quantities which may themselves be scalars, vectors, second-rank tensors, etc. Many "modern" phenomena, such as the electro-optic effect, require the use of tensors for their description.

III. PHILOSOPHY AND SCOPE

A. Method of introducing tensor concepts

How should the tensor description of physical properties be introduced to students? A good philosophy was that espoused by Newton: "exempla non minus doceunt quam precaepta." Examples are not only more palatable to students, they are the crux of the information which is to be taught. The aesthetic beauty of tensors and tensor manipulations is a secondary interest to many students. The specific approach used here concentrates on the basic uses of tensors and tensor concepts in describing physical phenomena. The amount of mathematical manipulation is intentionally kept to a minimum.

B. Scope

For classroom applications, the scope of tensor concepts and uses needs to be limited to a number of the most important areas. It is suggested that these basic areas include the following:

(i) *Linear relationships*—simple linear relationships between physical quantities.

(ii) *Nonlinear relationships*—the description of higher order nonlinear physical phenomena.

(iii) *Effects of crystal symmetry on tensors*—the simplification and reduction of tensors as determined by crystal structure.

(iv) *Estimating magnitudes of physical effects*—the use of tensor rank to estimate the relative magnitudes of physical effects.

(v) *Relationships between physical effects*—the use of tensors to interrelate physical effects which occur simultaneously in a solid.

IV. BASIC TENSOR CONCEPTS

Tensors may be used to represent a wide variety of physical properties. A particular tensor is ultimately represented by a set of components. The number of components is equal to N^n, where N is the dimensionality of the

space of the tensor and n is the rank of the tensor. The dimensionality of the space in which crystals are represented is, of course, three (e.g., x,y,z). This is the dimensionality that will be used here in the description of the physical properties of solids. Higher dimensionalities also exist. For example, in relativistic mechanics time must be included and thus the space dimensionality is four (e.g., x,y,z,t).

In three-dimensional space, a tensor of rank n thus has 3^n components. Therefore, a zero-rank tensor has one component, a first-rank tensor has three components, a second-rank tensor, nine components, and so forth. A tensor of zero rank is a simple scalar and is written without a subscript. A first-rank tensor, α_i, is a vector and is written with a single subscript indicating its components. A second-rank tensor, α_{ij}, is written with two subscripts to represent its nine components ($i,j = 1,2,3$). Thus, in general, the number of subscripts on a tensor is equal to the rank of the tensor.

The gradient operation applied to a tensor increases its rank by one. For example, the gradient of voltage, a zero-rank tensor (scalar), is electric field, a first-rank tensor (vector). Likewise, force, a first-rank tensor (vector) becomes stress, a second-rank tensor, and so forth.

An important characteristic feature of tensors is that their components are dependent on the set of mutually orthogonal axes to which they are referenced. Thus, the components of a tensor are not unique but depend on the selection of the reference coordinate axes. This property of invariance and the definition of a tensor quantity may both be shown by considering the following.

Two orthogonal coordinate systems (x,y,z and x',y',z') having an arbitrary orientation with respect to each other are shown in Fig. 1. The direction cosines of x' with respect to x,y,z are given by $a_{x'x}$, $a_{x'y}$, $a_{x'z}$, respectively. Likewise, the direction cosines of y' and z' with respect to x,y,z, are given by $a_{y'x}$, $a_{y'y}$, $a_{y'z}$ and $a_{z'x}$, $a_{z'y}$, $a_{z'z}$, respectively. The components of the vector **A** with respect to the x',y',z' coordinate system are

$$\begin{aligned} A_{x'} &= a_{x'x}A_x + a_{x'y}A_y + a_{x'z}A_z, \\ A_{y'} &= a_{y'x}A_x + a_{y'y}A_y + a_{y'z}A_z, \\ A_{z'} &= a_{z'x}A_x + a_{z'y}A_y + a_{z'z}A_z \end{aligned} \tag{1}$$

or, written in matrix form,

$$\begin{bmatrix} A_{x'} \\ A_{y'} \\ A_{z'} \end{bmatrix} = \begin{bmatrix} a_{x'x} & a_{x'y} & a_{x'z} \\ a_{y'x} & a_{y'y} & a_{y'z} \\ a_{z'x} & a_{z'y} & a_{z'z} \end{bmatrix} \begin{bmatrix} A_x \\ A_y \\ A_z \end{bmatrix}. \tag{2}$$

By letting the subscript $i = 1,2,3$ for x',y',z', respectively, and the subscript $j = 1,2,3$ for x,y,z, respectively, the primed (new) components of the vector **A** in terms of the unprimed (old) components of the vector **A** may be expressed concisely as

$$A'_i = \sum_j a_{ij}A_j. \tag{3}$$

This is the transformation law for vectors. A vector is defined as a quantity whose components transform according to this equation. The vector **A**, whether it is represented by the components A'_i ($i = 1,2,3$) in the primed coordinate system or by the components A_j ($j = 1,2,3$) in the unprimed system, is of course the same vector. These representations are completely equivalent. Regardless of the set of axes the vector is referenced to, it is the same vector and represents the same physical quantity. The axes of the coordinate systems may be chosen arbitrarily

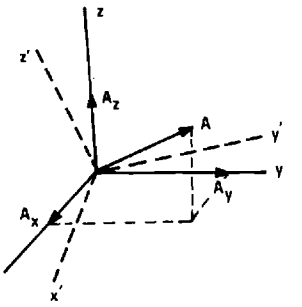

Fig. 1. Two possible sets of orthogonal coordinate axes.

Table I. The use of tensors to interrelate physical quantities.

Rank of tensor	Tensor notation	Quantities related	Mathematical expression
zero (scalar)	α	scalar to scalar	$A = \alpha B$
first (vector)	α_i	vector to scalar	$A_i = \alpha_i B$
second	α_{ij}	second-rank tensor to scalar	$A_{ij} = \alpha_{ij}B$
		vector to vector	$A_i = \sum \alpha_{ij}B_j$
third	α_{ijk}	third-rank tensor to scalar	$A_{ijk} = \alpha_{ijk}B$
		second-rank tensor to vector	$A_{ij} = \sum \alpha_{ijk}B_k$
		vector to second-rank tensor	$A_i = \sum \alpha_{ijk}B_{jk}$
		vector to two other vectors	$A_i = \sum \alpha_{ijk}B_jC_k$
fourth	α_{ijkl}	fourth-rank tensor to scalar	$A_{ijkl} = \alpha_{ijkl}B$
		third-rank tensor to vector	$A_{ijk} = \sum \alpha_{ijkl}B_l$
		second-rank tensor to second-rank tensor	$A_{ij} = \sum \alpha_{ijkl}B_{kl}$
		second-rank tensor to two vectors	$A_{ij} = \sum \alpha_{ijkl}B_kC_l$
		vector to third-rank tensor	$A_i = \sum \alpha_{ijkl}B_{jkl}$
		vector to second-rank tensor and vector	$A_i = \sum \alpha_{ijkl}B_{jk}C_l$
		vector to three vectors	$A_i = \sum \alpha_{ijkl}B_jC_kD_l$

Table II. Some common physical effects described by tensors.

Rank of tensor	Quantities related: Type of quantities	Specific quantities	Physical property
zero	scalar	internal energy	heat capacity
	scalar	temperature	
first	vector	polarization	pyroelectric
	scalar	temperature	effect
second	vector	current density	conductivity
	vector	electric field	
	vector	polarization	dielectric
	vector	electric field	susceptibility
	vector	magnetization	magnetic
	vector	magnetic field	permeability
	vector	electric field	Seebeck effect
	vector	temperature gradient	
	vector	electron group velocity	electron
	vector	electron wave vector	effective mass
	second-rank tensor	strain	thermal
	scalar	temperature	expansion
third	vector	polarization	piezoelectric
	second-rank tensor	stress	effect
	vector	electric field	inverse piezo-
	second-rank tensor	strain	electric effect
	second-rank tensor	refractive index	Pockels effect
	vector	electric field	(linear electro-optic effect)
	vector	current density	
	vector	electric field	Hall effect
	vector	magnetic field	
	vector	electric field	
	vector	temperature gradient	Nernst effect
	vector	magnetic field	
	vector	temperature gradient	Ettingshausen
	vector	current density	effect
	vector	magnetic field	
	second-rank tensor	strain	magneto-
	vector	magnetic field	striction
	vector	magnetization	inverse magne-
	second-rank tensor	stress	tostrictive effect
	vector	temperature gradient	Righi–Leduc
	vector	temperature gradient	effect
	vector	magnetic field	
	vector	polarization	optical second-
	vector	electric field	harmonic
	vector	electric field	generation
	vector	polarization	
	vector	electric field (at pump frequency)	optical parametric
	vector	electric field (at idler frequency)	oscillation

Table II (*cont'd*).

Rank of tensor	Quantities related: Type of quantities	Specific quantities	Physical property
fourth	second-rank tensor	stress	elasticity
	second-rank tensor	strain	
	second-rank tensor	strain	
	vector	electric field	electrostriction
	vector	electric field	
	second-rank tensor	refractive index	Kerr effect
	vector	electric field	(quadratic
	vector	electric field	electro-optic effect)
	vector	current density	
	vector	electric field	magneto-
	vector	magnetic field	resistivity
	vector	magnetic field	
	vector	polarization	optical third-
	vector	electric field	harmonic
	vector	electric field	generation
	vector	electric field	

except that the axes must be mutually orthogonal.

Likewise, a second-rank tensor represents a physical quantity and may be represented by components referenced to a particular orthogonal coordinate system. The components will change as the reference axes are changed. Again, however, the physical quantity which the tensor represents does not change. Only the method of representing the tensor has changed. For second-rank tensors the transformation law for changing reference axes is

$$T'_{ij} = \sum_{k,l} a_{ik} a_{jl} T_{kl}, \tag{4}$$

where i,j represent x',y',z' and k,l represent x,y,z. A second-rank tensor is defined as a quantity whose components transform according to this equation. This type of expression is also used for higher rank tensors. For a tensor of rank n, there will be n direction cosine factors in its transformation law.

Even though the practice will not be followed here, the Einstein summation convention is frequently used. This convention may be stated as follows: when a letter subscript occurs twice in the same term, summation with respect to that subscript is automatically understood. Using the Einstein summation convention, Eq. (4) would be written as $T'_{ij} = a_{ik} a_{jl} T_{kl}$.

V. THE RANGE OF PHYSICAL RELATIONSHIPS DESCRIBED BY TENSORS

Many of the physical properties of crystals are described by tensors. Tensors are used not only to describe relationships between vectors, as is their frequent use, but also to describe relationships between other tensor quantities. A listing of tensors up to rank four and the types of quantities that they can relate is given in Table I.

Inspection of Table I reveals the straightforward procedure by which tensors of rank higher than four can be used to interrelate physical quantities. In every case the sum of the ranks of the tensors of the physical quantities being related is equal to the rank of the tensor of the physical property which interrelates them.

A selected number of examples of electrical, mechanical, optical, and thermal effects which are described by tensors are listed in Table II.

VI. ILLUSTRATIVE EXAMPLE: CONDUCTIVITY

Only for the special case of isotropic materials can the use of tensors be avoided. Even though for a very large number of cases a physical property may not vary with direction in the crystal, this in general will not be the case. That is, a physical property such as the electrical conductivity will be different for an applied electric field along the $\langle 100 \rangle$ direction than for an applied field along the $\langle 111 \rangle$ direction. In addition, the resultant vector current density, **J**, due to the electric field, **E**, may not be in the same direction as the applied field! This makes the description of electrical conductivity even more difficult. An example of this general situation is illustrated in Fig. 2 (for the case of *n*-type germanium at high electric fields). Thus, in general, the following observations are made.

(a) The current density is not proportional to the electric field.

(b) The current density is not in the same direction as the electric field.

(c) The magnitude of the current density varies with crystallographic direction.

To describe mathematically this type of relationship between vectors (**J** and **E** in this case) requires the use of a series of tensor terms. For example, the general expression for the current density in a crystal may be expressed as a tensor expansion in powers of the electric field. The ith orthogonal component of current density is thus given by

$$J_i = \sum_j \sigma_{ij} E_j + \sum_{j,k} \sigma_{ijk} E_j E_k + \sum_{j,k,l} \sigma_{ijkl} E_j E_k E_l + \cdots, \tag{5}$$

where the subscript indices $j,k,l, \ldots,$ are each independently summed over the three orthogonal reference directions. σ_{ij} is a second-rank tensor with $3^2 = 9$ elements and can be represented by a 3×3 matrix. σ_{ijk} is a third-rank tensor with $3^3 = 27$ elements and can be represented by a $3 \times 3 \times 3$ matrix. σ_{ijkl} is a fourth-rank tensor with $3^4 = 81$ elements and can be represented by a $3 \times 3 \times 3 \times 3$ matrix, etc.

If the current density *is* proportional to the applied electric field [relaxing observation (a)], then a linear relationship exists and only the second-rank tensor terms need to be retained. That is,

$$J_i = \sum_j \sigma_{ij} E_j \tag{6}$$

or

$$\begin{bmatrix} J_1 \\ J_2 \\ J_3 \end{bmatrix} = \begin{bmatrix} \sigma_{11} & \sigma_{12} & \sigma_{13} \\ \sigma_{21} & \sigma_{22} & \sigma_{23} \\ \sigma_{31} & \sigma_{32} & \sigma_{33} \end{bmatrix} \begin{bmatrix} E_1 \\ E_2 \\ E_3 \end{bmatrix}. \tag{7}$$

If the orthogonal reference directions 1,2,3 are represented by x,y,z, then this may be written as

$$\begin{aligned} J_x &= \sigma_{xx} E_x + \sigma_{xy} E_y + \sigma_{xz} E_z, \\ J_y &= \sigma_{yx} E_x + \sigma_{yy} E_y + \sigma_{yz} E_z, \\ J_z &= \sigma_{zx} E_x + \sigma_{zy} E_y + \sigma_{zz} E_z. \end{aligned} \tag{8}$$

The coefficient σ_{xy}, for example, may be thought of as "the conductivity in the x direction due to an electric field in the y direction," and so forth. Just as Eq. (5) is a general relationship between two dependent vectors, Eq. (6) is the general *linear* relationship between two dependent vectors.

In writing out the matrix of values that represents a particular tensor, the mutually perpendicular reference axes for the tensor must be oriented in some manner with respect to the crystal axes (which are not necessarily mutually orthogonal). The choice of the x,y,z axes with respect to the a,b,c crystalline axes for the various crystal systems has become standardized.[11] These conventions are listed in Table III.

The conductivity elements σ_{ij} are not necessarily independent of each other. Due to basic thermodynamic considerations, the conductivity tensor σ_{ij} (and all second-rank tensors discussed) is inherently diagonally symmetric ($\sigma_{ij} = \sigma_{ji}$). This is true even in the complete absence of crystal symmetry. The interrelationship between the various tensor elements also depends on the symmetry possessed by the crystal. The physical property (electrical conductivity in this case) must at least possess the symmetry of the crystal structure. It can have more symmetry than the crystal structure but it can have no less symmetry than the crystal structure. This basic principle was first asserted by Neumann in 1833. The application of this principle allows the second-rank conductivity tensor com-

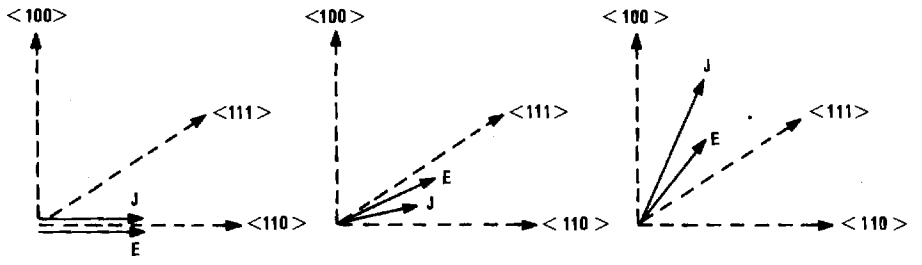

Fig. 2. Resultant current density, **J**, for a given magnitude of electric field applied in several different crystallographic directions. The illustrated behavior is characteristic of *n*-type germanium at high electric fields. The plane of the figure is a (110) plane.

Table III. Conventional orientation of tensor reference axes x,y,z to crystalline axes a,b,c (Ref. 11).

Crystal system	Relative orientation
Triclinic Monoclinic	$y \| \| b$
Tetragonal Trigonal Hexagonal	$x \| \| a,\ z \| \| c$
Orthorhombic Cubic	$x \| \| a,\ y \| \| b,\ z \| \| c$

ponents to be reduced considerably. These results are shown in Table IV. Notice that only for the cubic case does the second-rank conductivity tensor reduce to a simple scalar. That is,

$$\begin{bmatrix} J_1 \\ J_2 \\ J_3 \end{bmatrix} = \begin{bmatrix} \sigma_0 & 0 & 0 \\ 0 & \sigma_0 & 0 \\ 0 & 0 & \sigma_0 \end{bmatrix} \begin{bmatrix} E_1 \\ E_2 \\ E_3 \end{bmatrix}, \tag{9}$$

where $\sigma_0 = \sigma_{11}$. Thus,

$$\mathbf{J} = \sigma_0 \mathbf{E}. \tag{10}$$

Thus for the cubic case, the current density *is* in the same direction as the electric field [relaxing observation (b)]. Furthermore, the magnitude of the current density *does not* vary with crystallographic direction for this case [relaxing observation (c)]. This, of course, is true if only the second-rank tensor is present (linear case) in the expansion given by Eq. (5). The example shown in Fig. 2 is for a cubic crystal, but for high electric field strengths where the higher rank tensor terms cause deviations from Eq. (10). Equation (10) is Ohm's law (analogous to $I = V/R$). For a very large number of practical situations, Ohm's law is valid. That is, the current density is proportional to the applied electric field, is in the same direction as the applied field, and is independent of crystallographic direction.

Table IV. The second-rank conductivity tensor for the various crystal systems.

Crystal system	Second-rank tensor
Triclinic	$\sigma_{ij} = \begin{bmatrix} \sigma_{11} & \sigma_{12} & \sigma_{31} \\ \sigma_{12} & \sigma_{22} & \sigma_{23} \\ \sigma_{31} & \sigma_{23} & \sigma_{33} \end{bmatrix}$
Monoclinic	$\sigma_{ij} = \begin{bmatrix} \sigma_{11} & 0 & \sigma_{31} \\ 0 & \sigma_{22} & 0 \\ \sigma_{31} & 0 & \sigma_{33} \end{bmatrix}$
Orthorhombic	$\sigma_{ij} = \begin{bmatrix} \sigma_{11} & 0 & 0 \\ 0 & \sigma_{22} & 0 \\ 0 & 0 & \sigma_{33} \end{bmatrix}$
Tetragonal Trigonal Hexagonal	$\sigma_{ij} = \begin{bmatrix} \sigma_{11} & 0 & 0 \\ 0 & \sigma_{11} & 0 \\ 0 & 0 & \sigma_{33} \end{bmatrix}$
Cubic	$\sigma_{ij} = \begin{bmatrix} \sigma_{11} & 0 & 0 \\ 0 & \sigma_{11} & 0 \\ 0 & 0 & \sigma_{11} \end{bmatrix}$

VII. ESTIMATING MAGNITUDES OF PHYSICAL EFFECTS

In the previous section it was shown that the electrical conductivity is isotropic in cubic materials for small electric fields. For relatively large electric field strengths, it was also illustrated that additional higher rank tensor terms in Eq. (5) become significant. However, for most common physical situations the higher rank conductivity tensors do not alter the conductivity as described by the linear (second-rank) term.

This basic situation is very common in nature—higher order effects are usually of little consequence. That is, *the magnitude of physical effects usually become smaller for higher rank tensors relating the same physical quantities.* In this section, this is stated as an empirical principle that is potentially useful in estimating the relative magnitudes of various physical effects. It is important to point out that a priori the relative magnitudes of the higher order effects cannot be estimated. It is, however, an experimental fact that these effects usually contribute much less than lower order effects.

A multitude of examples in addition to electrical conductivity can be given to illustrate this empirical principle. Among these is the physical situation in which both an electrical current and a magnetic field are applied to a solid. Just as Eq. (5) can be "inverted" to express electric field in a tensor expansion in powers of current density as

$$E_i = \sum_j \rho_{ij} J_j + \sum_{j,k} \rho_{ijk} J_j J_k + \sum_{j,k,l} \rho_{ijkl} J_j J_k J_l + \cdots, \tag{11}$$

likewise the electric field in the presence of a current density and a magnetic field may be expressed as

$$E_i = \sum_j \zeta_{ij} J_j + \sum_{j,k} \zeta_{ijk} J_j B_k + \sum_{j,k,l} \zeta_{ijkl} J_j B_k B_l + \cdots. \tag{12}$$

If the solid is maintained at a constant temperature, the tensors ζ_{ij}, ζ_{ijk}, and ζ_{ijkl} represent the resistivity, the Hall effect, and magnetoresistivity, respectively (see next section for a detailed discussion). Thus, using the empirical principle stated above, we conclude that, in general, the resistivity will be a larger effect than the Hall effect and that the Hall effect will be a larger effect than magnetoresistivity. This is indeed borne out by experimental results.

Another example would be the comparison of the inverse piezoelectric effect and electrostriction. Both of these effects may be described as strain being induced in a solid owing to the presence of an electric field. From Ta-

ble II it is seen that the inverse piezoelectric effect is described by a third-rank tensor, whereas electrostriction is described by a fourth-rank tensor. Thus, we correctly estimate that the inverse piezoelectric effect is a larger effect than electrostriction.

The relative magnitudes of other physical effects relating the same physical quantities may be estimated in a similar manner. Thus we conclude that the Pockels effect (third-rank tensor) will generally be larger than the Kerr effect (fourth-rank tensor), that optical second-harmonic generation (third-rank tensor) will generally be a larger effect than optical third-harmonic generation (fourth-rank tensor), and so forth.

The empirical principle presented here may thus be used to *estimate* the relative magnitudes of various physical effects interrelating the same quantities. This procedure, though generally valid, sometimes fails because the lower order effect does not exist owing to other physical reasons or owing to requirements imposed by crystal symmetry. In these cases, however, it is frequently known in advance that a lower order effect will not exist. For example, the Pockels effect (third-rank tensor) does not exist in $SrTiO_3$ because its crystal structure possesses inversion symmetry. In this case the Kerr effect (fourth-rank tensor) becomes the dominant effect.

VIII. INTERRELATING PHYSICAL EFFECTS WITH TENSORS

Multiple physical effects may occur simultaneously in a single solid. One physical effect may cause another effect to occur, and so on. If these physical effects are described by tensors, they may frequently be conveniently interrelated to each other through the use of the tensor notation.

As an example of such an interrelation procedure, consider the rectangular solid shown in Fig. 3. A current density has been applied in the (+) x direction and a magnetic field applied in the (+) z direction. The y direction and z direction are open circuited so that no current can flow in those directions. This is the basic geometry used in making Hall effect measurements. However, in general, other effects may also occur simultaneously in the solid. The most important effects occurring in this configuration are listed in Table V.

To determine the interrelationship between these effects, the physical situation in the solid may be analyzed in terms of the applied and generated physical quantities in the solid. A step-by-step sequential procedure can be used to describe the physical effects which are present at each step in terms of the physical quantities which were found to be present from previous steps.

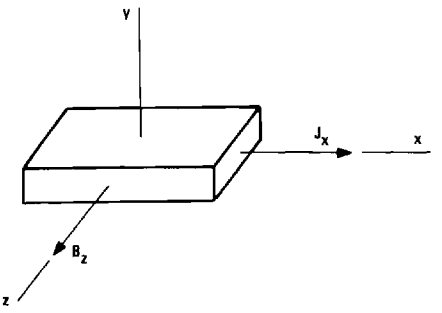

Fig. 3. Geometrical configuration of a solid with an applied current density (x direction) and an applied magnetic field (z direction).

Table V. Conductivity, galvanomagnetic, and thermoelectric effects that may occur when an electrical current and a magnetic field are applied at right angles to each other in a solid.

	Rank of tensor	Tensor element needed[a]	Defining tensor equation
Conductivity effect			
Electrical resistivity	2	ρ_{xx}	$E_x = \rho_{xx} J_x$
Galvanomagnetic effects			
Hall effect	3	R_{yxz}	$E_y = R_{yxz} J_x B_z$
Nernst effect	3	Q_{xyz}	$E_x = Q_{xyz}\, dT/dy\, B_z$
Ettingshausen effect	3	P_{yxz}	$dT/dy = P_{yxz} J_x B_z$
Righi–Leduc effect	3	A_{xyz}	$dT/dx = A_{xyz}\, dT/dy\, B_z$
Magnetoresistivity effect	4	M_{xxzz}	$E_x = M_{xxzz} J_x B_z^2$
Thermoelectric effect			
Seebeck effect	2	S_{yy}	$E_y = S_{yy}\, dT/dy$

[a] E = electric field; J = current density; B = magnetic flux density; T = temperature.

Initially a current density, J_x, is applied in the x direction and a magnetic flux density, B_z, is applied in the z direction. From Table V it is seen that four of the effects are present owing to these applied physical quantities. These four (electrical resistivity, Hall effect, Ettingshausen effect, and magnetoresistivity) are the effects which depend only on J_x and B_z. These represent the first four steps in the sequential procedure.

(i) An electric field is generated in the x direction owing to the current density in the x direction and the electrical resistivity:

$$E_{x1} = \rho_{xx} J_x . \tag{13}$$

(ii) An electric field is generated in the y direction owing to the current density in the x direction, the magnetic field in the z direction, and the Hall effect:

$$E_{y1} = R_{yxz} J_x B_z . \tag{14}$$

(iii) An additional electric field is generated in the x direction owing to the current density in the x direction, the magnetic field in the z direction and the magnetoresistivity effect:

$$E_{x2} = M_{xxzz} J_x B_z^2 . \tag{15}$$

If experimentally no thermal gradients are allowed to form (the isothermal case, approximated by immersing the sample in a constant-temperature, high-thermal-conductivity surrounding), then to the fourth-rank tensor term the electric fields are

$$E_x = E_{x1} + E_{x2},$$

$$E_y = E_{y1}$$

or

$$E_x = (\rho_{xx} + M_{xxzz} B_z^2) J_x, \tag{16}$$

$$E_y = R_{yxz} B_z J_x. \tag{17}$$

These results for E_x and E_y represent the first three terms (second-, third-, and fourth-rank tensor terms) of Eq. (12) for the isothermal case and the geometry of Fig. 3. These electric fields are the usual quantities which are measured in an experiment, and thus an understanding of them is essential if experimental results are to be properly interpreted.

If, on the other hand, the material is isolated from its surroundings, thermal gradients will form via the Ettingshausen and Righi–Leduc effects. This is the adiabatic case and is approximated by leaving the sample in air or more accurately by putting it in a vacuum.

(iv) A temperature gradient is generated in the y direction due to the current density in the x direction, the magnetic field in the z direction, and the Ettingshausen effect:

$$\frac{dT}{dy} = P_{yxz} J_x B_z. \tag{18}$$

This temperature gradient produces additional electric fields via the Seebeck and Nernst effects.

(v) An additional electric field is generated in the y direction owing to the temperature gradient in the y direction and the Seebeck effect:

$$E_{y2} = S_{yy} \frac{dT}{dy}. \tag{19}$$

By using the above expression for dT/dy, this becomes

$$E_{y2} = S_{yy} P_{yxz} J_x B_z. \tag{20}$$

(vi) An additional electric field is generated in the x direction owing to the thermal gradient in the y direction, the magnetic field in the z direction, and the Nernst effect:

$$E_{x3} = Q_{xyz} \frac{dT}{dy} B_z. \tag{21}$$

By using the dT/dy expression from the Ettingshausen effect again, this may be rewritten as

$$E_{x3} = Q_{xyz} P_{yxz} J_x B_z^2. \tag{22}$$

(vii) A temperature gradient is generated in the x direction owing to the temperature gradient in the y direction, the magnetic field in the z direction, and the Righi–Leduc effect:

$$\frac{dT}{dx} = A_{xyz} \frac{dT}{dy} B_z. \tag{23}$$

(viii) An additional electric field is generated in the x direction owing to the temperature gradient in the x direction and the Seebeck effect:

$$E_{x4} = S_{xx} \frac{dT}{dx}. \tag{24}$$

Combining Eqs. (18), (23), and (24) gives

$$E_{x4} = S_{xx} A_{xyz} P_{yxz} J_x B_z^2$$

for the additional electric field in the x direction. Thus, the electric fields to the fourth-rank tensor terms are

$$E_x = E_{x1} + E_{x2} + E_{x3} + E_{x4},$$

$$E_y = E_{y1} + E_{y2}$$

or

$$E_x = [\rho_{xx} + (M_{xxzz} + Q_{xyz} P_{yxz} + S_{xx} A_{xyz} P_{yxz}) B_x^2] J_x, \tag{25}$$

$$E_y = [(R_{yxz} + S_{yy} P_{yxz}) B_z] J_x. \tag{26}$$

These results represent the first three terms (second; third; and fourth-rank tensor terms) of Eq. (12) for the adiabatic case and the geometry of Fig. 3. These results along with the results for the isothermal case are tabulated in Table VI.

For the constant-temperature case, the second-, third-, and fourth-rank tensors represent the resistivity, the Hall effect, and magnetoresistivity, respectively. In the adiabatic case, the development of temperature gradients complicates the interpretation of the third- and fourth-rank tensor terms as indicated in Table VI. In these cases additional terms are present. These new terms are usually quite small and are therefore ignored. However, in some

Table VI. Physical interpretation of the tensor terms in Eq. (12).

	Physical interpretation[a]	
Tensor term	Isothermal case	Adiabatic case
ζ_{ij}	ρ	ρ
ζ_{ijk}	R	$R + SP$
ζ_{ijkl}	M	$M + QP + SAP$

[a]Subscripts deleted. ρ = resistivity; R = Hall coefficient; M = magnetoresistivity; S = Seebeck coefficient; P = Ettingshausen coefficient; Q = Nernst coefficient; A = Righi–Leduc coefficient.

cases the correction terms must be taken into account. For example, in measuring the Hall effect of a sample, the Hall coefficient may be very small owing to a large concentration of charge carriers or owing to a nearly equal number of electrons and holes in the material. If the sample is in open air (essentially the adiabatic case), thermal gradients will form and the *SP* term may be dominant. Thus what would appear to be a Hall effect measurement may not be at all.

The above procedure may be straightforwardly extended to higher rank tensor terms to determine their interpretation in terms of physical effects. These higher rank tensor terms will modify the interpretation of the measured electric fields by producing additional correction terms. These corrections will generally be completely negligible owing to the high rank of the tensors that describe the underlying physical effects.

[1]J. A. Schouten, *Tensor Analysis for Physicists* (Oxford University, Oxford, 1954).

[2]See, for example, J. L. Synge, *Tensorial Methods in Dynamics* (Toronto University, Toronto, 1936).

[3]Use of tensors introduced by A. Einstein in 1913; see, for example, G. Y. Rainich, *Mathematics of Relativity* (Wiley, New York, 1950).

[4]See, for example, I. S. Sokolnikoff, *Mathematical Theory of Elasticity* (McGraw-Hill, New York, 1946).

[5]Use of tensors introduced by G. Kron in 1934; see, for example, J. W. Lynn, *Tensors in Electrical Engineering* (Arnold, London, 1963).

[6]W. Voigt, *Lehrbuch der Kristallphysik* (Teubner, Leipzig, 1910).

[7]J. F. Nye, *Physical Properties of Crystals* (Oxford University, Oxford, 1957).

[8]C. S. Smith, Solid State Phys. **6,** 175 (1958).

[9]See, for example, H. Callen, Am. J. Phys. **36,** 735 (1968).

[10]See, for example, H. Callen, E. Callen, and Z. Kalva, Am. J. Phys. **38,** 1278 (1970).

[11]Proc. IRE **37,** 1378 (1949).

Unified approach to the formation of phase holograms in ferroelectric crystals*

S. F. Su and T. K. Gaylord

School of Electrical Engineering, Georgia Institute of Technology, Atlanta, Georgia 30332
(Received 16 June 1975; in final form 2 September 1975)

The description of the formation of thick-phase holograms over the entire range of exposures has been accomplished using numerical methods. The internal electric field distributions (and thus the refractive-index profiles for linear electro-optic crystals) generated through diffusion and through drift of charge carriers are calculated. The treatment allows for the presence of an effective electric field due to the photovoltaic effect and an externally applied electric field. The results of this approach reduce to the existing analytic expressions for the limiting cases of the initial and the steady-state stages of hologram formation. This approach establishes the limits of validity for the analytic expressions in terms of exposure and material parameters.

PACS numbers: 42.30.N, 42.40.K, 78.20.J

I. INTRODUCTION

The recording of thick-phase holograms in ferroelectric crystals was first shown in lithium niobate by Chen *et al.*[1] The grating patterns of the holograms were optically induced refractive-index changes in the bulk material. Their work stimulated study of the theory of hologram formation in ferroelectrics. Three different models of the physical mechanisms have been proposed[2–4] to explain the phenomenon of this optically induced refractive-index change. Chen[2] explained the refractive-index change by drift of photoexcited carriers under the influence of an internal electric field. He assumed that there are electron traps in the material. Initially, some of the traps are filled (neutral charge state) and they provide electrons upon photoexcitation. The others are empty and they capture electrons. In addition, he assumed that there is an internal electric field in the direction opposite to that of the spontaneous polarization. The photoexcited electrons drift toward the positive side of the field (or the spontaneous polarization) leaving behind positive charges of ionized trap centers. The photoexcited charges will be retrapped and reexcited out of the traps until they finally drift out of the illuminated region and are trapped. Therefore, a space-charge field is created between the positive ionized centers and the trapped negative charges. This space-charge field causes the spatial variation of the refractive index via the linear electro-optic effect of the sample. The need for an internal field in Chen's model was removed by Glass *et al.*[5] by introducing the concept of a high-field photoeffect. They found that the current inside the crystal is due to a bulk photovoltaic effect and not due to internal fields.

Johnston[3] proposed a light-generated polarization pattern to explain the variation of the refractive index. In his model, an extremely high density of free electrons are required to generate the large field necessary to account for the variation of the refractive index.

Another model has been proposed by Amodei.[4] He has pointed out that charge migration by diffusion is an important factor in holographic recording for sufficiently small grating periods. He has shown that even in the absence of an internal field or an externally applied field, the photoexcited electrons still can migrate out of the illuminated region by thermal processes. Further, he has derived[6] expressions for the electric field patterns generated through diffusion and through drift, respectively, for plane-wave holograms for the cases of the initial and the steady-state stages of holographic recording.

Young *et al.*[7] have generalized Amodei's formulation by removing the assumption that the diffusion length is small compared to a grating period. This treatment applies only to the initial stage of hologram formation.

In this paper, Amodei's model is extended to cover the entire range of exposures in the formation of plane-wave holograms. This is accomplished by a numerical approach and both the diffusion and the drift of charge carriers are included. The electric field distributions generated through these two mechanisms are obtained. The results of this approach reduce to the existing analytic expressions[6] for the limiting cases of the initial and the final steady-state stages of hologram formation. Since analytic expressions for the electric field pattern, in general, cannot be obtained in the intermediate stages of holographic recording, the numerical approach permits the establishment of the limits of validity for the analytic expressions in terms of exposures and material parameters.

II. THEORY

Two plane waves of wavelength λ having angles of incidence upon the medium of $+\theta$ and $-\theta$ produce an interference pattern inside the medium of intensity $I(x) = I_0(1 + m\cos Kx)$, where I_0 is the sum of the intensities (power per unit area transverse to the direction of energy flow) of the two waves, m is the modulation ratio ($0 < m \leq 1$), x is the direction perpendicular to the bisector of the angle between the beams, and $K = 2\pi/L$, where $L = \lambda/2\sin\theta$. Staebler and Amodei[8] have shown for lithium niobate that the electric field patterns, which cause the spatial variation of the refractive index, are generated through both diffusion and drift of photogenerated free electrons (as opposed to holes). Thus the charge carriers will be assumed to be electrons. The method is equally applicable to holes, however. Assuming that the concentration of trapped electrons is sufficiently large so that its variation due to migration

is negligibly small and that the generation rate and trapping time are essentially unchanged during recording, then the concentration of free electrons excited to the conduction band is given by[6]

$$n(x) = \tau g_0(1 + m\cos Kx), \tag{1}$$

where τ is the lifetime of charge carriers and g_0, the generation rate, is given by[6]

$$g_0 = I_0\alpha/hf, \tag{2}$$

where α is the optical absorption coefficient, h is Planck's constant, and f is the light frequency. For an isotropic material (or if the x direction is along one of the crystallographic axes for an anisotropic material), the spatial distribution of the current density at any time is given by

$$J(x,t) = eD_n\frac{dn}{dx} + e\mu_n n[E_0' + E_{sc}(x,t)] + \kappa_1\alpha I, \tag{3}$$

where e is the magnitude of the electronic charge, D_n is the diffusion coefficient for electrons, μ_n is the mobility for electrons, E_0' is the externally applied field (if any), $E_{sc}(x,t)$ is the space-charge field, and κ_1 is a constant depending on the nature of the absorption center and wavelength.[5] The third term on the right-hand side of Eq. (3) represents the photovoltaic effect.[5] Using Eq. (1) and the definition of I, Eq. (3) can be rewritten as

$$J(x,t) = eD_n\frac{dn}{dx} + e\mu_n n[E_0 + E_{sc}(x,t)], \tag{4}$$

where

$$E_0 \equiv E_0' + \frac{\kappa_1\alpha I_0}{e\mu_n\tau g_0}. \tag{5}$$

The last term in Eq. (5) may be regarded as an effective field due to the photovoltaic effect. Using the Einstein relation, $\mu_n/D_n = e/kT$, where k is the Boltzmann constant and T is the absolute temperature, the current density, Eq. (4), can be rewritten as

$$J(x,t) = e\mu_n\left(\frac{kT}{e}\frac{dn}{dx} + n[E_0 + E_{sc}(x,t)]\right). \tag{6}$$

The accumulation rate of the space-charge density ρ at any point and at any time is given by the one-dimensional continuity equation,

$$\frac{\partial\rho(x,t)}{\partial t} = -\frac{\partial J(x,t)}{\partial x}. \tag{7}$$

Combining this with Poisson's equation gives

$$\frac{\partial E_{sc}(x,t)}{\partial x} = \frac{\rho(x,t)}{\epsilon} = -\frac{1}{\epsilon}\int_0^t \frac{\partial J(x,t')}{\partial x}\,dt', \tag{8}$$

where ϵ is the permittivity of the material. Equation (8) cannot be solved analytically except in the limiting case of the initial stage of hologram formation in which $E_{sc}(x,t)$ is neglected in the transport equation. Therefore, a numerical approach was employed to reveal the behavior of $E_{sc}(x,t)$ for the exposures in which $E_{sc}(x,t)$ cannot be neglected in the transport equation. The total space-charge field is $E_{sc}(x,t) \equiv E_{sc}'(x,t) + E_{sc}''(x,t)$, where $E_{sc}'(x,t)$ and $E_{sc}''(x,t)$ are the space-charge fields due to diffusion and drift, respectively. In order to obtain a better insight into the relative importance of diffusion and drift, these two mechanisms are considered separately as follows.

A. Diffusion only (no internal or externally applied field)

In this case, $E_0 = 0$ and $E_{sc}(x,t) = E_{sc}'(x,t)$, therefore Eq. (6) becomes

$$J(x,t) = e\mu_n\tau g_0 \times [-(kT/e)mK\sin Kx + (1 + m\cos Kx)E_{sc}'(x,t)]. \tag{9}$$

The exposure time t is set equal to $p\Delta t$, where p is any positive integer and Δt is a constant increment of the exposure time that is sufficiently small so that the variation of dJ/dx is negligible over the time interval Δt. Then, Eq. (8) reduces to a difference-differential equation,

$$\frac{dE_{sc}(x,p\Delta t)}{dx} = \frac{dE_{sc}(x,(p-1)\Delta t)}{dx} - \frac{1}{\epsilon}\frac{dJ(x,(p-1)\Delta t)}{dx}\Delta t. \tag{10}$$

Substituting Eq. (9) into Eq. (10) with E_{sc} replaced by E_{sc}', we obtain

$$\frac{dE_{sc}'(x,p\Delta t)}{dx} = \frac{dE_{sc}'(x,(p-1)\Delta t)}{dx} + \left(\frac{e\mu_n\tau g_0}{\epsilon}\right) \times\left[\left(\frac{kT}{e}\right)mK^2\cos Kx - (1 + m\cos Kx) \times\frac{dE_{sc}'(x,(p-1)\Delta t)}{dx} + mK\sin(Kx) \times E_{sc}'(x,(p-1)\Delta t)\right]\Delta t. \tag{11}$$

From Eq. (11), together with the boundary condition $E_{sc}'(0,t) = 0$ and the initial condition $\partial E_{sc}'(x,0)/\partial x = 0$, the space-charge field, $E_{sc}'(x,t)$, can be obtained by numerical integration.

B. Drift only (with large dc field)

In this case, there is a dc field that is sufficiently large so that the diffusion component of the current can be neglected compared with the drift component. Therefore, Eq. (6) becomes

$$J(x,t) = e\mu_n\tau g_0(1 + m\cos Kx)[E_0 + E_{sc}''(x,t)]. \tag{12}$$

Letting the exposure time t be equal to $p\Delta t$ and substituting Eq. (12) into Eq. (10) with E_{sc} replaced by E_{sc}'' gives

$$\frac{dE_{sc}''(x,p\Delta t)}{dx} = \frac{dE_{sc}''(x,(p-1)\Delta t)}{dx} + \left(\frac{e\mu_n\tau g_0}{\epsilon}\right) \times\left(mK\sin(Kx)[E_0 + E_{sc}''(x,(p-1)\Delta t)] - (1 + m\cos Kx)\frac{dE_{sc}''(x,(p-1)\Delta t)}{dx}\right)\Delta t. \tag{13}$$

Equation (13) is the difference-differential equation for drift. It can also be solved numerically for $E_0 + E_{sc}''$, provided that the boundary and the initial conditions are specified.

C. Diffusion and drift

When the electric field, E_0 (externally applied field plus effective photovoltaic field), is small such that

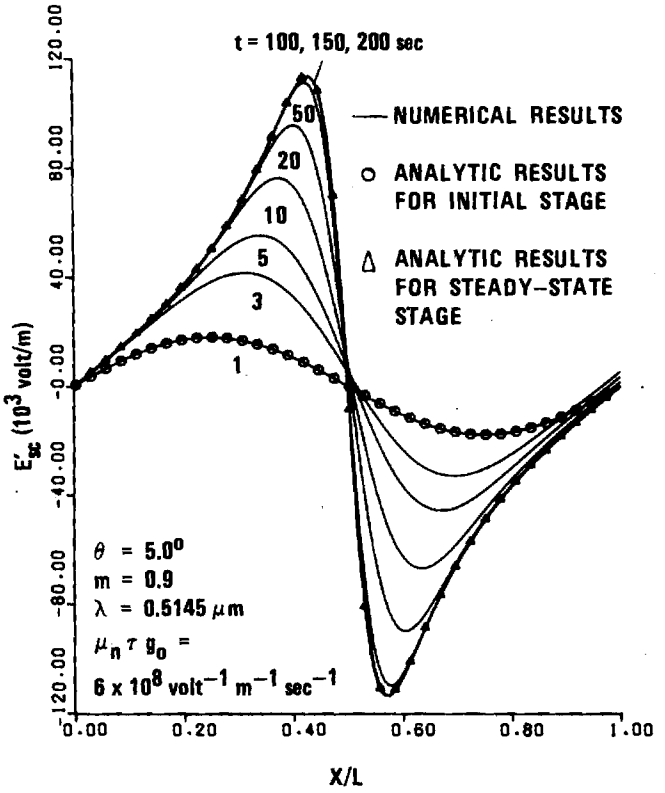

FIG. 1. One grating period of the calculated space-charge field, $E'_{sc}(x,t)$, produced by diffusion.

both the diffusion and drift components are present, the space-charge field is the superposition of the fields due to these two components. That is, $E_{sc} = E'_{sc} + E''_{sc}$. Usually, when the electric field E_0 is several hundred thousand volts per meter, the space-charge field due to diffusion is very small compared with the space-charge field due to drift.

III. RESULTS AND DISCUSSION

Equations (11) and (13) were numerically solved by use of the Runge-Kutta method. As can be seen from these equations the controlling material parameter is $\mu_n \tau g_0/\epsilon$. The low-frequency permittivity ϵ is known for most ferroelectrics as a function of temperature and crystallographic direction. For lithium niobate at room temperature, a typical value is $\epsilon = 30\epsilon_0$, where ϵ_0 is the permittivity of free space. Values for the parameters μ_n and τ are not accurately known. Photoconductivity data for doped lithium niobate[5] imply that the product $\mu_n \tau \approx 10^{-13}$ m^2/V (using $e\mu_n\tau\alpha/hf = 1.4\times10^{-10}$ m/V^2 and $\alpha = 3.8\times10^3$ m^{-1} from Ref. 5). The generation rate g_0 can vary over an extremely wide range depending on the doping and treatment of the sample as well as the intensity of the laser beams. A typical value of $g_0 = 6\times10^{22}$ m^{-3} sec^{-1} is chosen here and thus $\mu_n \tau g_0 = 6\times10^8$ V^{-1} m^{-1} sec^{-1} in this work. The exposure time increment Δt was 1 sec. The space-charge field distribution for diffusion is shown in Fig. 1. Figure 1 shows that for the initial stage of hologram formation (after a 1-sec exposure time in this case), the field distribution is sinusoidal. As the exposure increases, the amplitude of the space-charge field increases and the field distribution becomes nonsinusoidal, and the positions at which the field extrema occur are shifted. However, the field pattern retains odd symmetry at all stages of hologram formation. When the steady-state stage of hologram formation is reached (after about a 100-sec exposure), the amplitude and the distribution of the space-charge field pattern remain fixed and do not change with further exposure. For comparison, the results of the analytic solutions for the initial and the final steady-state stages of hologram formation are also shown in Fig. 1. The circles in Fig. 1 represent the results for the initial stage of hologram formation as obtained from the analytic expression[6]

$$E'_{sc}(x,t) = (1/\epsilon)kT\mu_n\tau g_0 mKt \sin Kx, \tag{14}$$

evaluated for an exposure time of 1 sec with $\mu_n \tau g_0 = 6\times10^8$ V^{-1} m^{-1} sec^{-1}. The triangles in Fig. 1 represent the results for the steady-state stage of hologram formation as obtained from the analytic expression[6]

$$E'_{sc}(x) = (kT/e)(mK \sin Kx)(1 + m\cos Kx)^{-1}, \tag{15}$$

evaluated at room temperature. The comparison shows that the numerical results correctly reduce to the analytic results for the limiting cases. In addition, the limits of validity for Eqs. (14) and (15) are established by the numerical approach in terms of exposure and material parameters. For example, from Fig. 1, it is seen that Eq. (14) is valid when $t \leq 1$ sec and that Eq. (15) is valid when t is near or greater than 100 sec for the parameters used here. Figure 2 presents the behavior of the amplitude of the space-charge field as a function of exposure. The amplitude increases rapidly in the early stages of hologram formation. For $\mu_n \tau g_0$

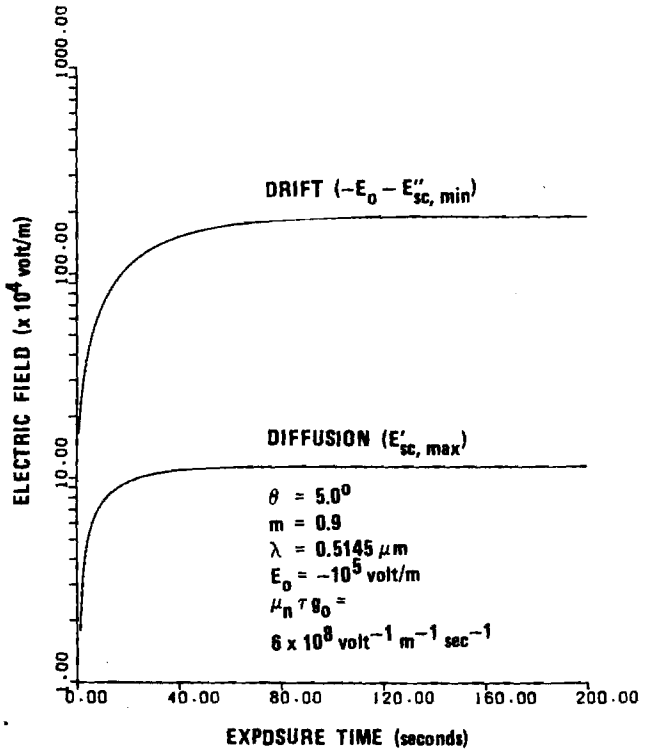

FIG. 2. Calculated values of the space-charge field amplitude produced by diffusion and by drift as a function of exposure time.

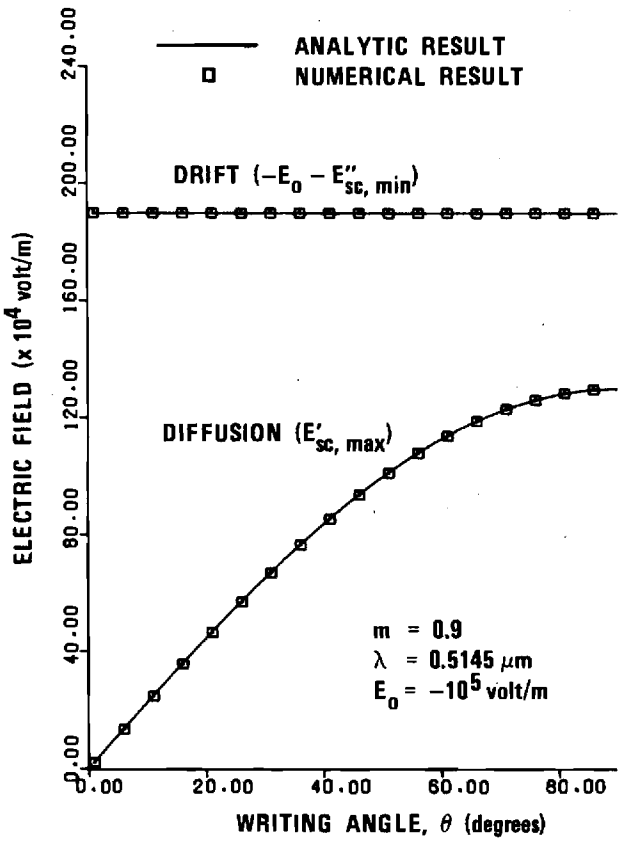

FIG. 3. Calculated steady-state final amplitude of the space-charge field produced by diffusion and by drift as a function of writing angle.

$=6\times10^8$ V^{-1} m^{-1} sec^{-1}, the amplitude begins to saturate near 40 sec of exposure and finally remains unchanged after about 100 sec of exposure. Since the value of g_0 is proportional to I_0 as given by Eq. (2), the limits of validity of Eqs. (14) and (15) depend on I_0 for a given set of material parameters. Larger values of I_0 result in larger values of g_0 and, therefore, shorter exposure times are needed to reach any given exposure. In other words, the amplitude of the field saturates more rapidly for larger values of g_0. Equation (14), for the case of the initial stage of hologram formation, is valid as long as the space-charge field is negligible in the transport equation. Strictly speaking, the space-charge field cannot be neglected at any time except at the very beginning of hologram formation. In the numerical approach, the space-charge field is neglected in the transport equation only for an exposure time of Δt in duration from the beginning of hologram formation. In the calculation of the results here, Δt was chosen to be 1 sec. In fact, other values of Δt can be used, provided that the values of Δt are small enough to assure that there is no appreciable variation in dJ/dx over the time interval Δt. In addition to $\Delta t = 1.0$ sec, the calculations have been performed with $\Delta t = 0.5$ sec and the same resultant electric field patterns are obtained. In general, in order to maintain the same level of numerical accuracy, a smaller value of Δt must be used for a larger value of g_0 for given material parameters, writing angle, and beam modulation ratio.

Figure 3 presents the amplitude of the space-charge field as a function of writing angle in the steady-state stage of hologram formation. The squares in Fig. 3 represent the numerical results, while the solid curve represents the analytic solution. The field amplitude for diffusion increases as writing angle increases (grating period decreases). This is true for all stages of hologram formation though only the steady-state case is shown in Fig. 3. The space-charge field amplitude as a function of the modulation ratio m for the steady-state case is shown in Fig. 4. Again, the results of the numerical method and the analytic solution are represented by the squares and the solid curve, respectively. The field amplitude increases as the modulation ratio increases. This is also true for all other stages of hologram formation.

In the case of drift, the electric field at the boundary is not zero. It depends on the charge density at the surface and the applied voltage across the sample. The electric field at the boundary is assumed to be equal to the dc field E_0 at all times. The shape of the electric field pattern produced is independent of the value of the dc field E_0. The amplitude of the pattern, however, is dependent upon E_0, increasing with increasing E_0. The initial condition for drift is $\partial E''_{sc}(x, 0)/\partial x = 0$. Figure 5 shows the total electric field distribution when drift is dominant. The dc field E_0 is assumed to be -1.0×10^5 V/m. As for the diffusion case, the field distribution is sinusoidal at the initial stage of hologram formation. As exposure increases, the amplitude increases and the field distribution becomes nonsinusoidal and sharply

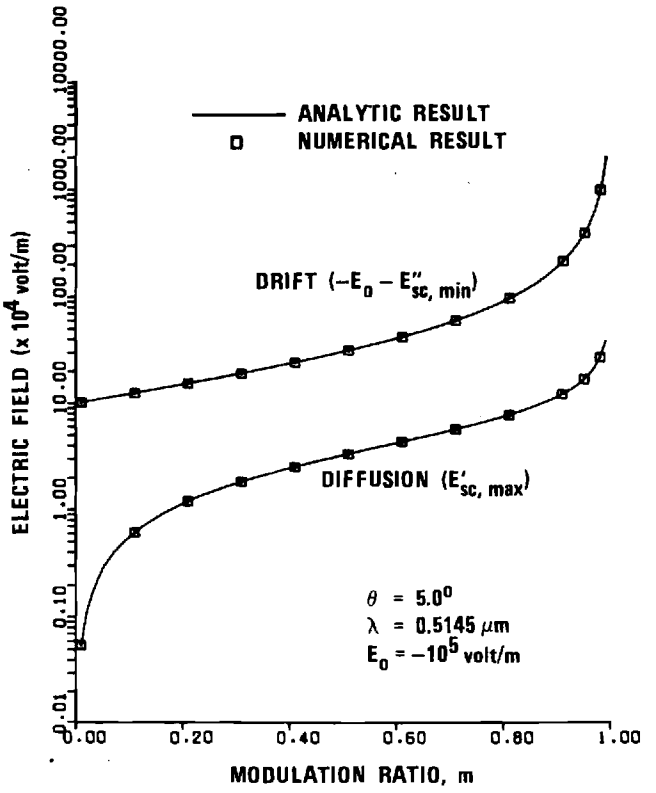

FIG. 4. Calculated steady-state final amplitude of the space-charge field produced by diffusion and by drift as a function of beam modulation ratio.

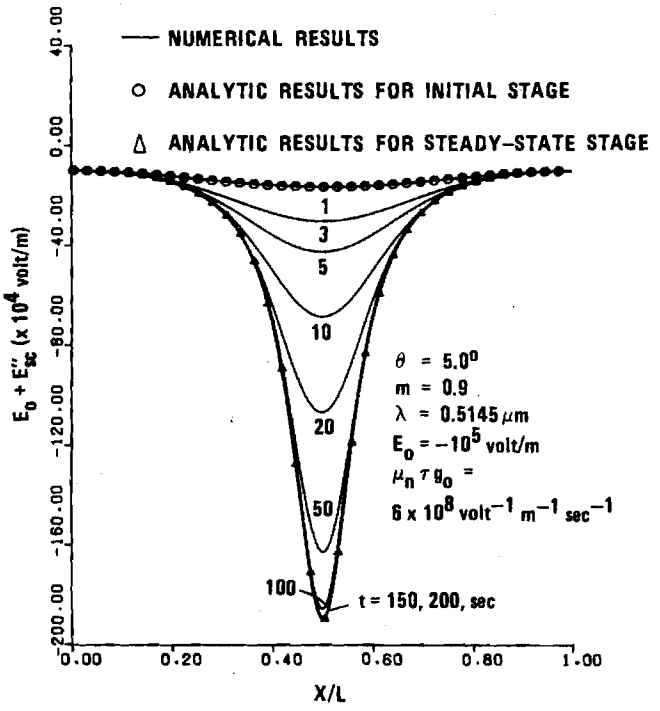

FIG. 5. One grating period of the calculated total electric field, $E(x,t)=E_0+E_{sc}''(x,t)$, produced by drift.

peaked. However, the positions at which the field extrema occur do not shift with exposure. In addition, the field pattern has even symmetry at all times. Also shown in Fig. 5 are the analytic solutions for the electric field distribution at the initial and the steady-state stages of hologram formation. The same value for the electric field at the boundary has been used in these analytic solutions. The circles in Fig. 5 represent the results of the initial stage solution (proportional to $\cos Kx$). The triangles represent the steady-state solution [proportional to $(1+m)/(1+m\cos Kx)$]. The numerical results again correctly reduce to the analytic solutions in these limiting cases of the initial and the steady-state stages of hologram formation. From Fig. 5, it is observed that, for $\mu_n\tau g_0=6\times10^8\ \mathrm{V^{-1}\,m^{-1}\,sec^{-1}}$, the analytic solutions are valid when t is equal to or less than 1 sec for the initial stage of hologram recording and when t is near or greater than 150 sec for the steady-state case. The behavior of the drift electric field amplitude as a function of exposure is also plotted in Fig. 2. The saturation time is about 150 sec for $\mu_n\tau g_0=6\times10^8\ \mathrm{V^{-1}\,m^{-1}\,sec^{-1}}$, which is somewhat longer than that for the diffusion case. Figure 3 contains the steady-state drift electric field amplitude as a function of writing angle. It is observed that the amplitude does not change with the writing angle (and therefore grating period). This is also true for all other stages of hologram formation as well. In Fig. 4, the steady-state drift electric field amplitude as a function of the beam modulation ratio is plotted. It shows that only when the beam modulation ratio is greater than about 0.8 will an appreciable amplitude of the electric field be produced.

These results indicate the following distinctions between the electric field pattern produced by the diffusion mechanism and that produced by the drift mechanism:

(i) The electric field pattern due to diffusion has odd symmetry at all times, whereas the field pattern due to drift has even symmetry at all times.

(ii) For diffusion, the field amplitude increases as writing angle increases (decreasing grating period). For drift, the field amplitude is independent of the writing angle (and grating period).

(iii) The exposure time needed to reach steady state is somewhat longer for drift than for diffusion. In other words, the field due to diffusion saturates more rapidly than the field due to drift.

(iv) In the case of diffusion, the position for the maximum (and minimum) value of the electric field is a function of exposure. In the case of drift, the position for the field maximum (and minimum) remains fixed for all exposures.

(v) There is a 90.0° phase difference between the fundamental Fourier component of the electric field patterns for diffusion and drift for all exposures.

The analysis of this paper is applicable if holes instead of electrons were the charge carriers. For the case of hole charge carriers, the electric field pattern due to diffusion is the same as that produced by electrons except that it is reflected about the $x=0$ axis [$E_{sc}'(x,t)$ becomes $E_{sc}'(-x,t)$]. The electric field patterns due to drift are independent of the type of charge carriers.

The electric field (due to diffusion and/or drift) in ferroelectric lithium niobate causes a spatial modulation of the refractive index via the electro-optic effect. For lithium niobate, the electro-optic effect is linear (Pockels effect). Thus, the amplitude of the modulation of the refractive index is proportional to the magnitude of the electric field. Therefore, the refractive-index pattern caused by the electric field via the electro-optic effect is the same as the electric field pattern calculated here. It follows that the spatial distribution of the refractive index (grating shape) resulting from diffusion is different from that resulting from drift. Since different grating shapes produce different distributions of the higher-order diffraction efficiencies,[9] these higher-order diffraction efficiencies of a hologram grating produced by diffusion are different from those of a hologram grating produced by drift. This indicates the possibility that the physical mechanisms (diffusion and/or drift) that occur during the hologram formation may be determined by measuring the higher-order diffraction efficiencies of a hologram.

IV. CONCLUSIONS

The internal electric field patterns generated by diffusion and drift during hologram recording in ferroelectric crystals were obtained by numerically solving the appropriate difference-differential equations. Unlike previous analytic solutions, this method is applicable for all exposure times. These numerical results reduce to existing analytic results for the limiting cases of the initial and the final steady-state stages of hologram formation. For a given set of material parameters, the

limits of validity of the analytic solutions as well as further distinctions between diffusion and drift have been revealed.

Note added in proof. Calculations of the internal electric field distributions for all stages of hologram development have recently been made using analytical methods. A closed-form solution has been presented by G.A. Alphonse, R.C. Alig, D.L. Staebler, and W. Phillips [RCA Rev. **36**, 213 (1975)] using the assumption that their function G is equal to $e\mu_n \tau g_0 E_0/\epsilon$. Analytical results have also been obtained assuming $E_{sc}(0, t) = 0$ (as in the present work) by W.D. Cornish, M.G. Moharam, and L. Young (unpublished).

*Work supported by the National Science Foundation and by the National Aeronautics and Space Administration.

[1]F.S. Chen, J. T. LaMacchia, and D.B. Fraser, Appl. Phys. Lett. **13**, 223 (1968).
[2]F.S. Chen, J. Appl. Phys. **40**, 3389 (1969).
[3]W.D. Johnston, Jr., J. Appl. Phys. **41**, 3279 (1970).
[4]J.J. Amodei, Appl. Phys. Lett. **18**, 22 (1971).
[5]A.M. Glass, D. von der Linde, and T.J. Negran, Appl. Phys. Lett. **25**, 233 (1974).
[6]J.J. Amodei, RCA Rev. **32**, 185 (1971).
[7]L. Young, W.K.Y. Wong, M.L. W. Thewalt, and W.D. Cornish, Appl. Phys. Lett. **24**, 264 (1974).
[8]D.L. Staebler and J.J. Amodei, J. Appl. Phys. **43**, 1042 (1972).
[9]S.F. Su and T.K. Gaylord, J. Opt. Soc. Am. **65**, 59 (1975).

Determination of physical parameters and processes in hologram formation in ferroelectrics*

S. F. Su and T. K. Gaylord

School of Electrical Engineering, Georgia Institute of Technology, Atlanta, Georgia 30332
(Received 29 January 1976)

The material parameters and physical processes during hologram formation in ferroelectric crystals have previously been identified. Some methods (based largely on new diagnostic techniques) for evaluating these critical parameters and for quantifying the physical processes are summarized here.

PACS numbers: 42.40.Kw, 42.30.Nt, 78.20.Jq

A multitude of applications exist for volume (thick) holograms and gratings. The use of ferroelectric crystals such as lithium niobate for volume holographic recording was established by Chen, LaMacchia, and Fraser.[1] Since then there has been considerable experimentation and analysis involving these materials. The holographic diffraction efficiency has been shown to be very sensitive to the material parameters and the physical processes that are operative in these linear electro-optic materials. The physical processes, in turn, are largely dependent on the recording conditions. Some methods for evaluating the material parameters and quantifying the physical processes are summarized here.

The physical processes occurring during hologram recording are known to be diffusion and drift of electrons.[2,3] The resultant space-charge electric field modulates the index of refraction via the linear electro-optic effect. There may be an effective electric field due to the bulk photovoltaic effect[4] and/or an externally applied electric field during recording. A charge transport analysis[2,5-7] of the holographic recording process in these electro-optic crystals indicates that the controlling parameter is $e\mu_n\tau g_0 t/\epsilon$, where e is the magnitude of the electronic charge, μ_n is the electron mobility, τ is the electron lifetime, g_0 is the electron photogeneration rate, t is the exposure time, and ϵ is the low-frequency dielectric permittivity. The permittivity (a tensor) is well known for any given direction in most crystals. The exposure time t is externally controlled and is thus known. The unknown (and highly variable) factor is therefore $\mu_n\tau g_0$.

The product $\mu_n\tau g_0$ may be calculated via several methods. One method is by evaluation of the exposure parameter u. The exposure parameter, which is defined as $u \equiv \mu_n\tau g_0 t$, may be evaluated from a knowledge of the beam modulation ratio m during recording, the measured fundamental diffraction efficiency DE_1, and the higher-order diffraction efficiencies, DE_2, DE_3, etc. A detailed procedure for determining u is given in Ref. 8. Since the exposure duration t is known, the product $\mu_n\tau g_0$ is then determined by u/t. A second method to obtain the product $\mu_n\tau g_0$ is via a single-beam erasure experiment. The normal decay of the diffraction efficiency η of any hologram from its initial value η_0 under uniform illumination can be shown[5] to be

$$\sin^{-1}(\eta^{1/2})/\sin^{-1}(\eta_0^{1/2}) = \exp(-e\mu_n\tau g_0 t/\epsilon). \quad (1)$$

From measurements of η and η_0, the product $\mu_n\tau g_0$ may be obtained for known t. For small diffraction efficiencies, Eq. (1) reduces to $\eta = \eta_0 \exp(-2e\mu_n\tau g_0 t/\epsilon)$ as given in Ref. 5. A third method to evaluate $\mu_n\tau g_0$ is by measurement of the photoconductivity σ, since $\sigma = e\mu_n n = e\mu_n\tau g_0$, where n is the photogenerated electron concentration.

The photogeneration rate g_0 is proportional to the total intensity I_0 and the optical absorption coefficient α of the crystal. It is given by $g_0 = \alpha I_0/hf$, where h is Planck's constant and f is the optical frequency. Thus, g_0 may be determined from I_0, α, and f. It is difficult to evaluate μ_n and τ separately. The product $\mu_n\tau$ is frequently treated as a single parameter. If g_0 has been obtained, the product $\mu_n\tau$ may be determined using any one of the three methods mentioned previously.

The physical processes of diffusion and drift during hologram recording are conveniently quantified by giving the effective diffusion electric field E_D and the effective internal drift electric field E_0. The field E_D is given by $(kT/e)K$, where k is Boltzmann's constant, T is the absolute temperature during recording, and $K = 2\pi/L$, where L is the grating period. The field E_0 is the sum of an effective bulk photovoltaic field and the applied field (if any). The relative magnitudes of the effective fields are a measure of the relative contributions of diffusion and drift. Thus,

$$\%\ \text{diffusion} = [E_D/(E_D + |E_0|)] \times 100\%, \quad (2)$$

and

$$\%\ \text{drift} = [E_0/(E_D + |E_0|)] \times 100\%. \quad (3)$$

Usually K and T are known and, therefore, E_D can be easily calculated.

The value of E_0 may be evaluated several ways. From a knowledge of the beam modulation ratio during recording and the measured fundamental and higher-order diffraction efficiencies, the field E_0 can be determined.[8] The procedure involves first determining the exposure parameter u and then determining the Fourier components of the refractive-index profile. These Fourier components determine the grating profile. By a best fit of the analytical expression for the space-charge field, which is a function of u and E_0, to the grating profile, the value of E_0 may be determined.

The value of E_0 may also be evaluated via photocurrent measurements. It has been shown[4] that the effective photovoltaic electric field is given by

$$E_0 = \kappa_1 hf / e\mu_n \tau, \quad (4)$$

where κ_1 is a constant that is proportional to the induced photocurrent and is dependent on the impurity centers involved. For example, for iron-doped lithium niobate, Glass *et al.*[4] have found a value of κ_1 to be about 3.0×10^{-11} A m/W. From Eq. (4), E_0 may be evaluated from a knowledge of κ_1, f, and the product $\mu_n \tau$.

A third method for determining E_0 is by direct experimentation. The magnitude of an externally applied electric field (along the c axis) may be varied until the electric field is found that produces the minimum writing sensitivity. In this situation, it is assumed that the external electric field is cancelling the effective internal field E_0, and thus E_0 is equal in magnitude and opposite in direction to the applied field that yields minium sensitivity.

For small exposures which produce sinusoidal or nearly sinusoidal refractive index gratings, the physical processes of diffusion and drift may be quantified by evaluating the parameter ϕ_n, which is the spatial phase difference between the hologram-forming light interference pattern and the resulting refractive-index profile. The range of values for ϕ_n is from 0° (pure drift) to 90° (pure diffusion).[3] For a light interference pattern with a maximum at the coordinate system origin, diffusion contributes sine grating components and drift contributes cosine grating components. The value of the parameter ϕ_n is determined by the relative amplitudes of the fundamental sine grating and the fundamental cosine grating. Specifically, $\phi_n = |\tan^{-1}(n_{s_1}/n_{c_1})|$, where n_{s_1} and n_{c_1} are the fundamental sine and cosine components, respectively. These two quantities may be determined from m, DE_1, DE_2, etc.[8] Therefore, ϕ_n may also be quantified.

For illustration, a hologram was recorded in a 2.12-mm-thick 0.02-mole% iron-doped lithium-niobate crystal possessing an absorption coefficient of 0.37 m^{-1}. The hologram was written with a wavelength of 514.5 nm, a total intensity of 8.77 mW/mm^2, external angles of incidence of $\pm 5.00°$, a recording time of 187 sec, polarization in the plane of incidence, a modulation ratio of 0.994, and no applied electric field. For this case, it was determined by the methods summarized in this letter that $u = 4.74 \times 10^8$ $V^{-1} m^{-1}$ (using $\epsilon = 30\epsilon_0$, where ϵ_0 is the permittivity for free space), $g_0 = 8.39 \times 10^{21}$ $m^{-3} sec^{-1}$, $\mu_n \tau = 3.04 \times 10^{-16}$ $V^{-1} m^2$, $E_D = 5.50 \times 10^4$ V m^{-1}, $E_0 = -1.06 \times 10^5$ V m^{-1}, $\phi_n = 27.3°$, % diffusion = 34%, and % drift = 66%. An external electric field during recording applied in the $+c$ or $-c$ directions was found, respectively, to subtract or to add to E_0. This changes the relative contributions of diffusion and drift. In addition, the diffraction efficiencies, the Fourier grating components, and ϕ_n also are changed by the application of an electric field during recording.

*Work supported by the National Science Foundation and by the National Aeronautics and Space Administration.

[1]F.S. Chen, J.T. LaMacchia, and D.B. Fraser, Appl. Phys. Lett. **13**, 223 (1968).
[2]J.J. Amodei, RCA Rev. **32**, 185 (1971).
[3]D.L. Staebler and J.J. Amodei, J. Appl. Phys. **43**, 1042 (1972).
[4]A.M. Glass, D. von der Linde, and T.J. Negran, Appl. Phys. Lett. **25**, 233 (1974).
[5]G.A. Alphonse, R.C. Alig, D.L. Staebler, and W. Phillips, RCA Rev. **36**, 213 (1975).
[6]W.D. Cornish, M.G. Moharam, and L. Young, J. Appl. Phys. (to be published).
[7]S.F. Su and T.K. Gaylord, J. Appl. Phys. **46**, 5208 (1975).
[8]S.F. Su and T.K. Gaylord, Appl. Opt. (to be published).

Reprinted from **Applied Optics**, Vol. 15, page 1947, August 1976

Refractive-index profile and physical process determination in thick gratings in electrooptic crystals

S. F. Su and T. K. Gaylord

A method for determining the refractive index profile of thick phase gratings in linear electrooptic crystals is presented. This method also determines the effective photovoltaic electric field and the relative contributions of diffusion and drift during hologram recording. The method requires only a knowledge of the modulation ratio during hologram recording and the fundamental and the higher-order diffraction efficiencies of the grating. As an illustration of the method, the refractive index profile, the effective photovoltaic field, and the relative contributions of diffusion and drift are determined from experimental measurements for a lithium niobate holographic grating.

I. Introduction

Volume (thick) holographic gratings have numerous applications. They can be used as highly efficient diffraction gratings, narrowband spectral filters, thick grating optical components such as lenses, imaging systems capable of spectral resolution of extended objects, and as a variety of components in integrated optics. The materials used for recording volume holograms, in general, exhibit light-induced changes in refractive index (photorefractive effect) or changes in optical absorption or both. Photorefractive materials include linear electrooptic crystals such as lithium niobate. In these materials, a sinusoidal light intensity pattern does not necessarily produce a sinusoidal change in the index of refraction or a change that is in phase with the recording intensity pattern. Depending on the crystals, the details of exposure, and the physical mechanisms in the process of hologram recording, different grating profiles and different spatial phase shifts may be generated.[1-4] Therefore, in the study of microscopic physical processes in these optically induced phase gratings, a knowledge of the resultant gratings is of fundamental importance.

In this paper, a method for determining the grating profile of thick gratings in linear electrooptic crystals is presented. This method also determines the effective photovoltaic field and the relative contributions of diffusion and drift during hologram recording. The method requires only a knowledge of the modulation ratio during hologram recording and the fundamental and the higher-order diffraction efficiencies of the grating. Thus, simple external measurements reveal the microscopic internal properties.

To test the calculational accuracy of the method, the refractive index profiles of thick gratings are determined from the calculated diffraction efficiency data for some known grating profiles. Comparison of the determined profiles to the original profiles verifies that the method is very accurate. Further, as an illustration of the method, the refractive index profile, the effective photovoltaic field, and the relative contributions of diffusion and drift are determined from experimental measurements for a lithium niobate holographic grating.

II. Model

The geometry used for a thick optically induced grating is presented in Fig. 1. The $+x$ direction is chosen to coincide with the $+c$ axis direction of the crystal and is in the plane of incidence and parallel to the surfaces of the crystal, the y axis is perpendicular to the page, and the z axis is perpendicular to the surfaces of the crystal. The crystal is assumed to be lossless, and the grating is assumed to be a pure phase grating. The light intensity producing the grating is the sinusoidal interference pattern produced by the intersection of two plane waves and is given by

$$I(x) = I_0(1 + M\cos Kx), \tag{1}$$

where I_0 is the sum of the intensities of the two waves, $K = 2\pi/L$, L is the grating period given by $L = \lambda/2\sin\theta$, λ is the free space wavelength of the writing beams, θ is the angle of incidence, and M is the modulation ratio. The physical processes through which the grating is generated are known to be diffusion and drift of pho-

The authors are with Georgia Institute of Technology, School of Electrical Engineering, Atlanta, Georgia 30332.
Received 28 February 1976.

toexcited electrons.[5] Also, an externally applied electric field and/or an effective photovoltaic field[2,6] may exist during the process of hologram recording. The grating profile inside the crystal is periodic (but not necessarily sinusoidal) in the x direction. For simplicity, the grating is assumed to be uniform in the z direction.

III. Determination of the Refractive Index Profile

A. Theoretical Analysis

The space-charge electric field patterns, and therefore the grating profiles, generated through diffusion and drift of electrons, can be obtained for any given wavelength, exposure, material parameters, and geometrical configuration either by analytical methods[2,3] or by numerical methods.[4] An analytical expression for the space-charge field patterns can be shown to be

$$E_{sc}(x,t) = [(kT/e)MK \sin Kx + ME_0(1 - \cos Kx)](1 + M\cos Kx)^{-1} \times \{1 - \exp[(-e\mu_n \tau g_0 t/\epsilon)(1 + M\cos Kx)]\}, \quad (2)$$

where k is Boltzmann's constant, T is the absolute temperature, e is the magnitude of the electronic charge, μ_n is the electron mobility, τ is the lifetime of the photoexcited electrons, g_0 is the electron photogeneration rate, t is the exposure time, ϵ is the permittivity of the crystal, and E_0 is the effective electric field during hologram recording, which is the sum of the effective photovoltaic field and an externally applied field (if any). When multiplied by an appropriate electrooptic coefficient, Eq. (2) becomes a general expression for the grating profiles. The term containing $\sin Kx$ in Eq. (2) is due to diffusion, and the term containing $(1 - \cos Kx)$ is due to drift. From Eq. (2), it is seen that, for a given wavelength and geometrical configuration in holographic recording, the controlling parameters are E_0 and $\mu_n \tau g_0 t/\epsilon$. The permittivity (a tensor) is well known for any given direction in most crystals. The exposure time t is externally controlled and is thus also known. Without accurate measurements of the material parameters in advance, the values of E_0 and $\mu_n \tau g_0$ are usually not known during the process of holographic recording. Therefore, with E_0 and $\mu_n \tau g_0$ unknown, Eq. (2) does not represent any particular grating profile but a family of grating profiles. However, Eq. (2) contains information about the allowed profiles. From Eq. (2), it is seen that the grating profiles generated through diffusion of electrons have odd symmetry with respect to $x = 0$ (intensity maximum during recording) and can be represented by a sine series. Likewise, the grating profiles generated through drift have even symmetry with respect to $x = 0$ and can be represented by a cosine series. The refractive index modulation amplitude, which is proportional to $E_{sc}(x)$ at any time, is periodic and can be written as a Fourier series

$$\Delta n(x) \equiv n(x) - n_0 = \sum_{h=1}^{\infty} [n_{sh} \sin(hKx) + n_{ch} \cos(hKx)], \quad (3)$$

where $n(x)$ is the grating refractive index profile, n_0 is the average value of $n(x)$, and n_{sh} and n_{ch} are the amplitudes of higher-order harmonic gratings due to diffusion and drift, respectively. The subscripts s, c, and h denote the quantities associated with the sine gratings, the cosine gratings, and the hth-harmonic grating, respectively. By use of Eq. (2), it can easily be shown that the higher-order harmonic gratings, n_{sh} and n_{ch}, can be expressed in terms of their corresponding fundamental gratings as

$$n_{sh} = n_{s1} f_{sh} = n_{s1} \int_0^{2\pi} g_1(v) \sin(hv) dv \Big/ \int_0^{2\pi} g_1(v) \sin v dv, \quad (4)$$

and

$$n_{ch} = n_{c1} f_{ch} = n_{c1} \int_0^{2\pi} g_2(v) \cos(hv) dv \Big/ \int_0^{2\pi} g_2(v) \cos v dv, \quad (5)$$

where

$$g_1(v) = \sin v(1 + M\cos v)^{-1}\{1 - \exp[(-eu/\epsilon)(1 + M\cos v)]\}, \quad (6)$$

and

$$g_2(v) = (1 - \cos v)(1 + M\cos v)^{-1} \times \{1 - \exp[(-eu/\epsilon)(1 + M\cos v)]\}, \quad (7)$$

where $u \equiv \mu_n \tau g_0 t$ and $v \equiv Kx$. From Eqs. (4)–(7), it is observed that f_{sh} and f_{ch} are independent of E_0 and K. They are functions of M and u only. That is, for a given value of M, $f_{sh} = f_{sh}(u)$ and $f_{ch} = f_{ch}(u)$. Using this property and the expression for diffraction efficiency,[7] the grating profile of a thick grating can be determined.

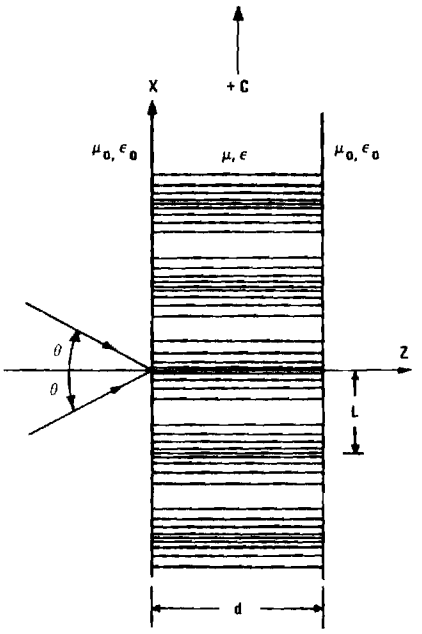

Fig. 1. Geometry of thick grating showing recording beams. The spatial modulation of the refractive index is indicated by the line pattern.

B. The Method

By the method of Ref. 7, the mth-order diffraction efficiency for an E mode incident wave (wave polarized in plane of incidence) of free space wavelength λ' at the mth-order Bragg angle θ_m can be shown to be

$$DE_m = \sin^2\Bigg(\Bigg\{\Bigg[\sum_h^m \Bigg[\frac{L^{(m_h-1)}}{(m_h-1)!(h)^{(m_h-1)}}\Bigg]^2 \times \Bigg(\frac{\{[(n_{sh})^2+(n_{ch})^2]^{1/2}\}^{m_h}}{(\lambda')^{(2m_h-1)}}\Bigg)(n_0)^{(m_h-1)}\cos[m_h\tan^{-1}(n_{sh}/n_{ch})]\Bigg]^2 + \Bigg[\sum_h^m \Bigg[\frac{L^{(m_h-1)}}{(m_h-1)!(h)^{(m_h-1)}}\Bigg]^2 \Bigg(\frac{\{[(n_{sh})^2+(n_{ch})^2]^{1/2}\}^{m_h}}{(\lambda')^{(2m_h-1)}}\Bigg) \times (n_0)^{(m_h-1)}\sin[m_h\tan^{-1}(n_{sh}/n_{ch})]\Bigg]^2\Bigg\}^{1/2}\frac{\pi d\cos(2\theta_m)}{\cos\varphi_m}\Bigg), \quad (8)$$

where φ_m is the refraction angle given by $\varphi_m = \sin^{-1}[(\sin\theta_m)/n_0]$, and m_h is an integer representing the m_hth mode (with respect to the hth-harmonic grating) excited due to the hth-harmonic grating. The symbol

$$\sum_h^m$$

denotes the summation over all the values of h that divide evenly into the integer m. A detailed discussion of the relationships among the integers m, h, and m_h is given in Ref. 7 for both exact Bragg conditions and nearly exact Bragg conditions. The quantities n_0, λ', θ_m, and DE_m ($m = 1, 2, 3, \cdots$) are now given, and the Fourier components n_{sh} and n_{ch} ($h = 1, 2, 3, \cdots$) are the quantities to be determined. The grating period, if not given, can be obtained by $L = \lambda'/2\sin\theta_1$.

From Eq. (8), the first- and second-order diffraction efficiencies are

$$DE_1 = \sin^2\{[(n_{s1})^2 + (n_{c1})^2]^{1/2}\pi d\cos(2\theta_1)/(\lambda'\cos\varphi_1)\}, \quad (9)$$

and

$$DE_2 = \sin^2[(\{L^2n_0[(n_{c1})^2 - (n_{s1})^2]/(\lambda')^2 + n_{c2}]^2 + [2L^2n_0n_{s1}n_{c1}/(\lambda')^2 + n_{s2}]^2)^{1/2}\pi d\cos(2\theta_2)/(\lambda'\cos\varphi_2)]. \quad (10)$$

Substituting Eqs. (4) and (5) into Eq. (10) with $h = 2$ gives

$$DE_2 = \sin^2[(\{L^2n_0[(n_{c1})^2 - (n_{s1})^2]/(\lambda')^2 + n_{c1}f_{c2}]^2 + [2L^2n_0n_{s1}n_{c1}/(\lambda')^2 + n_{s1}f_{s2}]^2)^{1/2}\pi d\cos(2\theta_2)/(\lambda'\cos\varphi_2)]. \quad (11)$$

Since the values of f_{s2} and f_{c2} can be calculated for any given value of u via Eqs. (4) and (5), n_{s1} and n_{c1} can be obtained for the same value of u by solving Eqs. (9) and (11) simultaneously. Thus, solving Eqs. (9) and (11) using a particular value of u, say u_1, we get a pair of solutions denoted by $n_{s1}(u_1)$ and $n_{c1}(u_1)$. The signs of $n_{s1}(u_1)$ and $n_{c1}(u_1)$ must be carefully chosen.[8,9] Once $n_{s1}(u_1)$ and $n_{c1}(u_1)$ are obtained, the corresponding higher-order Fourier components, $n_{sh}(u_1)$ and $n_{ch}(u_1)$, $h = 2, 3, \cdots$, can be obtained by Eqs. (4) and (5). With this set of Fourier components, the corresponding set of higher-order diffraction efficiencies $[DE_m(u_1), m = 3, 4, \cdots]$ are calculated. This entire process [starting from solving Eqs. (9) and (11)] is then repeated for other values of u. Using numerical techniques, a search is made for the particular u, say u_p, that gives the calculated higher-order diffraction efficiencies best matching the initially given values. The corresponding Fourier components $n_{sh}(u_p)$ and $n_{ch}(u_p)$, $h = 1, 2, 3, \cdots$, are the solutions desired, and the refractive index profile is obtained by inserting $n_{sh}(u_p)$ and $n_{ch}(u_p)$ into Eq. (3).

C. Calculational Accuracy of the Method

The method was numerically implemented and tested by determining the Fourier components of three typical gratings from the calculated diffraction efficiencies [using Eq. (8)] of these gratings. The first few orders of the Fourier components of the refractive index profile of these gratings are listed in the original rows in Table I. The diffraction efficiencies of these gratings are calculated with $\lambda' = 514.5$ nm. With these diffraction efficiency data, the Fourier components of the refractive index profile of the gratings are then determined using the foregoing method. The Fourier components determined are listed in the calculated rows in Table I. From Table I, it is seen that the method yields excellent numerical accuracy. Other reading wavelengths ($\lambda' = 488.0$ nm and $\lambda' = 632.8$ nm) have also been used to perform these calculations, and similar results were obtained. This shows that the reading wavelength λ' used in the method does not necessarily have to be equal to the writing wavelength λ and that the refractive index profile determined is independent of the reading wavelength.

D. Effect of Diffraction Efficiency Errors

In practice, the diffraction efficiencies are measured values, and, therefore, some experimental error is unavoidable. These experimental errors will affect the refractive index profile determined by the method. However, if the errors are small, a reasonably accurate grating profile can still be obtained. This is illustrated in Fig. 2. The central curve in Fig. 2 represents the actual profile of a grating. The other curves in Fig. 2 represent the grating profiles determined from dif-

Table I. Comparison of the Original Fourier Components and the Calculated Fourier Components of the Gratings Generated through Diffusion of Electrons, Drift of Electrons, and a Combination of the Two[a]

Physical mechanism		Refractive index Fourier component ($\times 10^{-5}$)									
		n_{c1}	n_{s1}	n_{c2}	n_{s2}	n_{c3}	n_{s3}	n_{c4}	n_{s4}	n_{c5}	n_{s5}
Diffusion	Original	0.000	−6.842	0.000	4.216	0.000	−2.566	0.000	1.536	0.000	−0.900
	Calculated	0.000	−6.842	0.000	4.216	0.000	−2.566	0.000	1.536	0.000	−0.899
Drift	Original	−4.997	0.000	2.988	0.000	−1.755	0.000	1.009	0.000	−0.566	0.000
	Calculated	−4.997	0.000	2.988	0.000	−1.755	0.000	1.009	0.000	−0.566	0.000
Diffusion and drift	Original	−4.997	−6.842	2.988	4.216	−1.755	−2.566	1.009	1.536	−0.566	−0.900
	Calculated	−4.997	−6.842	2.988	4.216	−1.755	−2.566	1.009	1.536	−0.566	−0.899

[a] The grating parameters are $n_0 = 2.243$ and $L = 3.6303$ μm.

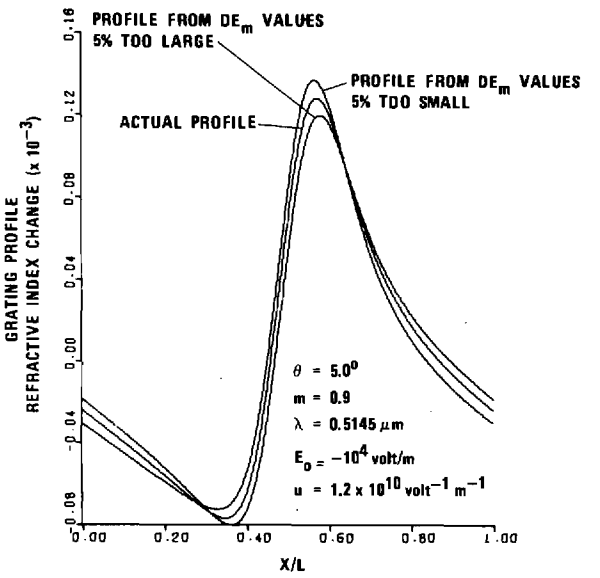

Fig. 2. One grating period of the refractive index profile determined from diffraction efficiencies that are (a) 5.0% too large and (b) 5.0% too small compared to the actual profile.

fraction efficiencies which are 5% higher and 5% lower than those corresponding to the actual profile. From Fig. 2, it is observed that a several percent systematic error in the diffraction efficiencies results in a small change in the grating profile determined by the method. In addition to the grating profile presented in Fig. 2, other grating profiles produced with smaller exposure parameters have also been analyzed. It is found that the error in the grating profile decreases with decreasing exposure parameters. If, instead of a systematic error, a random error of the same standard deviation is present, the determined profile similarly approximates the actual profile.

E. Effect of Boundary Reflections

The effect of boundary reflections was not included in the foregoing analysis. To include this, the measured diffraction efficiency at each Bragg angle must be corrected by dividing by the appropriate transmittance factor τ_m. When the surfaces of the grating are perfectly flat and perfectly parallel, this transmittance factor for the mth-order diffraction is given by[10]

$$\tau_m = (1 - R_m)^2[1 + 2R_m \cos(2\beta_m d) + (R_m)^2]/[[1 - (R_m)^2]^2 + 4(R_m)^2[\cos^2(2\nu_m d) + \cos^2(2\beta_m d)] - 4R_m[1 + (R_m)^2]\cos(2\nu_m d)\cos(2\beta_m d)], \quad (12)$$

where $R_m = \tan^2(\theta_m - \varphi_m)/\tan^2(\theta_m + \varphi_m)$, $\beta_m = 2\pi n_0(\cos\varphi_m)/\lambda'$, and $\nu_m d$ is the argument of the sine squared function in Eq. (8). In most practical cases, the surfaces of the grating are neither perfectly flat nor perfectly parallel. If the cosine factors in Eq. (12) average to zero due to variations in thickness over the illuminated region, the transmittance factor reduces to $\tau_m = (1 - R_m)^2/[1 + (R_m)^2]$.

IV. Determination of Effective Photovoltaic Field and Physical Processes

It has been shown in the preceding section that the refractive index profile of a grating in a linear electrooptic crystal can be determined by knowing the modulation ratio during hologram recording and the fundamental and the higher-order diffraction efficiencies of the grating. The information from Eq. (2) used in determining the grating profile was independent of the effective electric field E_0. Therefore, the value of E_0 can be obtained by a best fit of Eq. (2) to the grating profile determined by the method in the preceding section. The effective photovoltaic field can thus be obtained by subtracting the externally applied field (if any) from E_0.

The physical processes of diffusion and drift during hologram recording are conveniently quantified by the effective diffusion electric field E_D, which is given by $(kT/e)K$, and the effective electric field E_0. The relative magnitudes of the effective fields are a measure of the relative contributions of diffusion and drift. Thus,

$$(\%\ \text{diffusion}) = [E_D/(E_D + |E_0|)] \times 100\%, \quad (13)$$

and

$$(\%\ \text{drift}) = [|E_0|/(E_D + |E_0|)] \times 100\%. \quad (14)$$

V. Experimental Results

For illustration, the refractive index profile of a lithium niobate holographic grating is determined from measurements of its fundamental and higher-order diffraction efficiencies. The holographic grating was recorded in a 2.12-mm thick 0.02-mole% Fe-doped lithium niobate crystal with the grating vector parallel to the c axis of the crystal. The hologram was written with a wavelength of 514.5 nm, a total power density of 8.77 mW/mm^2, external writing angles of ±5.00°, a writing time of 187 sec, polarization in the plane of incidence, a modulation ratio of 0.994, and no externally applied field. The diffraction efficiencies were measured with a low power He–Ne laser ($\lambda' = 632.8$ nm). The measured diffraction efficiencies were $DE_1 = 21.6\%$, $DE_2 = 8.64 \times 10^{-2}\%$, and $DE_3 = 7.74 \times 10^{-3}\%$. When corrected by their corresponding transmittance factors, the diffraction efficiencies became $DE_1 = 29.7\%$, $DE_2 = 0.123\%$, and $DE_3 = 1.08 \times 10^{-2}\%$. These corrected diffraction efficiencies were then used in the method to determine the refractive index profile of the grating. The exposure parameter for this grating was found to be $u_p = 4.74 \times 10^8\ \text{V}^{-1}\text{m}^{-1}$ for $\epsilon = 30\epsilon_0$, where ϵ_0 is the permittivity for free space. The resultant refractive index profile is shown in Fig. 3. This particular grating profile is nearly sinusoidal due to the relatively small exposure. By fitting Eq. (2) to the profile in Fig. 3, it was found that the effective electric field during hologram recording was $E_0 = -1.06 \times 10^5$ V/m (in $-c$ direction). This value is larger than the values reported by Cornish *et al.*[2] but smaller than the values reported by Glass *et al.*[6] The value of E_D was found to be 5.5×10^4 V/m. Thus, (% diffusion) = 34% and (% drift) = 66% for this particular grating.

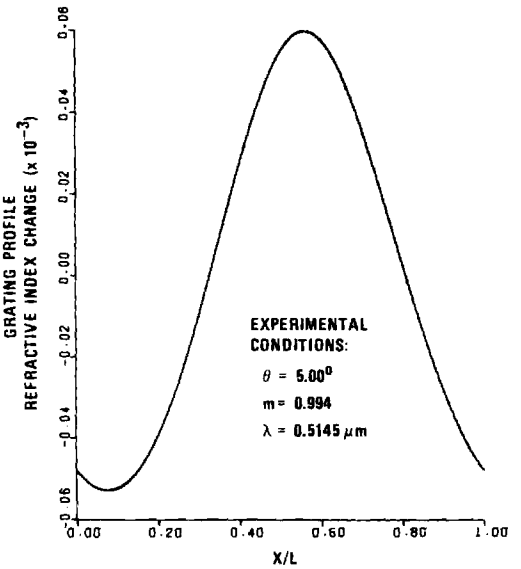

Fig. 3. One grating period of the refractive index profile of a holographic grating recorded in a 2.12-mm thick iron-doped lithium niobate crystal.

For small exposures that produce sinusoidal or nearly sinusoidal refractive index gratings, the physical processes of diffusion and drift may be quantified by evaluating the parameter ϕ_n, which is the spatial phase difference between the hologram-forming light interference pattern and the resulting refractive index profile. The range of values for ϕ_n is from 0° (pure drift) to 90° (pure diffusion).[5] For a light interference pattern with a maximum at the coordinate system origin, diffusion contributes sine grating components, and drift contributes cosine grating components. The value of the parameter ϕ_n is determined by the relative amplitudes of the fundamental sine grating and the fundamental cosine grating. Specifically, $\phi_n = |\tan^{-1}(n_{s1}/n_{c1})|$, where n_{s1} and n_{c1} are the fundamental sine and cosine components, respectively. For this experimental case it was found that $\phi_n = 27.3°$.

Determinations of the grating profile and physical processes have also been performed for gratings recorded in an applied electric field. An external field during recording applied in the $+c$ or $-c$ axis directions of the crystal was found, respectively, to decrease or to increase E_0 and thus to decrease or to increase the relative contribution of drift. The relative drift contribution has been experimentally altered by an external field from essentially 0% to nearly 100%.

VI. Discussion

Because the incident angle of the reading beam cannot exceed 90.0°, the number of higher-order Bragg angles available is limited to the integer that is nearest to, but less than, $2L/\lambda'$. If a suitably short wavelength source is available, the accessibility of higher-order Bragg angles is assured. However, the higher-order diffraction efficiencies are often small, and thus the first three or so orders of the diffraction efficiency are usually sufficient.

The method presented in this paper can also be applied to the case in which the reading beam is polarized perpendicular to the plane of incidence (H mode). It can be shown straightforwardly that the grating profiles determined are independent of the polarization of the reading beam.

The phenomenon of birefringence must, in principle, also be taken into account. Here, the refractive index is a function of the angle of incidence, and, therefore, the appropriate value for the average refractive index must be used in the foregoing formulations. However, for uniaxial crystals (such as lithium niobate), if the crystal is oriented in such a way that its optic axis is parallel to the x axis for the geometry used in this paper (Fig. 1), birefringence appears only in the case of E-mode polarization. In addition, since the amplitude of the spatial modulation of the refractive index would be 10^{-4} or smaller, the error in determining the grating profile is negligible due to the very small variations in the birefringence at different Bragg angles. For example, in the case of lithium niobate at $\lambda' = 514.5$ nm, changes in the amplitude of the fundamental grating do not exceed one tenth of 1% (using $n_0 = 2.337$ and $n_E = 2.243$, where n_0 and n_E are the principal indices of refraction for ordinary and extraordinary waves, respectively).

VII. Conclusions

A method for determining the refractive index profile, the effective electric field, and the physical processes in optically induced thick phase gratings in linear electrooptic crystals has been presented. This method utilizes a knowledge of the allowed family of grating profiles and a knowledge of the modulation ratio during hologram recording and the fundamental and the higher-order diffraction efficiencies of the grating. Thus, simple external measurements reveal the internal properties of the grating.

The authors thank R. Magnusson for his help with the experimental measurements and L. Young for a prepublication copy of Ref. 2. This work was supported by the National Science Foundation and the National Aeronautics and Space Administration.

References

1. J. J. Amodei, RCA Rev. **32,** 185 (1971).
2. W. D. Cornish, M. G. Moharam, and L. Young, J. Appl. Phys. **47,** 1479 (1976).
3. G. A. Alphonse, R. C. Alig, D. L. Staebler, and W. Phillips, RCA Rev. **36,** 213 (1975).
4. S. F. Su and T. K. Gaylord, J. Appl. Phys. **46,** 5208 (1975).
5. D. L. Staebler and J. J. Amodei, J. Appl. Phys. **43,** 1042 (1972).
6. A. M. Glass, D. von der Linde, and T. J. Negran, Appl. Phys. Lett. **25,** 233 (1974).
7. S. F. Su and T. K. Gaylord, J. Opt. Soc. . **65,** 59 (1975).
8. These, of course, depend on the physical properties of the recording materials. For example, for lithium niobate, it can be shown[9] that negative signs must be chosen for both $n_{s1}(u_1)$ and $n_{c1}(u_1)$ when the $+c$ axis of the crystal is directed in the $+x$ reference direction, and that the positive sign for $n_{s1}(u_1)$ and negative sign for $n_{c1}(u_1)$ must be chosen when the $+c$ axis is directed in the $-x$ reference direction. No matter which direction ($+x$ or $-x$) is chosen for the $+c$ axis direction, the same refractive index profile in the lithium niobate crystal is obtained. This shows that there is no ambiguity in the solution.
9. S. F. Su, Ph.D. thesis, Georgia Institute of Technology (1976).
10. H. Kogelnik, J. Opt. Soc. Am. **57,** 431 (1967).

V. DYNAMIC THEORY OF HOLOGRAM FORMATION

Use of dynamic theory to describe experimental results from volume holography*

R. Magnusson and T. K. Gaylord

School of Electrical Engineering, Georgia Institute of Technology, Atlanta, Georgia 30332
(Received 1 July 1975)

The general applicability of dynamic theory to the description of the recording and readout characteristics of volume (thick) hologram gratings is indicated. In dynamic theory (as opposed to static theory), the volume nature of the thick holographic grating allows the interference of an incident light beam with its own diffracted beam inside the recording medium. This effect causes the continuous recording of another grating that alters the initial one, producing a resultant grating that is not uniform through the thickness of the recording material and a grating whose writing and reading characteristics may vary dramatically depending on the recording material and the experimental conditions. A large number of diverse types of writing, reading, and angular selectivity behavior have been reported in the published literature. The dynamic theory of thick hologram writing and reading is shown to predict qualitatively all of these various types of experimental behavior.

PACS numbers: 42.40.D, 42.30.N

I. INTRODUCTION

Thick gratings and thick holograms have numerous applications based on their properties of high diffraction efficiency,[1] wavelength selectivity,[1] angular selectivity,[1] and reduced noise.[2] Thick gratings may be used as highly efficient diffraction gratings, narrow-band spectral filters,[3] thick grating lenses,[4] imaging systems capable of spectral resolution of extended objects,[2] wave guides for surface waves,[5] frequency-selective grating reflectors for thin-film distributed feedback lasers,[6] thin-film waveguide couplers,[7,8] and as deflectors and modulators.[9] Thick (volume) holograms are of interest due to their use in high-capacity information storage,[10] color holography,[11] and in white light reconstruction of holograms.[12]

The static diffraction characteristics of a thick grating have been analyzed by Burckhardt[13] by solving the exact electromagnetic boundary-value problem and by Kogelnik[1] by employing a coupled-wave theory. In these theories, the thick grating is assumed to exist already (as opposed to analyzing the recording process); it is assumed to be uniform through the thickness of the material; and it is assumed to be unaffected by the reconstruction process. These theories have been applied successfully to a large number of experimental situations. There remain, however, numerous types of experimentally observed behavior that are not predicted with these static theories. These include certain writing effects, reading effects, and angular selectivity effects (to be discussed in this paper).

It has been recognized[14] that the volume nature of thick holograms permits the interference of an incident light beam with its own diffracted beam inside the recording medium. This effect causes the continuous recording of a new grating that may add to or subtract from the initial grating producing a resultant grating that is not uniform through the thickness of the material. As is shown in this paper, the explanation of the resulting characteristics, in general, requires a dynamical theory such as that developed by Ninomiya.[15]

Among the materials used for recording volume holograms are those that exhibit light-induced refractive-index changes (photorefractive materials), those that exhibit light-induced changes in optical absorption (photochromic materials), and those that exhibit both of these effects. Numerous recording materials exist in each of these categories.[16]

II. ANALYTICAL TECHNIQUES

The coupled-wave theory used here originated in acoustics.[17] This method has since been adapted to the analysis of volume holograms. Kogelnik[1] analyzed diffraction from sinusoidal hologram gratings and Su and Gaylord[18] analyzed nonsinusoidal gratings. These authors assumed the existence of a uniform grating through the thickness of the medium. Further, they assumed that the hologram grating can be addressed with a light beam without affecting the grating. Thus, these approaches are essentially static.

A more general approach, combining and extending the initial efforts of Kogelnik[1] and Kermisch,[19] has been presented by Ninomiya.[15] He included in the basic coupled-wave formalism, the dynamic behavior of holograms during recording and reading. That is, during recording, the development of the hologram continuously affects the diffraction process (feedback). Similarly, during reading, the incident beam is diffracted inside the medium and the resultant two beams interfere with each other producing changes which may either add to or subtract from the existing holographic grating.

There has been little study of the characteristics of hologram gratings that are not uniform in the direction perpendicular to the hologram surface. Kermisch[20] and Uchida[21] have theoretically analyzed the case of an exponentially attenuated grating, the latter using the coupled-wave approach. In the present work, nonuniformity is shown to occur for photorefractive materials as a result of the spatial phase difference (represented by ϕ_n) between the hologram-forming light interference pattern and the resulting index-of-refraction grating. Also, of course, an attenuated profile is produced if α_0, the average absorption coefficient of the material, is nonzero. It is found that the index profiles can have

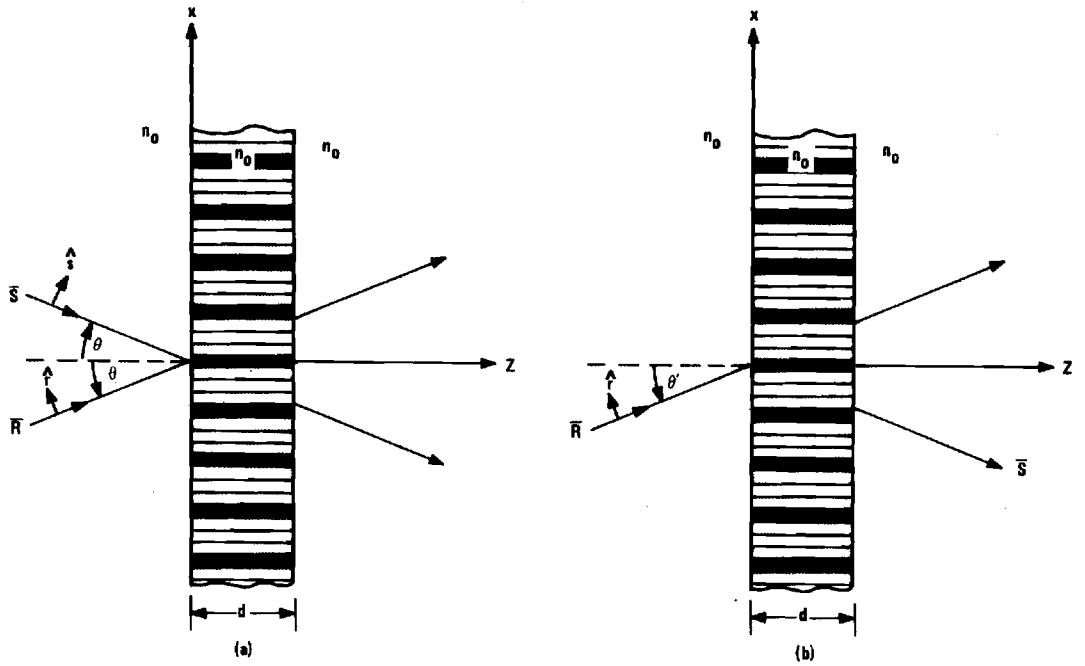

FIG. 1. Model for (a) hologram recording and (b) hologram reading.

many forms in addition to exponential. The above theories[1,15,18–21] have been presented without experimental results.

In this paper, the dynamical coupled-wave equations have been generalized to allow deviations in the angle of incidence and the wavelength, and are given for the *E*-mode polarization. These are then used to calculate the grating profiles and the writing, reading, and angular selectivity characteristics of unslanted phase volume holograms. Numerous types of experimental behavior cited in the literature as well as new experimental results presented here are shown to be predicted by the dynamical theory.

III. MODEL AND DYNAMIC THEORY

A. Model

The thick hologram gratings treated here are assumed to be recorded by the intersection of two coherent light waves in a thick photosensitive medium. They are read by a single wave incident upon the hologram. The recording and reading configurations are shown in Fig. 1. The signal and reference beams represented by the vectors $\mathbf{S}$ and $\mathbf{R}$, respectively, are taken to be infinite plane waves. They are polarized in the plane of incidence of the grating (*E* mode) with polarization vectors $\hat{\mathbf{s}}$ and $\hat{\mathbf{r}}$. The medium is unbounded in the x and y directions. It is to be noted that, during recording, the waves are symmetric in their angle of incidence and, therefore, the grating fringes are normal to the material surface (unslanted). The extension to slanted gratings is straightforward but little additional insight is gained. For convenience, it is assumed that the same average refractive index exists inside and outside the grating (this is a common simplification; see, e.g., Ref. 1) and thus no reflections or deviations occur.

B. Equations

Ninomiya[15] developed the dynamic coupled-wave equations that describe the writing, reading, and erasure of thick holograms for exact Bragg conditons and *H*-mode polarization ($\hat{\mathbf{s}} \| \hat{\mathbf{r}}$). Here the dynamical equations for *E*-mode polarization (electric field in the plane of incidence) are used because the available experimental data are primarily for the *E*-mode configuration. In addition, the equations have been generalized to permit deviations in the incident angle from the writing angle and deviations in the wavelength from the writing wavelength. The notation used here is that of Ninomiya.[15]

Following Ninomiya's development, the wave equation for the total electric field,

$$\nabla^2\mathbf{E} - \nabla(\nabla \cdot \mathbf{E}) + K^2\mathbf{E} = 0, \tag{1}$$

where K is the propagation constant, is used as a starting point. The total electric field in the grating may now be expressed by the vector

$$\mathbf{E}(\mathrm{r},t) = \mathbf{R}(\mathrm{r},t)\exp(-j\boldsymbol{\rho}\circ\mathrm{r}) + \mathbf{S}(\mathrm{r},t)\exp(-j\boldsymbol{\sigma}\circ\mathrm{r}), \tag{2}$$

where $\boldsymbol{\rho}$ and $\boldsymbol{\sigma}$ are the wave vectors of the reference and signal beams, respectively, and $\mathbf{r} = (x,y,z)$. The exposure is thus $\int_0^T \mathbf{E}\cdot\mathbf{E}^*\,dt$, where t is time and T is exposure time. From Eqs. (1) and (2), the following coupled equations are obtained for the wave amplitudes R and S (functions of z and t):

$$\cos\theta\frac{\partial R}{\partial z} + \gamma R = -j\Gamma_1 S(\hat{\mathbf{r}}\cdot\hat{\mathbf{s}})^2, \tag{3}$$

$$\cos\theta\frac{\partial S}{\partial z} + (\gamma + j\vartheta)S = -j\Gamma_2 R(\hat{\mathbf{r}}\cdot\hat{\mathbf{s}})^2, \tag{4}$$

where

$$\gamma = (j2\pi a/\lambda + b)\int_0^T (RR^* + SS^*)\,dt + \alpha_0, \tag{5}$$

$$\Gamma_1 = [(2\pi a/\lambda)\exp(j\phi_n) - jb\exp(j\phi_\alpha)]\int_0^T RS^*\,dt, \tag{6}$$

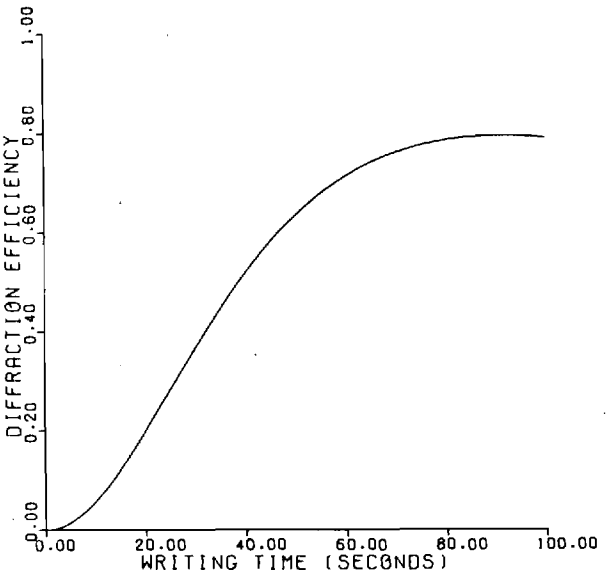

FIG. 2. Calculated hologram writing characteristic exhibiting a saturationlike appearance. Hologram thickness is 2.00 mm, $a = 10^{-12}$ $(\mathrm{V/m})^{-2}$ sec^{-1}, $\phi_n = 90°$, $\alpha_0 = 0$, and other parameters as given in Sec. IV.

$$\Gamma_2 = [(2\pi a/\lambda)\exp(-j\phi_n) - jb\exp(-j\phi_\alpha)]\int_0^T SR^*\,dt, \quad (7)$$

$$\vartheta = (\beta_0^2 - \sigma'^2)/2\beta_0, \quad (8)$$

$$\beta_0 = 2\pi n_0/\lambda, \quad (9)$$

$$\hat{\mathbf{r}}\cdot\hat{\mathbf{s}} = \cos 2\theta, \quad (10)$$

and λ is the free-space wavelength, n_0 is the average index of refraction, α_0 is the average absorption constant, ϕ_n and ϕ_α are the phase differences between the hologram-forming light interference pattern and the resulting refractive-index and absorption gratings, respectively, and a and b are the exposure sensitivities of the refractive-index changes and absorption changes, respectively. The quantity ϑ is the dephasing factor introduced by Kogelnik.[1] The magnitude of the propagation vector of the diffracted wave upon reading is

$$\sigma' = (\beta_\delta^2 - 4\beta_0\beta_\delta\sin\theta\sin\theta' + 4\beta_0^2\sin^2\theta)^{1/2}, \quad (11)$$

where $\beta_\delta = 2\pi m_\delta/\lambda'$. The primed quantities represent the values associated with the reading process.

Equations (3) and (4) can be solved numerically on a digital computer. It is shown that the solutions thus obtained qualitatively describe the various types of externally measurable diffraction behavior of volume holograms that have been experimentally measured and reported in the literature (sometimes with very little explanation).

IV. CALCULATED RESULTS AND EXPERIMENTAL BEHAVIOR

A. Calculational procedure

In this section, numerical results obtained by solving Eqs. (3) and (4) are presented for selected sets of hologram parameters. The solutions are seen to compare favorably with published experimental results. For writing, the equations are solved with $\vartheta = 0$ (no dephasing) and the boundary conditions $R(0,t) = R_0$ and $S(0,t) = S_0$. For reading, ϑ can be nonzero. Deviations in wavelength and/or incident angle from the corresponding writing quantities result in $\vartheta \neq 0$. The boundary conditions $R(0,t) = R_\delta$ and $S(0,t) = 0$ are used for the case of readout with the R beam and $R(0,t) = 0$ and $S(0,t) = S_\delta$ are used for readout with the S beam. Diffraction efficiency is then defined as $\eta = S(1,T)S^*(1,T)/R_\delta^2$ for R-beam readout and $\eta = R(1,T)R^*(1,T)/S_\delta^2$ for S-beam readout.

The computer algorithm employs a fourth-order Runge-Kutta method to solve the equations with respect to the z variable. The integrations in t were performed by replacing the integrals by the corresponding sums and using increments, Δt, small enough for convergence. The actual incremental step sizes used were $\Delta z = 0.01$ (the equations are normalized with respect to the thickness so that $0 \leq z \leq 1$) and $\Delta t = 0.5$ sec. The numerical accuracy was tested by decreasing the step sizes Δz and Δt until the improvements in convergence were insignificant.

The calculations presented are for a 1.66- and a 2.00-mm-thick crystal of $LiNbO_3$ with its optic axis (c axis) in the plane of incidence of the writing beams. The writing and reading waves are polarized in the plane of incidence and have a wavelength of $\lambda = 0.5145$ μm. The angles of incidence for the writing beams are $\pm 2.23°$ (corresponding to external angles of incidence of $\pm 5.00°$ for the grating surrounded by a unity refractive-index medium). For this wavelength, polarization, angle of incidence, and orientation of the lithium niobate crystal, the index of refraction is $n_0 = 2.2426$. For writing $R_0 = S_0 = 1000$ V/m. Reading is done with $R_\delta = 1000$ V/m. Only transmission phase holograms are considered, that is, b is set equal to zero (no photochromic effect).

B. Writing

With a few exceptions, the experimental diffraction efficiency writing characteristics (η vs t) reported in the literature for volume holograms begin with zero initial slope and increase in a parabolic fashion. The magnitudes of the diffraction efficiencies reported, however, vary considerably. Several workers[22–25] report relatively low efficiencies (e.g., $< 1\%$) exhibiting saturating behavior or a very small rate of increase. Others[26–31] have reported higher efficiencies, also showing saturation behavior. At times, instead of saturation, an oscillatory diffraction efficiency is observed.[2,27,28,30,31] It seems that experimental oscillatory writing characteristics are observed primarily for relatively high-efficiency holograms. In many papers,[2,14,24,27,32–38] the writing is terminated before the onset of oscillation or saturation.

The types of behavior indicated above can be straightforwardly predicted using the dynamic theory. The oscillatory behavior is seen to be inherent in the theory because of the assumption of constant refractive-index exposure sensitivity. The material is thus assumed to respond continuously to the interaction of the wave fields at all times. Physically, the quantity a may be time depen-

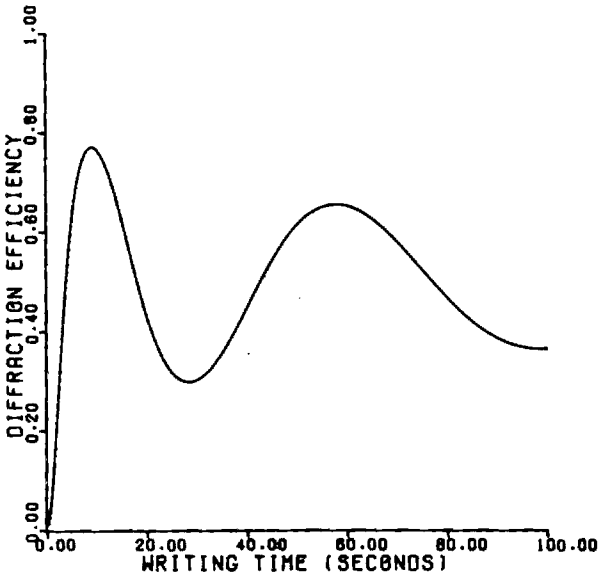

FIG. 3. Calculated oscillatory hologram writing characteristic with decreasing amplitude and increasing period of the diffraction efficiency oscillations. Hologram thickness is 2.00 mm, $a = 10^{-11}$ $(V/m)^{-2}\,sec^{-1}$, $\phi_n = 90°$, $\alpha_0 = 0$, and other parameters as given in Sec. IV.

dent since the physical mechanism(s) (such as photochemical effects, drift of charge carriers, diffusion of charge carriers, etc.) that produce the sensitivity may be self-limiting in some materials. Therefore, saturation at low or high efficiency may be brought about by a vanishing sensitivity. At the turning point toward saturation, $|d\eta/dt|$ is strongly affected by $|da/dt|$. Thus, depending on the material and the experimental situation, gradual[22,24–28,30,31] or abrupt[23,29] turning points are observed in $\eta(t)$. Figure 2 demonstrates that an approximately saturating behavior may be predicted by the dynamic equations even with a constant refractive-index exposure sensitivity (Fig. 2 is similar to Fig. 6 in Ref. 15). Calculated oscillatory behavior is shown in Fig. 3.

Figure 3 exhibits behavior similar to that experimentally observed by the authors in lithium niobate and shown in Fig. 4. Note the decreasing amplitude and increasing period of the diffraction efficiency oscillations with exposure in both of these figures. Figure 3 also bears qualitative resemblance to Fig. 6 in Ref. 27 and to Fig. 2 in Ref. 28. Figure 5 illustrates large increasing diffraction efficiency oscillations with minima near 0%. This behavior is like that depicted in Fig. 5 of Ref. 2 for a 1.8-mm-thick photopolymer hologram grating.

The exceptional cases for which writing starts with an apparently linear $\eta(t)$ characteristic[23,25,28,39] (rather than parabolic) may possibly be reconciled by the fact that the zero-slope initial portion of the $\eta(t)$ is sometimes of very brief duration (see, for example, Fig. 4 of this paper, Fig. 2 in Ref. 22, Fig. 5 in Ref. 27, Fig. 1 in Ref. 35, etc.) and thus the curve appears to be approximately linear when in fact it may not be.

C. Reading

The application of a reading beam to a thick hologram may continually change its characteristics. Experimentally, the most commonly observed result seems to be exponentiallike decay of the diffraction efficiency.[14,22–24,27,28,30,32–34,36,37,40,41] Oscillatory diffraction efficiency readout behavior has also been reported. In rhodium-doped $LiNbO_3$, for example, vivid oscillations have been observed during readout.[28] An iron-doped sample of $LiNbO_3$ has shown an initial rise and a subsequent decay of diffraction efficiency upon readout.[33] Oscillatory behavior at low efficiency following an exponentiallike decay has also been noted.[33] Self-enhancement (an increase of diffraction efficiency upon reading) of Fe-doped $LiNbO_3$ holograms has been observed.[42] In this case, erasure and enhancement were produced depending on which of the original writing beams was used for readout. Behavior such as this has been theoretically predicted by Staebler and Amodei.[14] We present here further experimental results for volume holograms that show this type and other effects upon

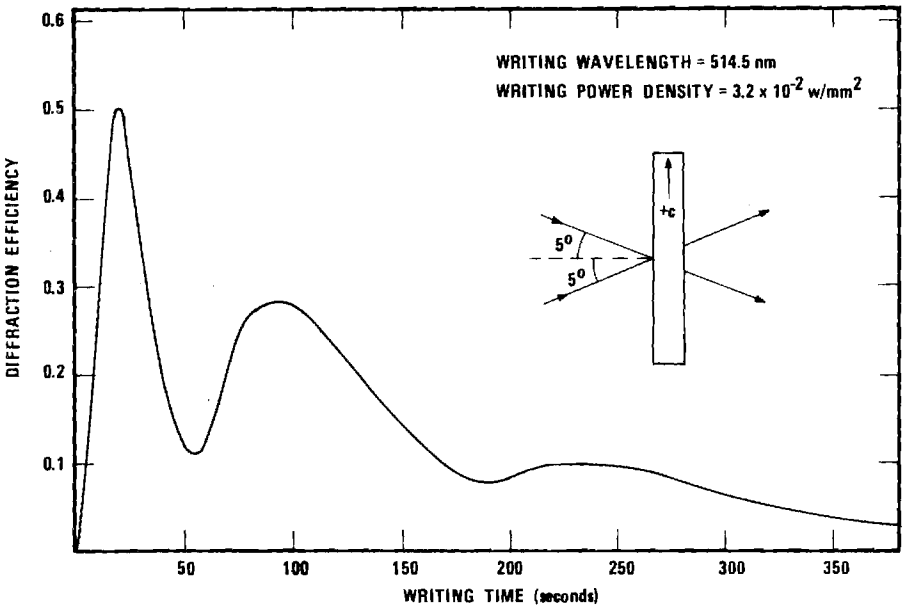

FIG. 4. Experimental oscillatory hologram writing characteristic for a 1.66-mm-thick iron-doped lithium niobate crystal. Writing beam polarizations are in the plane of incidence and the experimental configuration is as shown in the figure inset.

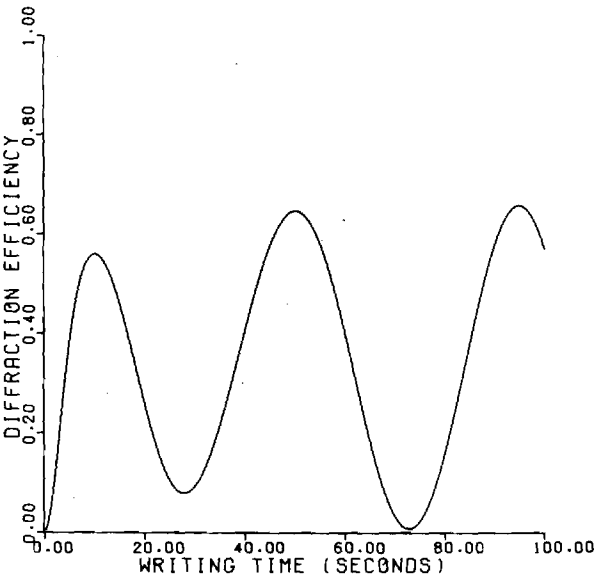

FIG. 5. Calculated oscillatory hologram writing characteristic with diffraction efficiency minima near 0%. Hologram thickness is 2.00 mm, $a = 10^{-11}$ $(V/m)^{-2}$ sec^{-1}, $\phi_n = 60°$, $\alpha_0 = 10^2$ m^{-1}, and other parameters as given in Sec. IV.

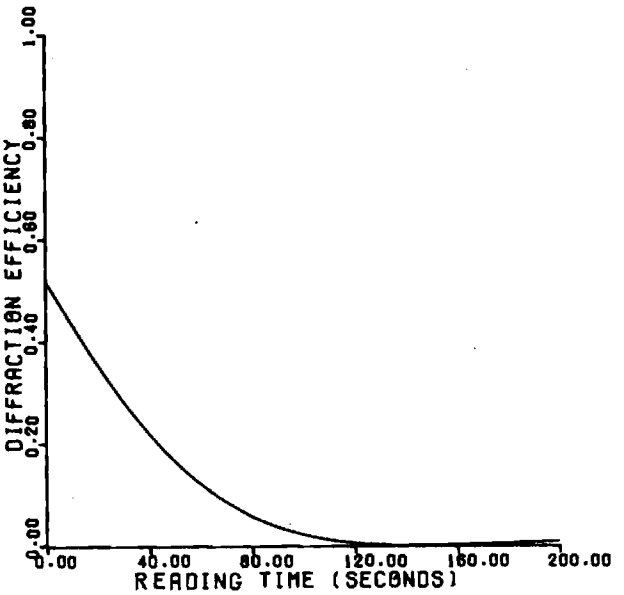

FIG. 6. Calculated exponentiallike reading characteristic. Note slight rise in efficiency at a reading time of 200 sec. Hologram thickness is 2.00 mm, $a = 10^{-12}$ $(V/m)^{-2}$ sec^{-1}, $\phi_n = 90°$, $\alpha_0 = 0$, readout with R beam, and other parameters as given in Sec. IV. The original hologram was recorded using these same parameters and an exposure time of 40 sec.

changing the reading beam from the R beam to the S beam (see Fig. 1).

The various types of behavior discussed above are all predicted by the dynamic theory. In Fig. 6, for example, a calculated exponentiallike decay of the hologram efficiency is shown. Note that, eventually, the efficiency rises again (as experimentally reported in Ref. 33 and in Fig. 4 of Ref. 41). Figure 7 depicts the experimentally recorded decay of the efficiency of a hologram written in a 1.66-mm-thick iron-doped crystal of $LiNbO_3$ for the beam configuration indicated in the inset of Fig. 7. Note the slight oscillations at low efficiency. Figures 8 and 9 illustrate the calculated effect of switching the reading beam to the symmetrical angular location. In Fig. 8, an initial decrease in diffraction efficiency is predicted, whereas in Fig. 9 an initial increase is predicted (like experimental data in Fig. 6 of Ref. 33, in Fig. 2 of Ref. 42, and in Fig. 12 of this paper). Figure 8 also clearly predicts oscillations at low efficiency such as have been experimentally observed. Figure 10 shows the behavior of efficiency oscillations followed by monotonic decay as calculated by the dynamic theory. This is qualitatively like the experimental readout behavior observed in rhodium-doped $LiNbO_3$ by Ishida *et al.*[28] Figure 11 illustrates calculated diffraction efficiency

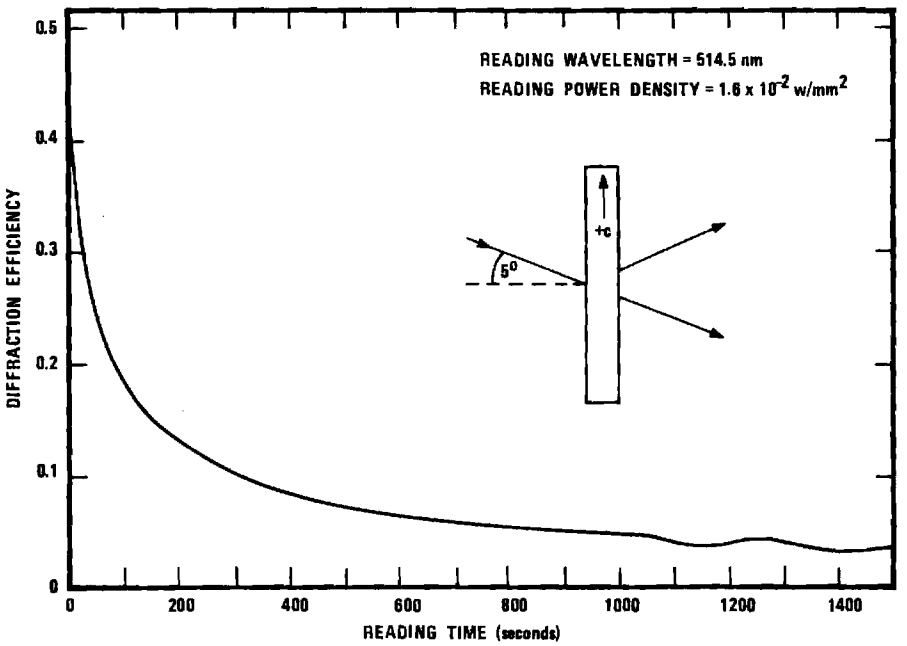

FIG. 7. Experimental exponentiallike reading characteristic for a 1.66-mm-thick iron-doped lithium niobate crystal. Small amplitude diffraction efficiency oscillations are present at low efficiencies. Reading beam polarization is in the plane of incidence and the experimental configuration is as shown in the figure inset.

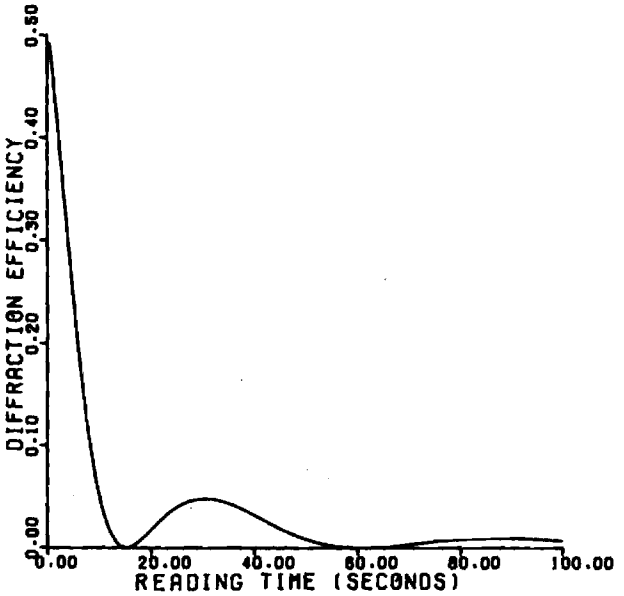

FIG. 8. Calculated reading characteristic showing diffraction efficiency oscillations at low efficiencies. Hologram thickness is 2.00 mm, $a = 10^{-11}$ $(V/m)^{-2}$ sec^{-1}, $\phi_n = 90°$, $\alpha_0 = 10^2$ m^{-1}, readout with R beam, and other parameters as given in Sec. IV. The original hologram was recorded using these same parameters and an exposure time of 10 sec.

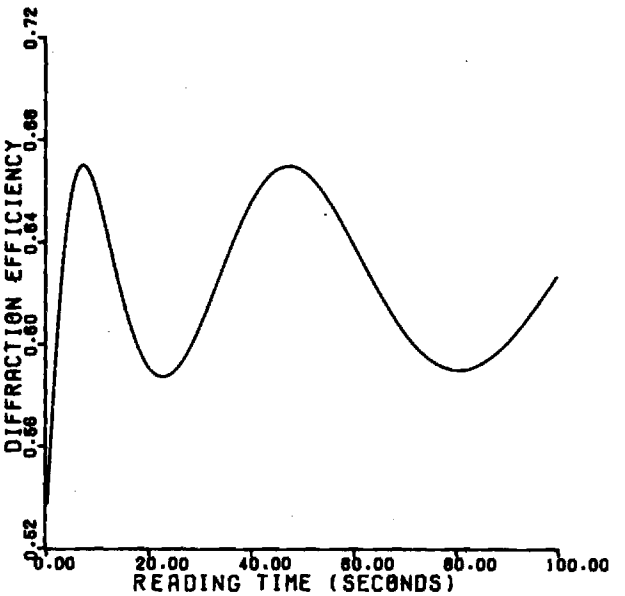

FIG. 9. Calculated enhancement and oscillatory reading characteristic resulting from S-beam readout as opposed to normal R-beam readout. All other conditions and parameters are identical to those of Fig. 8.

oscillations that both decrease and increase as a function of readout exposure. In Fig. 12, we show experimentally measured oscillatory reading behavior for the same hologram grating used in Fig. 7 except that reading is done with the beam at the symmetric recording angle (reading with the S beam instead of the R beam in the notation of Fig. 1). Large variations in both the amplitude and the period of the efficiency oscillations are observed. This behavior is qualitatively similar to the predicted readout diffraction efficiency of Fig. 11.

D. Angular selectivity

Angular selectivity refers to the variation of diffraction efficiency as a function of angle of incidence of the reading wave. In experiments measuring this property of thick hologram gratings, a low power reading beam or a reading beam of a wavelength at which the material is insensitive is generally used so as not to affect the hologram by the process of measurement.

Experimental angular selectivity results are somewhat less plentiful than the other terminally measured

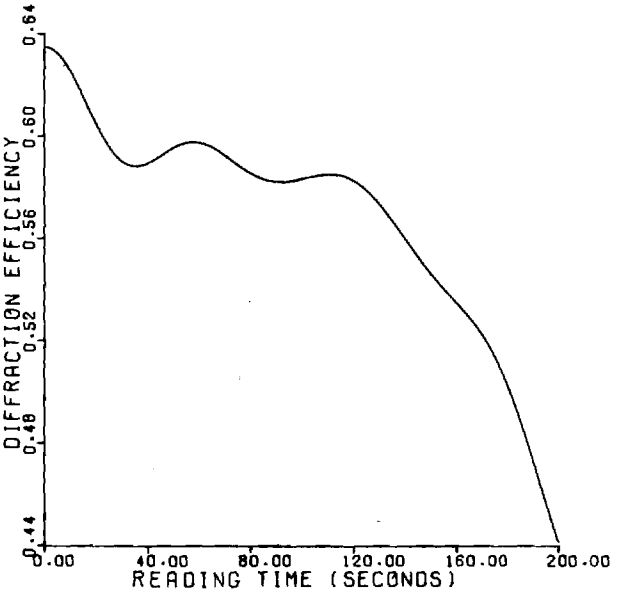

FIG. 10. Calculated reading characteristic showing diffraction efficiency oscillations followed by rapid decay. Hologram thickness is 2.00 mm, $a = 10^{-11}$ $(V/m)^{-2}$ sec^{-1}, $\phi_n = 0°$, $\alpha_0 = 0$, readout with R beam, and other parameters as given in Sec. IV. The original hologram was recorded using these same parameters and an exposure time of 35 sec.

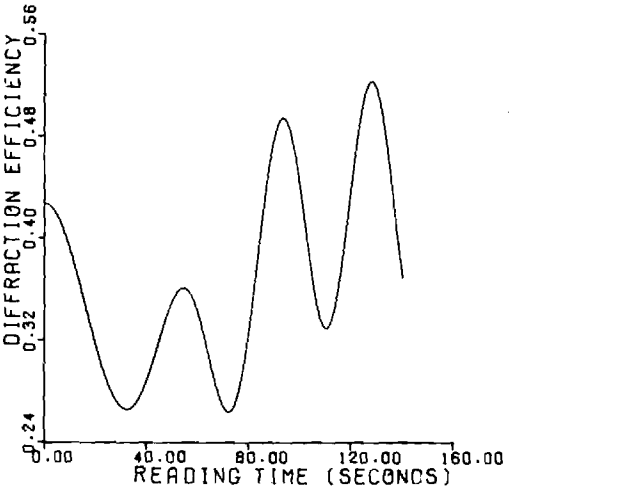

FIG. 11. Calculated oscillatory reading characteristic showing large variations in the amplitude and period of the diffraction efficiency oscillations. Hologram thickness is 2.00 mm, $a = 10^{-11}$ $(V/m)^{-2}$ sec^{-1}, $\phi_n = 0°$, $\alpha_0 = 0$, readout with R beam, and other parameters as given in Sec. IV. The original hologram was recorded using these same parameters and an exposure time of 10 sec.

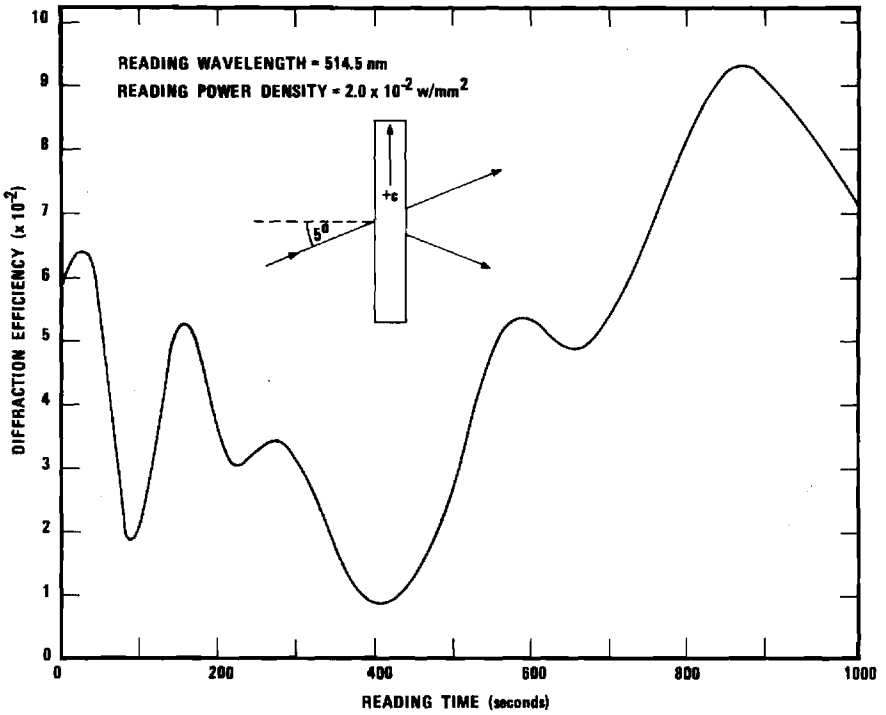

FIG. 12. Experimental oscillatory reading characteristic for a 1.66-mm-thick iron-doped lithium niobate crystal. A wide variation in the amplitude and period of the diffraction efficiency oscillations is apparent. Reading beam polarization is in the plane of incidence and the experimental configuration is as shown in the figure inset.

characteristics of thick holograms. Some of the existing experimental results exhibit a series of nonzero minima in place of the nulls[43–47] predicted by static hologram theories. Some experimental data show no minima in the angular selectivity.[43,48] It is now well established[20,21,43] that nonuniformity of the grating with material thickness produces nonzero diffraction minima or the complete disappearance of the minima in the angular selectivity.

The dynamic theory straightforwardly predicts the various types of angular selectivity behavior of volume holograms. Here, grating nonuniformity arises if $\phi_n \neq 0$, or $\alpha_0 \neq 0$, or if both ϕ_n and α_0 are nonzero. Nonuniformity, and the corresponding disappearance of angular selectivity minima for low-loss materials ($\alpha_0 \cong 0$), is explained here by the dynamic theory but cannot be explained by the static theories. In Fig. 13, a logarithmic plot of experimental data is presented for a hologram written in a 1.66-mm-thick 0.05-mole% Fe-doped crystal of $LiNbO_3$ and compared to the solution of Eqs. (3) and (4) for the same conditions. Due to the short writing time and the low efficiency ($\cong 1\%$), the grating is still quite uniform through the thickness of the material (z direction) and thus the grating exhibits well-defined nulls in the diffraction efficiency for a series of reading angles. Theory and experiment both show these nulls. Figure 14 indicates the vanishing of the angular selectivity nulls as the grating develops and begins to show nonuniformity in the amplitude of the refractive index modulation with z (see inset in Fig. 14). Figure 15 shows the angular selectivity and the index profile for the hologram grating after further exposure. Note that $\alpha_0 = 0$. Figure 15 illustrates that the absolute maximum diffraction intensity peak now occurs off the Bragg angle. The pattern is symmetric with respect to the Bragg angle and thus a second peak occurs for an angle of incidence on the other side of the Bragg angle.

V. DISCUSSION

The prediction of a very wide variety of results in volume holography is possible with the dynamic theory. Writing and reading characteristic curves (usually presented as η vs t) may have an infinitude of possible magnitudes and shapes. The calculated curves presented in this paper are typical results taken from a much larger number of cases that have been analyzed by the authors. Many rapidly varying experimental writing and reading results (such as the data shown in Fig. 12) have previously informally been attributed to "experimental problems". It is now apparent that these types of oscillatory results are "normal" and are to be expected.

The dynamic theory is an important aid in identifying the "significant" parameters in volume holographic recording and readout. Relatively few parameters are needed in the dynamic theory. The role of each of these parameters can be determined in a given situation. This indicates the possibility of using the dynamic theory (1) as an aid in synthesis and (2) as a diagnostic tool.

As an aid in synthesis, the dynamic theory serves as an indicator of the parameter values that are needed to produce a particular desired situation (e.g., uniformity of induced change through the thickness of a hologram, a certain type of angular selectivity, an enhancing readout, a rapidly erasing readout, etc.). The dynamic theory parameters in some materials, indeed, may be controlled in a fairly direct manner. For example, in iron-doped lithium niobate, α_0 and a may be dramatically changed by heat treating the material in various environments.[32,33] Microscopically, this has been shown to control the relative Fe^{2+} and Fe^{3+} concentrations in iron-doped lithium niobate.[32,33] In addition, the phase difference between the light and the refractive-index

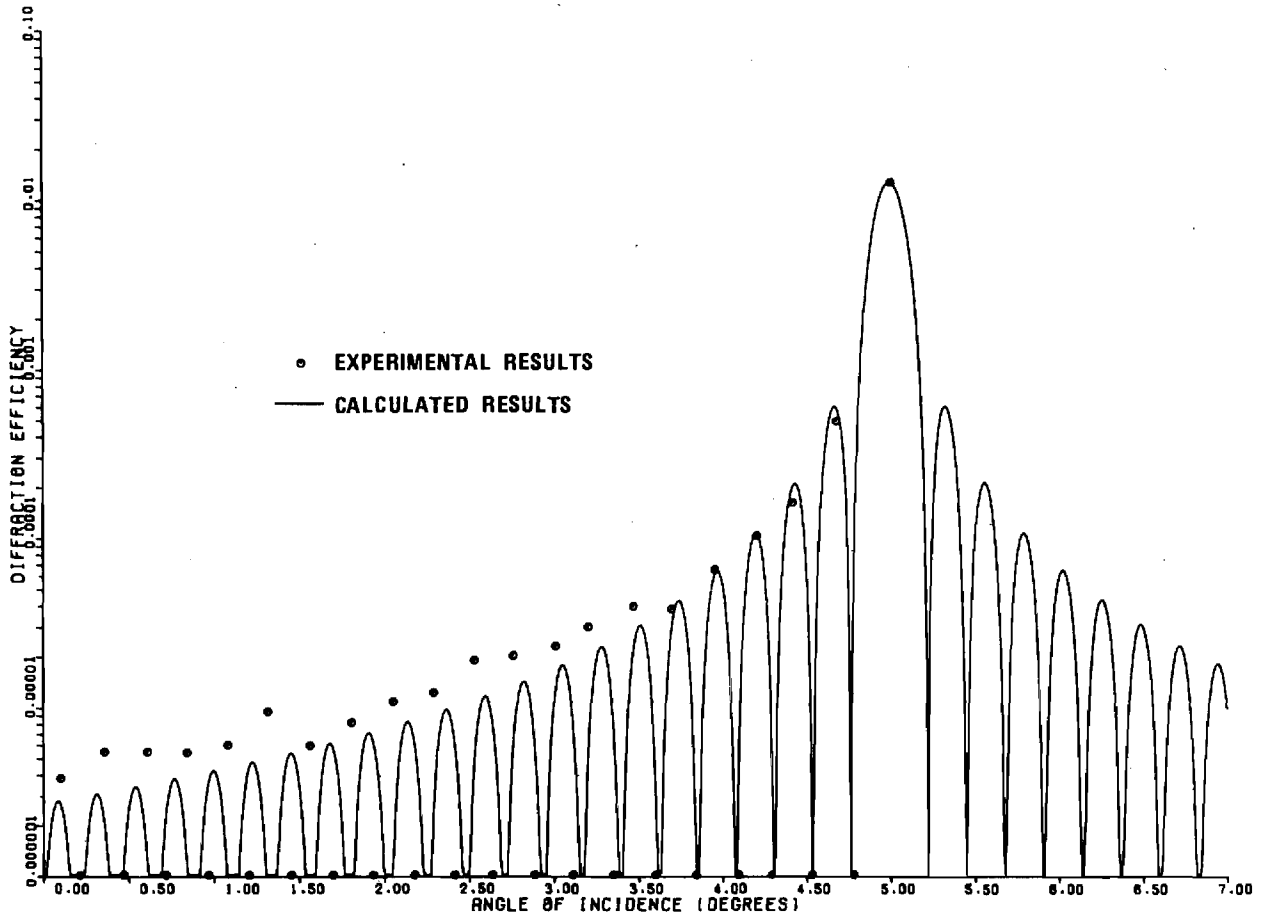

FIG. 13. Experimental and calculated angular selectivity exhibiting zero diffraction efficiency at minima. The hologram is a 1.66-mm-thick iron-doped lithium niobate crystal. Experimentally, hologram was written with a wavelength of 514.5 nm, a total power density of 3.5 mw/mm^2, external angles of incidence of $\pm$ 5.00°, a writing time of 5 sec, polarization in the plane of incidence, and the configuration shown in the inset of Fig. 4. Experimentally, the angular selectivity was measured with a low power beam of the same wavelength. The calculated curve is for a hologram of thickness of 1.66 mm, written with $R_0 = 571$ V/m, $S_0 = 518$ V/m, for 5 sec with $a = 3.8 \times 10^{-12}$ (V/m)$^{-2}$ sec^{-1}, $\phi_n = 0°$, and $\alpha_0 = 0$, these parameters being estimated from the experimental conditions.

grating, ϕ_n, approaches 0° when drift of the photoexcited electrons dominates[14] (which may be induced by externally applying an electric field). The phase difference approaches 90° when diffusion of the electrons dominates[14] (which may be induced by using a small fundamental grating spacing).

As a diagnostic tool, the dynamic theory, when coupled with experiment, is capable of determining certain material and hologram characteristics. By experimentally holding constant some of the dynamic theory parameters, other parameters and properties may be found. For example, the variations with grating thickness of the refractive index may be determined knowing the conditions of recording. This would allow the direct determination of the index profile (in the z direction) as opposed to assuming a uniform grating or an exponential variation with thickness (both of which may be totally incorrect). As another example, the variation with exposure of the refractive-index exposure sensitivity, a, may be measured. By holding the other dynamic theory parameters constant and measuring the hologram writing characteristic, the time dependence of the index exposure sensitivity may be determined.

Chronologically, in the literature, the earlier thick recording materials tended to show a saturating-type writing characteristic indicating a rapidly decreasing value of a. More recently, higher-sensitivity materials have tended to show an oscillatory writing characteristic indicating a larger dynamic range for these materials (and thus the dynamic theory is valid in these cases with essentially a constant value of a).

VI. CONCLUSION

A large number of different types of recording and reading behaviors have been reported for thick (volume) holograms in a wide variety of recording materials. Writing, reading, and angular selectivity experimental data from approximately 25 published articles are cited in this paper as being representative of the known types of behavior. The dynamic theory of thick hologram recording and reading qualitatively predicts all of these various types of experimental behavior. Thus, the dynamic theory is potentially very powerful (1) in determining the material and recording parameters needed to produce a certain desired hologram characteristic

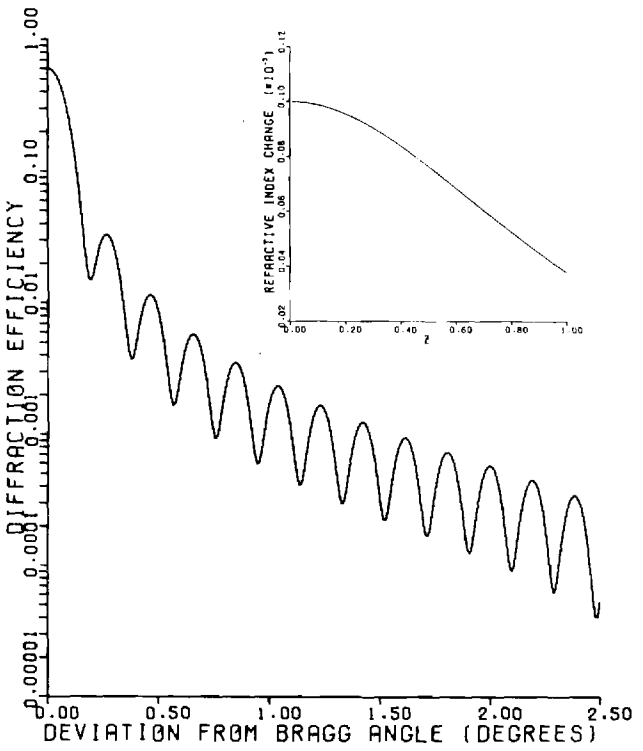

FIG. 14. Calculated angular selectivity exhibiting nonzero diffraction efficiency at minima. Nonzero minima are characteristic of phase holographic gratings having a variation in index of refraction through the thickness of the material. The refractive-index profile is shown in the inset. Hologram thickness is 2.00 mm, $a = 10^{-11}$ $(V/m)^{-2}$ sec^{-1}, $\phi_n = 90°$, $\alpha_0 = 0$, and writing time is 5 sec.

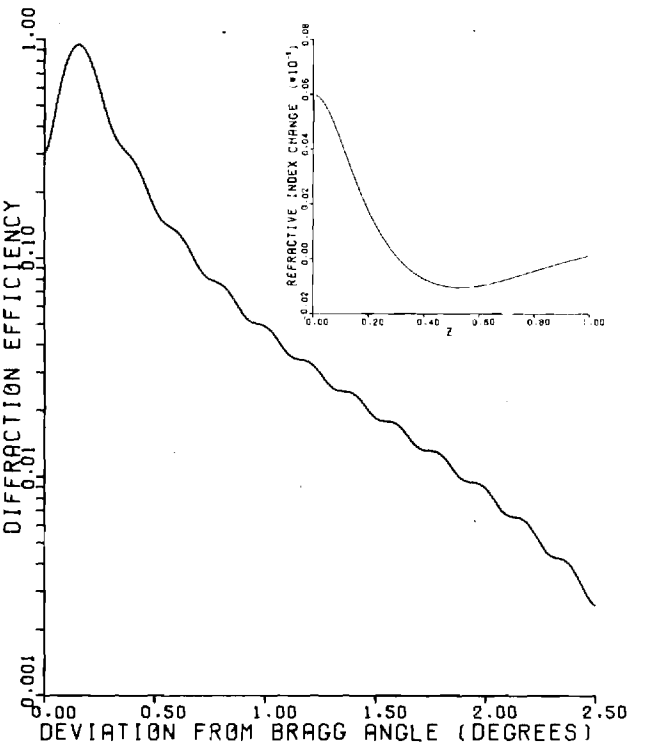

FIG. 15. Calculated angular selectivity showing the disappearance of diffraction efficiency minima. The same conditions as Fig. 14 prevail but with a longer writing time of 30 sec. The increased nonuniformity of the grating profile is shown in the inset.

and (2) as a diagnostic tool to analyze the parameters of thick photosensitive recording materials.

Note added in proof. An oscillatory diffraction efficiency upon readout has also been shown theoretically and experimentally to be possible due to changes in the multiple internal reflections as a result of crystal thermal expansion caused by the absorption of laser light. These results are reported in the work by W. D. Cornish and L. Young, J. Appl. Phys. **46**, 1252 (1975). In our experimental case (Figs. 4, 7, 12, and 13), we have found by the reflectance test given in the above reference that our crystals do not satisfy the flatness-and-parallelism requirements necessary for such effects to occur. Laser-induced thermal expansion, therefore, does not significantly affect our experimental results.

ACKNOWLEDGMENTS

The authors would like to thank S. F. Su for his help with the numerical analysis in this paper and W. R. Callen for his help with the experimental measurements.

*Work supported by the National Science Foundation and by the National Aeronautics and Space Administration.

[1]H. Kogelnik, Bell Syst. Tech. J. **48**, 2909 (1969).
[2]M. R. B. Forshaw, Opt. Laser Technol. **6**, 28 (1974).
[3]B. H. Crawford, J. Sci. Instrum. **31**, 333 (1954).
[4]J. N. Latta and R. C. Fairchild, J. Opt. Soc. Am. **63**, 487 (1973).
[5]R. Shubert and J. H. Harris, J. Opt. Soc. Am. **61**, 154 (1971).
[6]H. Kogelnik and C. V. Shank, Appl. Phys. Lett. **18**, 152 (1971).
[7]H. Kogelnik and T. P. Sosnowski, Bell Syst. Tech. J. 49, 1602 (1970).
[8]M. L. Dakss, L. Kuhn, P. F. Heidrich, and B. A. Scott, Appl. Phys. Lett. **16**, 523 (1970).
[9]J. M. Hammer, Appl. Phys. Lett. **18**, 147 (1971).
[10]P. J. Van Heerden, Appl. Opt. **2**, 393 (1963).
[11]K. S. Pennington and L. H. Lin, Appl. Phys. Lett. **7**, 56 (1965).
[12]G. W. Stroke and A. E. Labeyrie, Phys. Lett. **20**, 368 (1966).
[13]C. B. Burckhardt, J. Opt. Soc. Am. **56**, 1502 (1966).
[14]D. L. Staebler and J. J. Amodei, J. Appl. Phys. **43**, 1042 (1972).
[15]Y. Ninomiya, J. Opt. Soc. Am. **63**, 1124 (1973).
[16]See, for example, T. K. Gaylord, Opt. Spectra **8**, 29 (1974).
[17]P. Phariseau, Proc. Indian Acad. Sci. A **44**, 165 (1956).
[18]S. F. Su and T. K. Gaylord, J. Opt. Soc. Am. **65**, 59 (1975).
[19]D. Kermisch, J. Opt. Soc. Am. **61**, 1202 (1971).
[20]D. Kermisch, J. Opt. Soc. Am. **59**, 1409 (1969).
[21]N. Uchida, J. Opt. Soc. Am. **63**, 280 (1972).
[22]T. K. Gaylord, T. A. Rabson, and F. K. Tittel, Appl. Phys. Lett. **20**, 47 (1972).
[23]F. Micheron and G. Bismuth, Digest of Technical Papers, 1972 IEEE International Solid-State Circuits Conference, p. 104 (unpublished).
[24]W. Phillips, J. J. Amodei, and D. L. Staebler, RCA Rev. **33**, 95 (1972).

[25]L.H. Lin, Proc. IEEE **57**, 252 (1969).
[26]F.S. Chen, J.T. LaMacchia, and D.B. Fraser, Appl. Phys. Lett. **13**, 223 (1968).
[27]J.J. Amodei, W. Phillips, and D.L. Staebler, Appl. Opt. **11**, 390 (1972).
[28]A. Ishida, O. Mikami, S. Miyazawa, and M. Sumi. Appl. Phys. Lett. **21**, 192 (1972).
[29]R.W. Damon, D.H. McMahon, and J.B. Thaxter, Electro-Opt. Syst. Des. **2**, 68 (1970).
[30]F. Micheron and G. Bismuth, Appl. Phys. Lett. **23**, 71 (1973).
[31]T.A. Shankoff, Appl. Opt. **7**, 2101 (1968).
[32]W. Phillips and D.L. Staebler, J. Electron. Mater. **3**, 601 (1974).
[33]D.L. Staebler and W. Phillips, Appl. Opt. **13**, 788 (1974).
[34]J.P. Huignard, J.P. Herriau, and F. Micheron, Appl. Phys. Lett. **26**, 256 (1975).
[35]D.L. Staebler, W.J. Burke, W. Phillips, and J.J. Amodei, Appl. Phys. Lett. **26**, 182 (1975).
[36]J.J. Amodei, D.L. Staebler, and A.W. Stephens, Appl. Phys. Lett. **18**, 507 (1971).
[37]F. Micheron and G. Bismuth, Digest of Technical Papers, Optical Storage of Digital Data, MB3-1, 1973 (unpublished).
[38]T.K. Gaylord, T.A. Rabson, F.K. Tittel, and C.R. Quick, Appl. Opt. **12**, 414 (1973).
[39]R.L. Townsend and J.T. LaMacchia, J. Appl. Phys. **41**, 5188 (1970).
[40]J.J. Amodei and D.L. Staebler, Appl. Phys. Lett. **18**, 540 (1971).
[41]D.L. Staebler and J.J. Amodei, Ferroelectrics **3**, 107 (1972).
[42]T.K. Gaylord, T.A. Rabson, F.K. Tittel, and C.R. Quick, J. Appl. Phys. **44**, 896 (1973).
[43]E.N. Leith, A. Kozma, J. Upatnieks, J. Marks, and N. Massey, Appl. Opt. **5**, 1303 (1966).
[44]K. Biedermann, S.I. Ragnarsson, and P. Komlos, Opt. Commun. **6**, 205 (1972).
[45]V.V. Aristov and V.Sh. Shekhtman, Sov. Phys. Usp. **14**, 263 (1971).
[46]R.G. Zech, Ph.D. thesis (University of Michigan, 1974) (unpublished).
[47]D.R. Bosomworth and H.J. Gerritsen, Appl. Opt. **7**, 95 (1968).
[48]T.K. Gaylord and F.K. Tittel, J. Appl. Phys. **44**, 4771 (1973).

Reprinted from **APPLIED OPTICS**, Vol. 15, page 3021, December 1976

Dynamically produced refractive-index variations with thickness of volume holograms in electrooptic crystals

R. Magnusson and T. K. Gaylord

Dynamic theory of volume holography is used to calculate the variations in the thickness direction of the hologram-constituting refractive-index modulation and the externally observable effects of these variations in electrooptic materials. It is shown that thick holographic gratings may exhibit significant amplitude and grating phase variations with thickness including amplitude sign reversal. These nonuniformities strongly affect holographic grating recording and readout characteristics such as maximum possible diffraction efficiency and angular selectivity. Thus a variety of grating applications will be affected by these nonuniformities.

Introduction

Due to a variety of important applications, volume holographic recording has been the subject of much research. The initial analyses of volume (thick) holograms[1,2] were static in nature as the dynamic influence of the grating formation on the recording fields was neglected. In these papers, the holographic gratings analyzed were assumed to be uniform through the thickness of the material.

A more general approach, allowing for the effects of dynamic grating formation, has been presented by Ninomiya.[3] Such theory has been shown to account for the various types of experimental behavior observed in the recording, readout, and angular selectivity characteristics of thick ferroelectric holograms.[4] In dynamic theory, the exposure $\mathcal{E}$, which is the time integral of the local irradiance, is the fundamental parameter through which the dynamic feedback between the grating being formed and the fields propagating in that structure is introduced. Thus, the time–space evolution (history) continually modifies the grating and its associated externally observable characteristics. Because of the generality of the dynamic theory, no arbitrary conditions on the variations with thickness of the hologram constituting material changes are imposed. It is the purpose of this paper to discuss the thickness variations of the refractive-index modulation in electrooptic volume phase hologram gratings as derived from the dynamic theory. The present work considers only optically induced refractive-index changes (photorefractive effect). Similar effects in photochromic materials have been considered by others.[5,6]

It is shown in this paper that dynamically induced grating nonuniformities significantly influence volume hologram recording and readout behavior. On recording, the drop in the maximum attainable diffraction efficiency is linked to increasing grating nonuniformities. On readout, the sidelobe structure and symmetry of the angular selectivity characteristics are shown to be associated with the nonuniformities. As a result, these effects are important, and must generally be considered in volume holography applications. Considered separately, the nonuniformities are interesting and potentially useful in some applications.

Theory

In the present context, it is assumed that the change in the refractive index n is related to the exposure $\mathcal{E}$ by

$$dn/d\mathcal{E} = a = \text{constant}, \tag{1}$$

where a is the exposure sensitivity of the refractive index,

$$\mathcal{E} = \int_0^T \bar{E}\cdot\bar{E}^* dt,$$

where T is the exposure time, $\bar{E}(\bar{r},t) = R(z,t)\hat{r}\exp(-j\bar{\rho}\cdot\bar{r}) + S(z,t)\hat{s}\exp(-j\bar{\sigma}\cdot\bar{r})$ is the total rms complex electric field in the material, $\bar{E}^*$ is its complex conjugate, $R(z,t)$ and $S(z,t)$ are the complex amplitudes of two recording plane waves with wave vectors $\bar{\rho}$ and $\bar{\sigma}$ and polarization vectors $\hat{r}$ and $\hat{s}$, respectively, all lying in the plane of incidence (E-mode polarization), $\bar{r} = (x,y,z)$, where z is the direction through the thickness of the plane parallel material slab of thickness d, and x is in the direction of the grating vector $(\bar{\rho} - \bar{\sigma})$. The angle

The authors are with Georgia Institute of Technology, School of Electrical Engineering, Atlanta, Georgia 30332.

Received 2 August 1976.

between the (symmetrical) wave vectors $\bar{\rho}$ and $\bar{\sigma}$ is 2θ. The assumption represented by Eq. (1) merits discussion. It has been shown previously that using this assumption in the dynamic theory yields results that qualitatively describe a wide variety of experimental behavior.[4] Furthermore, the optically induced space-charge field that modulates the refractive index to form hologram gratings in electrooptic materials has an exponential saturation characteristic with a time constant that is approximately τ_r, the illuminated dielectric relaxation time of the material.[7,8] The exposure sensitivity decays with the same time constant. In a typical representative case $\tau_r \simeq 660$ sec for an iron-doped crystal of lithium niobate as determined by holography experiments.[9] Therefore, the exposure sensitivity may be assumed to vary slowly over the exposure range used here and can be approximated by a constant.

It can be shown that the spatially varying holographic refractive-index modulation may be represented as

$$n_1(x,z,T) = 2a \cos 2\theta (M^2 + N^2)^{1/2} \times \cos\{(\bar{\sigma} - \bar{\rho}) \cdot \bar{r} + \phi_n + \cos^{-1}[M/(M^2 + N^2)^{1/2}]\}, \quad (2)$$

where

$$M \equiv M(z,T) \equiv \int_0^T \mathrm{Re}\{RS^*\}dt,$$

$$N \equiv N(z,T) \equiv \int_0^T \mathrm{Im}\{RS^*\}dt,$$

and ϕ_n is the spatial phase difference ($0° \leq \phi_n \leq 90°$) between the grating-forming light intensity pattern and the resulting refractive-index pattern. Thus, if the wave amplitudes $R(z,t)$ and $S(z,t)$ are known, the index modulation can be calculated by Eq. (2). It is noted that the grating is sinusoidal in x, but with amplitude and phase dependent on the exposure time T and the thickness coordinate z. The amplitude of the index modulation along a peak in the pattern n_{1p} is consequently

$$n_{1p(z,T)} = 2a \cos 2\theta (M^2 + N^2)^{1/2}. \quad (3)$$

Likewise, the quantity $\cos^{-1}[M/(M^2 + N^2)^{1/2}]$ is a measure of grating bending[10-12]; that is, the deviation of a grating peak at an arbitrary value of z from its position at $z = 0$. It is seen that grating bending is a direct result of a possible z-dependent phase difference between the two waves in the medium (consider $N = 0$).

Results

The wave amplitudes $R(z,t)$ and $S(z,t)$ are calculated from the dynamic coupled-wave equations given in Ref. 4 with the boundary conditions $R(0,t) = S(0,t) = 1000$ V/m. This produces an incident beam intensity ratio [$\xi = S^2(0,t)/R^2(0,t)$] of unity. The wavelength is $\lambda = 0.5145$ μm, the index of refraction is $n_o = 2.243$ ($LiNbO_3$ crystal), and the absorption coefficient is $\alpha_o = 100$ m^{-1}. The wave amplitudes are used to calculate grating variations in z and t as indicated above.

Figure 1 shows the peak amplitudes [from Eq. (3)] of holographic gratings (recorded with typical experimental parameters) as functions of z for different spatial phase shifts ϕ_n. These grating profiles are calculated at the times (T) when the corresponding maximum diffraction efficiencies are reached on the recording characteristics as indicated in the figure inset. The gratings are found to become increasingly nonuniform with increasing values of ϕ_n and T. The value of ϕ_n in ferroelectrics is determined by the relative contributions of electronic diffusion and drift during recording.[10] For diffusion only $\phi_n = 90°$ and for pure drift $\phi_n = 0°$, which are valid if the carrier migration length is short compared to the grating period L. For longer migration lengths, the present analysis is still valid; only the physical interpretation needs to be modified.[13] The grating peak profiles shown in Fig. 1 exhibit nonuniformities typical of hologram gratings recorded to the maximum diffraction efficiency η_{max}, allowed by the material and its physical processes. The diffraction efficiency is maximum for $\phi_n = 0°$ if the incident beam intensity ratio is unity. In this case, $\eta_{max} = \exp(-2\alpha_o' d/\cos\theta')$, where α_o' is the absorption coefficient for the readout process[2,3] and θ' is the reading angle. For each $\phi_n \neq 0°$, the diffraction efficiency $\eta \leq \eta_{max}$, where the equal sign holds for a suitable ratio of the incident recording beam intensities.[14,15] This is, effectively, recording with $\xi = 1$ in addition to a simultaneous enhancing readout. If $\xi = 1$ and $\phi_n \neq 0°$, $\eta < \eta_{max}$.[14] Thus it is seen from Fig. 1 that the drop in the maximum diffraction efficiency corresponds to increased grating amplitude nonuniformity. For $\phi_n = 0°$, the monotonic drop with z is caused entirely by absorption ($\alpha_o \neq 0$). For $\phi_n = 90°$, the grating peak amplitude in Fig. 1 has dropped to zero at the output face of the crystal.

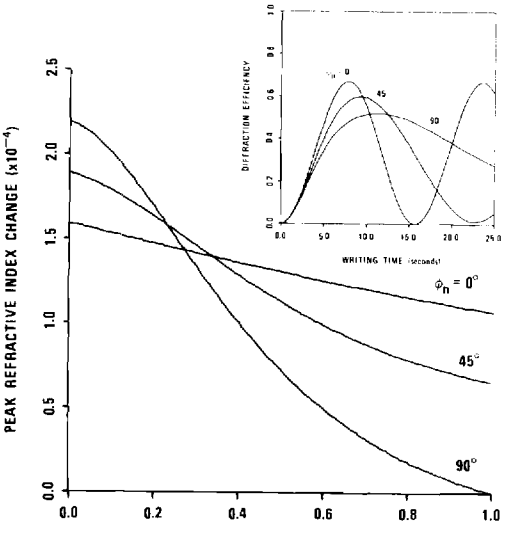

Fig. 1. Calculated refractive-index amplitude variations with normalized thickness along an amplitude peak in the holographic grating pattern. The hologram thickness is 2.00 mm, $a = 10^{-11}$ (V/m)$^{-2}$ sec^{-1}, $\alpha_o' = \alpha_o = 10^2$ m^{-1}, and $\theta = 2.23°$ (5.00° angle of incidence external to a crystal of $n_o = 2.243$). The curves are calculated at the times corresponding to the first maxima of the recording characteristics shown in the inset.

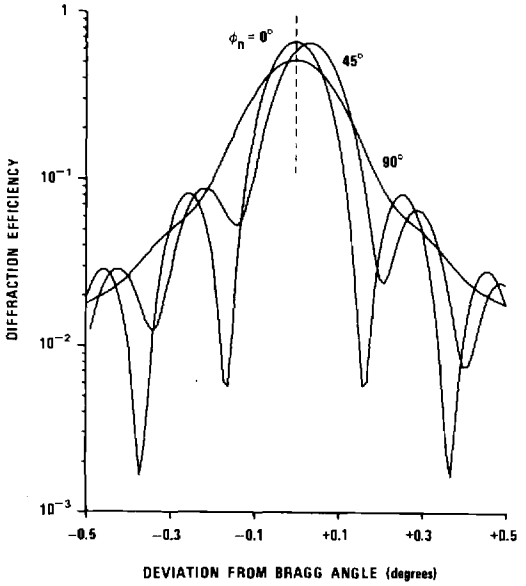

Fig. 2. Calculated angular selectivity characteristics for the gratings of Fig. 1. Vertical dashed line indicates position of Bragg angle.

Figure 2 shows the angular selectivity characteristics of the gratings of Fig. 1. The deviation from the Bragg angle is defined here as $\Delta\theta' = \theta' - \theta$. Increasing grating amplitude nonuniformity is seen to result in less accentuated minima in the angular selectivity pattern. This is a general result that has been obtained before for the case of exponentially attenuated gratings[16,17] such as those shaped by absorption only (i.e, $\phi_n = 0°$, $\alpha_0 \neq 0$). Note that the pattern is symmetric relative to the Bragg angle for the limiting cases $\phi_n = 0°$ and 90°. For intermediate values of ϕ_n, asymmetry in the angular selectivity occurs. For $\phi_n = 45°$ and the conditions presently used, the maximum diffraction efficiency, for example, occurs at $\Delta\theta' = 0.03°$ and is higher than that exactly on the Bragg angle by about 6%.

Figure 3 shows the gratings of Fig. 1 with their spatial phase variations (bending) at a later stage in their evolution (T = 25 sec; see the inset of Fig. 1). The nonuniformities have significantly increased. For ϕ_n = 90°, amplitude sign reversal is shown to occur, that is, the grating undergoes a 180° phase reversal for a range of the thickness coordinate. For $\phi_n = 45°$, the grating peak has shifted more than one-third of a period in x at the output plane. No phase shift takes place for $\phi_n = 0°$ for this case of $\xi = 1$. Grating bending thus occurs for $0° < \phi_n < 90°$.

Finally, Fig. 4 illustrates the angular selectivity characteristics associated with the gratings of Fig. 3. Only for $\phi_n = 0°$ does the maximum diffraction efficiency occur exactly on the Bragg angle. The pattern sidelobes become increasingly obliterated with increasing grating nonuniformity. The patterns are still symmetric for $\phi_n = 0°$ and 90° but not for other values of ϕ_n. Since these are the only values for which the grating does not bend, it is thus shown that the asymmetry of the angular selectivity pattern relative to the Bragg angle is associated with the bending of the grating. Asymmetric angular selectivity characteristics have been observed experimentally in electrooptic crystals.[14]

Conclusions

The nonuniformities discussed above can be of importance in applications employing holographic principles. For example, the angular selectivity, spectral

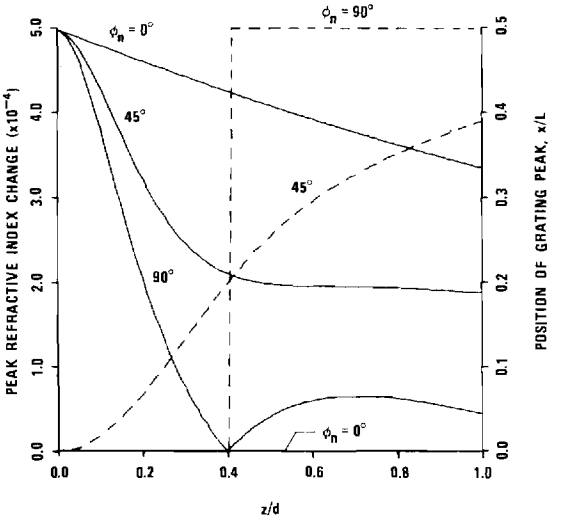

Fig. 3. Peak amplitudes of the refractive-index gratings (solid curves) as functions of distance through the grating after an exposure time T = 25 sec. Also shown are the positions of the grating peaks (dashed curves) as functions of thickness indicating the bending of the grating. All parameters are the same as in Fig. 1.

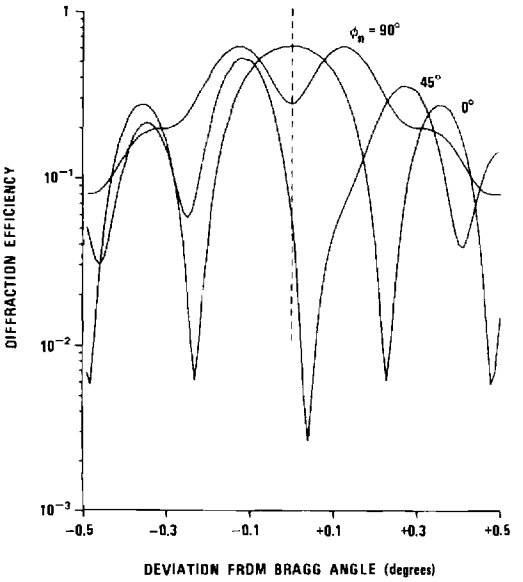

Fig. 4. Calculated angular selectivity characteristics for the gratings of Fig. 3. Vertical dashed line shows position of Bragg angle.

selectivity, and maximum obtainable diffraction efficiency are influenced by these nonuniformities. Thus, the calculations can be used to determine the crosstalk characteristics of angularly stacked holograms such as would be used for storing images, storing digital data, or in color holography. For a single angular selectivity maximum, it is desirable to have ϕ_n approach 90°. However, the reduction in sidelobe definition is seen to correspond to decreased diffraction efficiency and a larger angular width of the central lobe.

The theory is also useful in predicting the optimum experimental conditions for synthesizing a desired grating profile. For example, to obtain approximately uniform gratings (assuming small α_o) and high diffraction efficiency, it is desirable that ϕ_n approach 0°. This may be accomplished in electrooptic crystals by applying an electric field so as to increase electronic drift. Furthermore, the theory predicts that by allowing some inequality in the incident writing beam intensities, the otherwise unavoidable loss-induced grating amplitude drop can be compensated, at least partially, and more nearly uniform gratings obtained.[14] It is possible that this ability to tailor the grating profile may be useful in diffraction grating fabrication and in integrated optical grating components, such as used for distributed feedback, reflecting, filtering, and coupling.

In summary, it has been shown that thick holographic gratings can be significantly nonuniform with thickness and that amplitude variations, grating bending, and grating phase reversal may occur. The asymmetry of the angular selectivity characteristics around the Bragg angle is found to be associated with grating bending, while the obliteration of the angular selectivity minima is associated with grating amplitude variations with thickness.[18] Furthermore, the maximum obtainable diffraction efficiency on recording is limited by the nonuniformities. Thus, these effects appreciably influence the hologram recording and readout characteristics. In turn, these effects impact practical applications of holographic recording in phase materials.

This work was supported by the National Science Foundation and the Army Research Office.

References

1. C. B. Burckhardt, J. Opt. Soc. Am. **56,** 1502 (1966).
2. H. Kogelnik, Bell Syst. Tech. J. **48,** 2909 (1969).
3. Y. Ninomiya, J. Opt. Soc. Am. **63,** 1124 (1973).
4. R. Magnusson and T. K. Gaylord, J. Appl. Phys. **47,** 190 (1976).
5. D. Kermisch, J. Opt. Soc. Am. **61,** 1202 (1971).
6. W. J. Tomlinson, Appl. Opt. **14,** 2456 (1975).
7. G. A. Alphonse, R. C. Alig, D. L. Staebler, and W. Phillips, RCA Rev. **36,** 213 (1975).
8. S. F. Su and T. K. Gaylord, J. Appl. Phys. **46,** 5208 (1975).
9. S. F. Su and T. K. Gaylord, J. Appl. Phys. **47,** 2757 (1976).
10. D. L. Staehler and J. J. Amodei, J. Appl. Phys. **43,** 1042 (1972).
11. J. J. Amodei and D. L. Staebler, RCA Rev. **33,** 71 (1972).
12. D. W. Vahey, J. Appl. Phys. **46,** 3510 (1975).
13. L. Young, W. K. Y. Wong, M. L. W. Thewalt, and W. D. Cornish, Appl. Phys. Lett. **24,** 264 (1974).
14. R. Magnusson, Ph.D. Thesis, Georgia Institute of Technology (1976).
15. The finding reported here that the intensity inequality of the incident writing beams indeed has significant effects on thick hologram behavior seems to be in contradiction with a statement by Ninomiya[3] that the intensity ratio of the incident beams does not influence unslanted transmission holograms.
16. D. Kermisch, J. Opt. Soc. Am. **59,** 1409 (1969).
17. N. Uchida, J. Opt. Soc. Am. **63,** 280 (1973).
18. From a theoretical point of view, it is interesting to note that H. Kogelnik, Bell Syst. Tech. J. **55,** 109 (1976), in analyzing Bragg filtering of structures with nonuniform coupling coefficients and period in the direction of propagation, obtains similar sidelobe obliteration (in his reflectivity function) for (linear) nonuniformity in the coupling coefficient and asymmetric behavior relative to the Bragg frequency for (quadratic) nonuniformity in the period.

VI. INSTRUMENTATION

Electronic system for optical shutter control

H. C. Viljoen and T. K. Gaylord

School of Electrical Engineering, Georgia Institute of Technology, Atlanta, Georgia 30332

(Received 22 March 1976)

A versatile electronic system for accurate shutter control in optical experiments is described in detail. Digital and analog circuitry is used to provide automatic timing, exposure control, manual operation, and remote programmability.

I. INTRODUCTION

The accurate control of light beams is of fundamental importance in optical experiments. This is true for virtually all areas of optics. Experiments involving photography or holography are typical examples.

It is desirable to be able with precision to turn on and to turn off laser beams or other light beams in a controlled manner. This includes remote manual control of shutters as well as automatic timing and automatic exposure control. Further, it is frequently necessary to have (1) a relatively large-aperture ($\simeq$50 mm) shutter, (2) high-accuracy timing (error $<0.5\%$), (3) a large range of exposure times (10^{-3}–10^{4} sec), (4) high-accuracy exposure energy control (error $<0.5\%$), and (5) a wide range of total exposure energies (six orders of magnitude). The lack of commercial systems with all of these features provided the motivation for the present work.[1,2]

II. FUNCTIONAL CHARACTERISTICS

The front and rear panels of the electronic shutter system are shown in Fig. 1. As indicated by the OPERATING MODE[3] selection switch, there are four modes of operation and a safety (SHUTTER CLOSED) position. These modes and their functional characteristics are as follows:

(1) TIMER. The open time of the shutter is selected and controlled in this mode. The desired shutter time (from 0.01×10^{-1} to 9.99×10^{3} sec) is preset with the TIMER SET thumbwheel switch. The shutter is opened and the timing sequence begun by depressing the START pushbutton. The elapsed time during the exposure is continuously displayed on a three-digit LED readout. The shutter automatically closes when the preset time has elapsed. The final time (in agreement with the set time) remains displayed until the RESET pushbutton is depressed. If the shutter is closed by pushing the STOP button before the preset time is reached, the elapsed shutter time at the moment of shutter closing remains displayed. The exposure can then be continued by re-pushing the START button. The timing will continue from the previously displayed elapsed time. The elapsed time can be set to zero at any time with the RESET button.

(2) EXPOSURE. The exposure energy is selected and controlled in this mode of operation. An external power meter is used to monitor the optical intensity and to provide a low-impedance voltage signal for the electronic shutter system. The desired exposure energy (from 001 to 999×10^{3} in arbitrary energy units) is preset with the EXPOSURE SET thumbwheel switch. When the START pushbutton is depressed, the shutter opens and the monitor voltage level is integrated over time by the electronic system to give the accumulated exposure energy. This is displayed on a three-digit LED readout. The shutter automatically closes when the preset exposure energy has been reached, and the final exposure energy remains displayed until the RESET pushbutton is depressed. In the EXPOSURE mode, the elapsed time is also simultaneously displayed on the TIME readout. As in the TIMER mode, the STOP pushbutton may be depressed during the exposure causing the shutter to close and the integration process to be interrupted. Both the accumulated exposure energy and the elapsed time remain displayed on the readouts until either the exposure is continued (by pushing START) or the readouts are set to zero (by pushing RESET).

(3) MANUAL. In this mode the shutter is opened by depressing the START pushbutton (as in the other modes). It remains open until the STOP pushbutton is depressed. This is identical to the time mode on a camera. In the MANUAL operating mode with the shutter open the timer starts and operates continuously with the elapsed time being displayed on the TIME readout.

(4) BULB. In this operating mode, the shutter may be opened by depressing the START pushbutton and keeping it depressed. When the START pushbutton is released, the shutter closes. This is the same as bulb operation on cameras. When the shutter is open, the timer operates and the elapsed time continually changes and is displayed on the TIME readout. When the shutter is closed (by releasing the START pushbutton), the accumulated elapsed time is displayed.

In addition to the basic operating functions, a number of convenience features are incorporated in the front panel. These include a green LED to indicate when the shutter is closed and a red LED to indicate when the shutter is open. Another red LED is illuminated when the shutter cannot achieve full aperture owing to the setting of an exposure time that is too short for the particular shutter being used. This will depend on the type of shutter being used and is typically in the

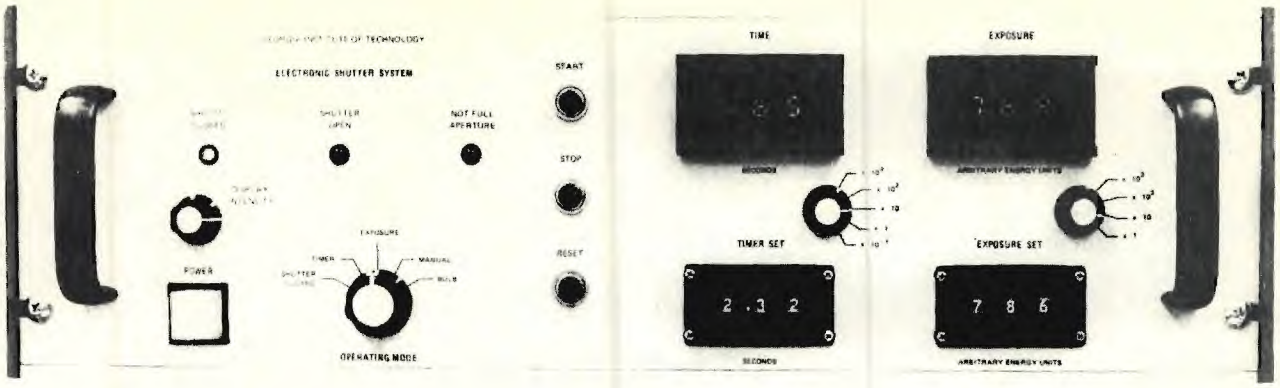

FRONT PANEL

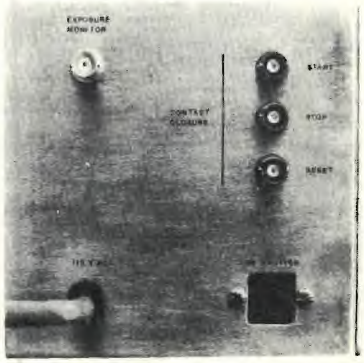

REAR PANEL

FIG. 1. Front and rear panels of electronic instrument for optical shutter control.

range from 1 to 50 msec for most solenoid-operated mechanical shutters. The exposure time setting below which the aperture warning light is illuminated is set with a series of miniature switches in the interior of the instrument. This preset warning point is then manually changed each time the shutter is changed.

A DISPLAY INTENSITY adjustment is also available on the front panel. This allows all display and lamp intensities to be varied uniformly and simultaneously from full brightness to completely off. This permits elimination of instrument light for experiments requiring subdued lighting or complete darkness.

The connectors for attaching external equipment to the shutter system electronics are provided on the rear panel. The output shutter drive signal is obtained from the TO SHUTTER connector. The input optical power level signal (when instrument is used in the EXPOSURE mode) is applied to the EXPOSURE MONITOR connector. Remote external control inputs (through contact closure to ground) for the START, STOP, and RESET functions are connected through three BNC connectors similarly labeled on the rear panel. This allows external programmability of the instrument's functions.

III. ELECTRICAL BLOCK DIAGRAM

A block diagram of the shutter system is shown in Fig. 2. In the exposure mode, the voltage from an external optical power meter is integrated by an exposure circuit to yield energy. The energy level is displayed on a front panel readout. The method of monitoring the optical beam may be with a beam splitter as shown in Fig. 2 or by other placement of the optical power meter sensor.

The control electronics provide switching between various operating modes, activation of the appropriate displays, and signaling of the shutter drive circuit indicating when the shutter is to be opened and when it is to be closed. The shutter drive circuit provides a voltage step to drive the shutter solenoid open. When the voltage is removed, the mechanical restoring springs in the solenoid force the shutter closed. The shutter drive circuit is on a separate printed circuit card to allow the changing of this circuit for use of the instrument with a variety of shutters. Required solenoid drive voltages from the shutter drive circuit are typically in the range 10–100 V for mechanical shutters.[4]

For accurate timing (in the TIMER, EXPOSURE, MANUAL, and BULB modes) a 100.000-kHz quartz crystal clock is used. By using decade counters the elapsed time may then be displayed in 1-msec to 10-sec steps.

IV. INDIVIDUAL CIRCUITS

Six basic circuits were used in the construction of this electronic system for shutter control: (1) timer-control circuit, (2) clock-control circuit, (3) comparator circuit, (4) integration circuit, (5) shutter drive circuit, and (6) power supply circuit. Each of these circuits was fabricated on a separate printed circuit card. The detailed electrical schematics for these circuits (with the exception of the power supply circuit) are presented in Figs. 3–6.

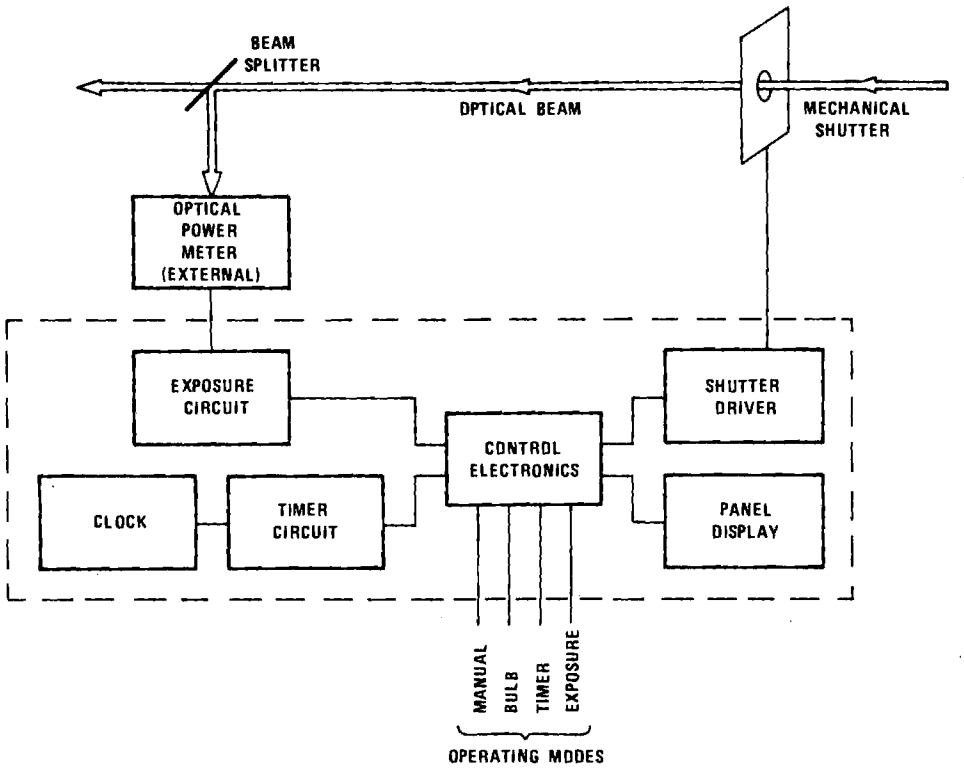

FIG. 2. Block diagram of electronic system for shutter control.

The operation of each circuit may be described as follows.

A. Timer-control circuit

The timer-control circuit is shown in Fig. 3. It contains the TTL logic circuits necessary to generate the different logical signals required for the various operating modes of the instrument. All logical operations are activated by three control pushbutton switches, labeled START, STOP, and RESET, mounted on the front panel. The functional operation of each part of the circuit for the different operating modes is as follows:

(1) BULB. An inverting amplifier [obtained by tying together the two inputs on pins 4 and 5 of the quadruple 2-input type 7400 NAND gate (A10)] inverts the signal from the START switch to give a positive output signal (from pin 6 of A10) whenever this switch is operated. This signal is used to drive the shutter drive circuit when the function selector OPERATING MODE switch is in the BULB position. This causes the shutter to remain open as long as the START switch is depressed.

(2) MANUAL. The START switch is also used to set a latching flip-flop (causing pin 8 of A3 to go high, i.e., logical one or +5 V level), formed by cross-connecting two NAND gates (A3) to eliminate contact bounce on the pushbutton switches. This latching flip-flop can be reset (causing pin 11 of A3 to go high) by operating the STOP switch. The output from pin 8 of A3 will alternate between the logical one (+5 V) and logical zero (0 V) levels by consecutively operating the START and STOP pushbutton switches, and is fed to the shutter drive board via the function selector OPERATING MODE switch whenever it is in the MANUAL position, opening the shutter after operating the START switch, and closing the shutter after operating the STOP switch.

(3) TIMER. A second latching flip-flop is formed by the remaining two NAND gates of A3, the output of which (pins 3 and 6 of A3) directly drives the *J-K* input terminal (pins 16 and 4) of the *J-K* flip-flop (A6). The second latching flip-flop (A3) can be set by pressing the START switch (causing pin 6 of A3 to go high), and is reset on its other input by operating the RESET switch. When this flip-flop is set, the *J-K* flip-flop (A6) will transfer its input state to the output when the next clock pulse from the time base goes negative, causing the shutter drive signal (pin 4 on A9) to go high. This will cause the shutter to open at the beginning of a clock pulse period when the function selector OPERATING MODE switch is in the TIMER position. Simultaneously, the time base pulses will be fed to pin 1 of A9 for counting by the three-decade counters on the clock-control board (see Fig. 4), as well as to the three type 74192 up/down counters A1, A4, and A5 of the timer-control circuit.

Should the STOP pushbutton switch be operated before the end of any operating sequence, the first latching flip-flop (pin 8 of A3) will be reset, causing the *J-K* flip-flop of A3 to reset, closing the shutter and disabling the clock pulses being fed to pin 1 of A9 and to pin 4 of A1. The operating sequence can be resumed by depressing the START switch again.

The above circuitry is in operation during all modes

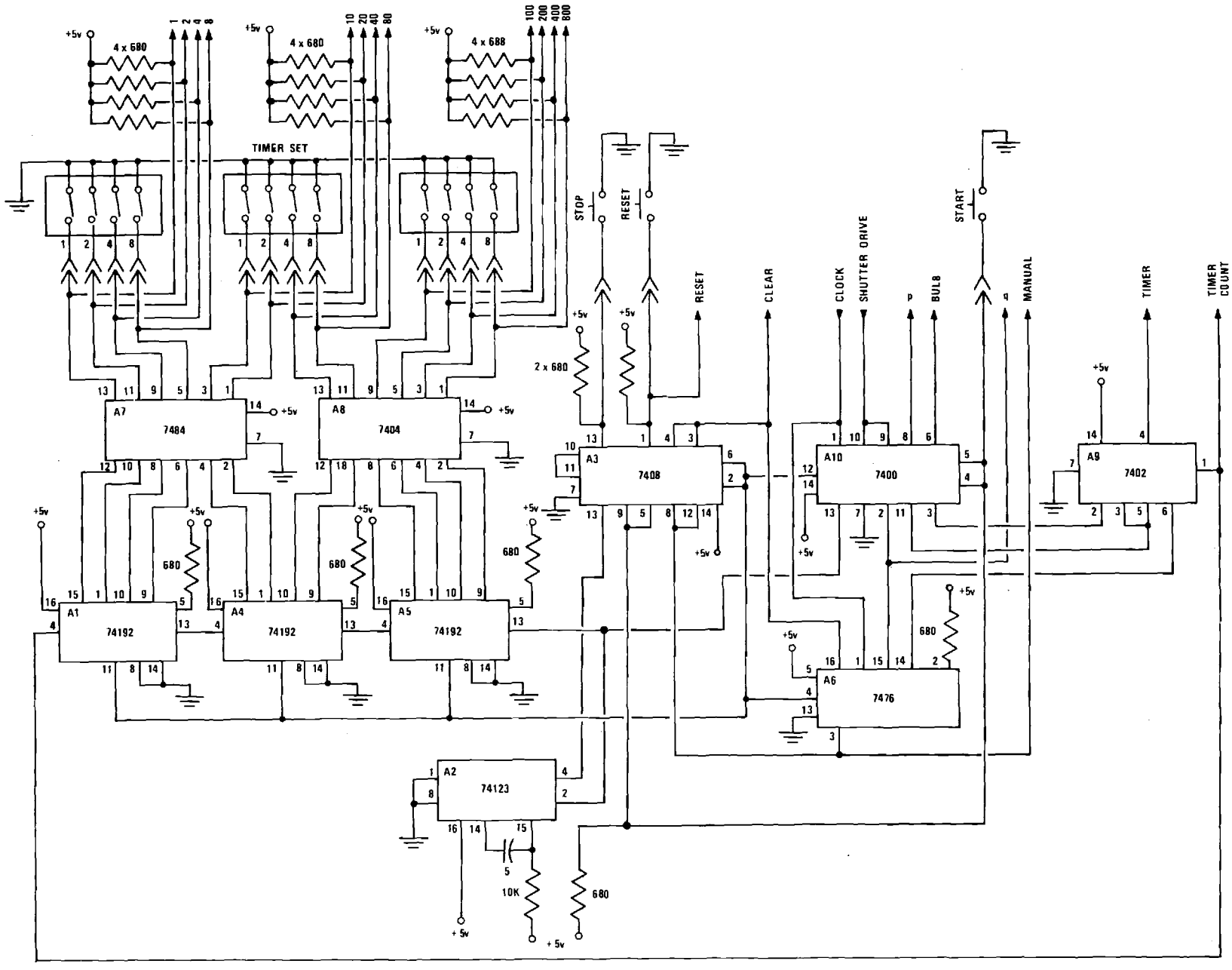

FIG. 3. Timer-control circuit of electronic system for optical shutter control. Here and in the rest of the diagrams all resistance values are in ohms and capacitance values are in μF. All resistors are of the 0.25-W, 5%, composition type.

of operation of the instrument, allowing the time during which the shutter is open to be measured accurately and displayed.

In the TIMER mode the TIMER SET binary coded decimal (BCD) thumbwheel switches preset (via the type 7404 inverting amplifiers A7 and A8) the type 74192 up/down counters A1, A4, and A5 to the desired count. This happens while the load input terminal (pin 11 of A1, A4, and A5, driven from the second latching flip-flop A3) is low, i.e., after operating the RESET switch. Upon operating the START switch, the countdown sequence is initiated by feeding the clock pulses from pin 1 of A9 to the countdown input (pin 4) of A1. At the same time the borrow output (pin 13) of A5 goes high during the entire countdown period, causing the shutter to open when the OPERATING MODE switch is in the TIMER position. Should the STOP switch be activated before countdown is completed, the countdown sequence is interrupted by resetting the first latching flip-flop of A3 (pin 8 of A3), which in turn causes the clock pulses fed through to pin 1 of A9 to be interrupted, and closing the shutter. The sequence can be resumed by again setting the first latching flip-flop (A3) by depressing the START switch.

When the up/down counters A1, A4, and A5 have counted down to zero, the borrow output (pin 13 of A5) goes low, thus resetting the first latching flip-flop via the monostable multivibrator A2, and closing the shutter. The up/down counters can be reactivated only after operating the RESET switch, which will cause the second latching flip-flop of A3 to reset (pin 6 of A3 goes low), causing the voltage on pins 11 of A1, A4, and A5 to go low, so as to enable the counters to be loaded again by the thumbwheel-switch setting.

The complementary output from the second latching flip-flop (pin 3 of A3), which goes high when operating the RESET switch, is also used to reset the clock (refer to Fig. 4) to zero whenever the RESET switch is operated.

B. Clock-control circuit

The clock-control circuit is shown in Fig. 4. A self-starting crystal-controlled Colpitts oscillator generates a 100-kHz square wave that is divided by a series of six type 7490 decade dividers (A1 to A6) to generate clock frequencies of 1 kHz to 0.1 Hz, the correct clock frequency being selected by the TIMER SET selector switch. After being gated by the timer-control circuitry (see Fig. 3), the number of clock pulses occurring during the time the shutter is activated is counted by three type 7490 decade counters (A7, A8, and A9) in all modes of operation of the instrument. The timer count is displayed on three LED 7-segment display devices. A decimal point after the most significant digit is permanently displayed, allowing the shutter opening time to be indicated in scientific notation (with the decimal multiplier indicated by the range switch).

The decade counters are reset to zero whenever the RESET switch is depressed. However, operating the STOP switch to interrupt any operating sequence will close the shutter, thus stopping the clock pulses fed to the decade counters A7 to A9, but does not reset these counters to zero. When the START switch is again operated, the operation will proceed (adding elapsed time to the previous count).

C. Comparator circuit

The comparator circuit (also shown in Fig. 4) consists of two cascaded pairs of type 7485 magnitude comparators (A13 and A14 for the $\times 1$ range, and A15 and A16 for the $\times 10^{-1}$ range), which compares the TIMER SET thumbwheel setting with a preset binary number on internal miniature switches. The most significant digit of the TIMER SET switch is monitored by a simple four-diode AND circuit, being activated by a zero digit. On the two highest frequency ranges of the range switch ($\times 10^{-1}$ and $\times 1$), the output of the corresponding two comparator ICs will go low whenever the thumbwheel setting is less than the preset setting on the miniature switches, causing the NOT FULL APERTURE warning LED light to be illuminated. The preset switches have to be reset each time a new type of shutter is used with the instrument by setting the switches to correspond with the time required to open the shutter fully after application of a drive pulse.

D. Exposure (integrator) circuit

The integrator circuit is shown in Fig. 5. It is a precision type LM308 op amp (A11) with a low-leakage 4-μF integrating capacitor. The integrating time constant can be varied over four decades by the exposure multiplier switch. This effective variation is obtained by a resistor divider network which offers a constant total resistance of 10 kΩ to the integrating op amp (to minimize offset drift when changing ranges) for a signal from a low-impedance input source (optical power meter).

The offset bias compensating trimpot RV1 is adjusted to eliminate any tendency of the integrator output to drift when the input is zero. In the EXPOSURE mode the integrator's input will be switched by relay RLY1 (activated by operating the START switch) from ground (0 V) to the signal to be integrated; operating the STOP switch will cause RLY1 to be deactivated, returning the integrator input to ground level (i.e., causing the integrator's output voltage to "hold"). Operating the RESET switch will activate relay RLY2, which effectively shorts the integrating capacitor through a 100-Ω resistor, discharging the voltage across it to zero.

With a positive input voltage to the integrator op amp, its output voltage will decrease (i.e., go negative) in proportion to the time integral of the input voltage. The output voltage of the integrator is measured by a digital voltmeter consisting of a precision voltage-to-frequency converter (A13 and A14) and three decade

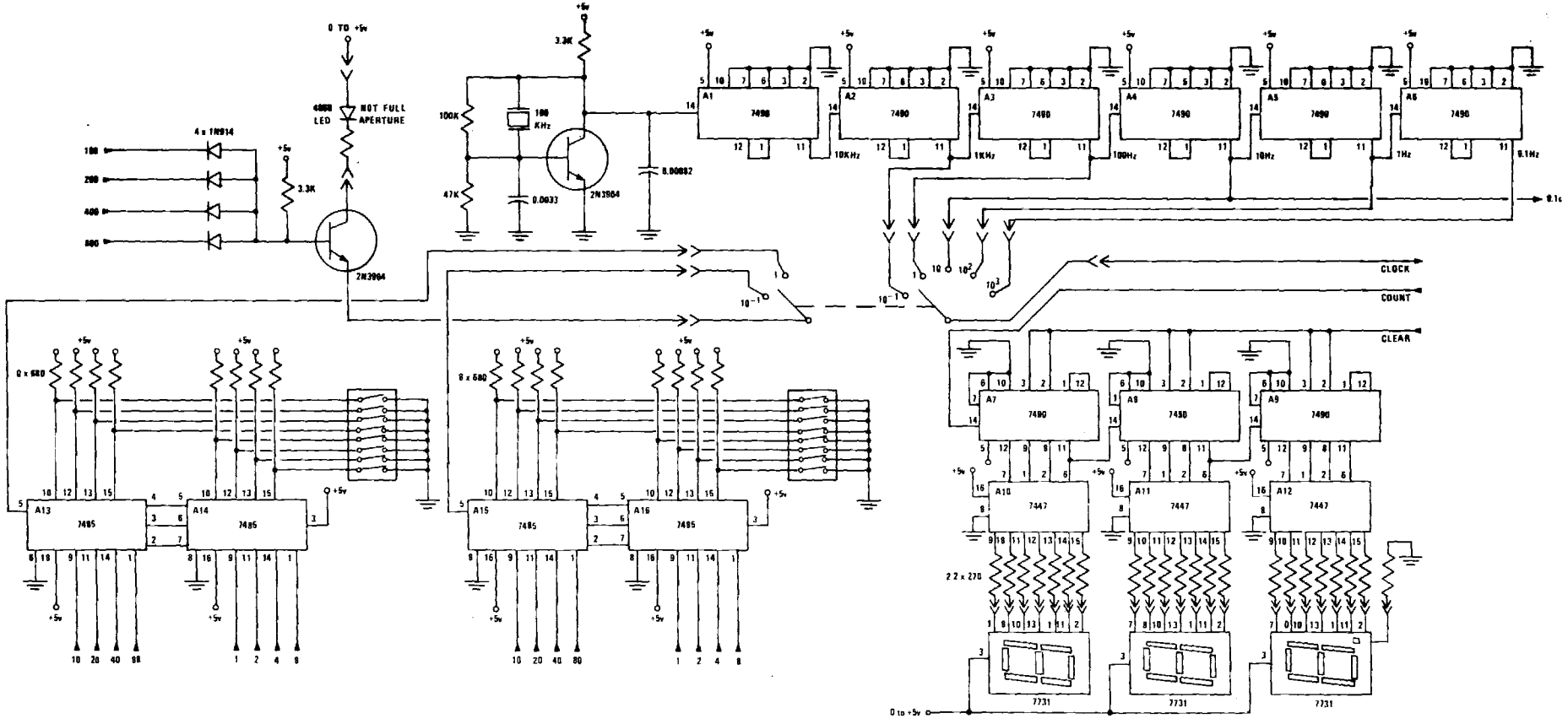

FIG. 4. Clock-control and comparator circuits of the electronic system for optical shutter control.

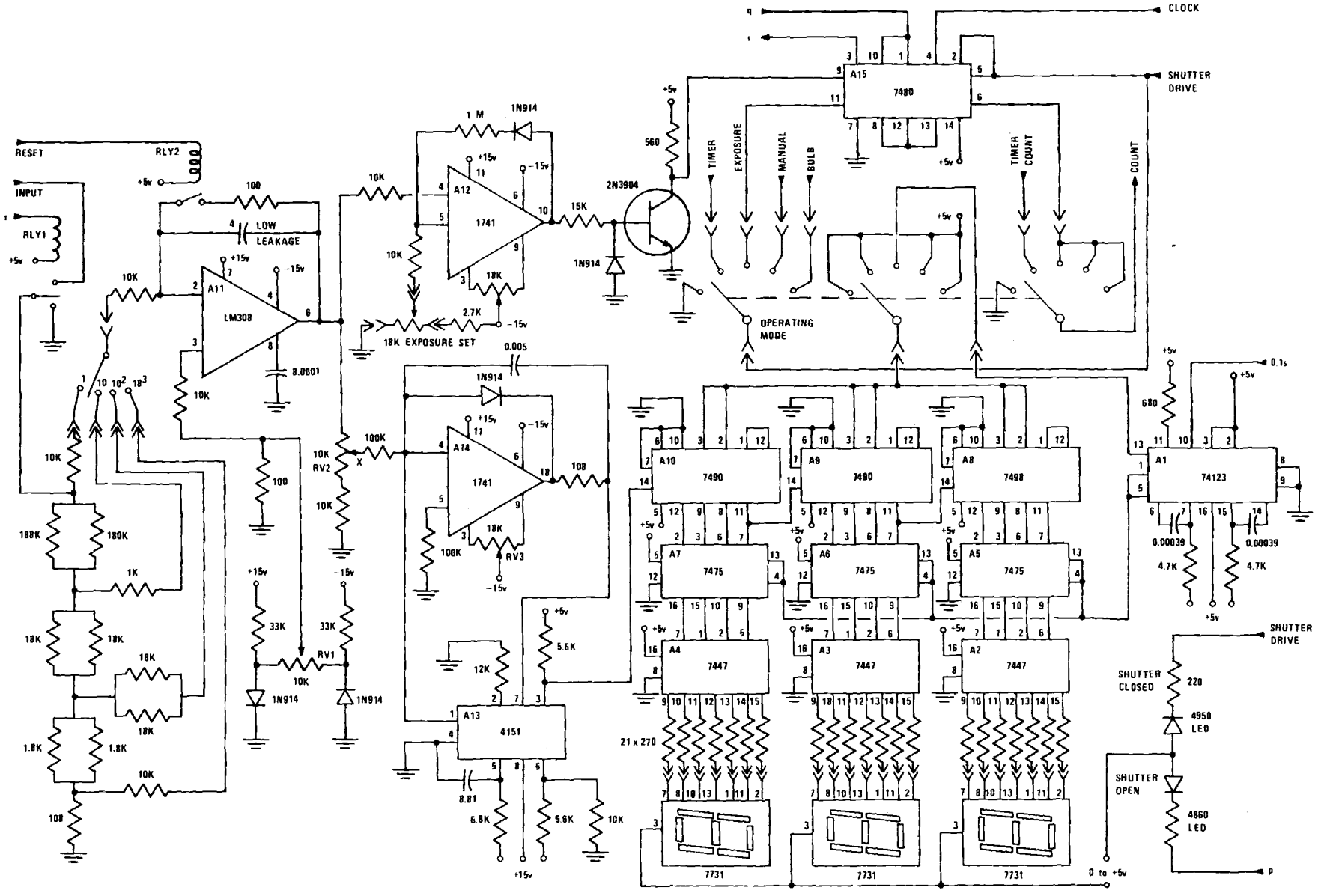

FIG. 5. Integration (exposure) circuit of the electronic system for optical shutter control.

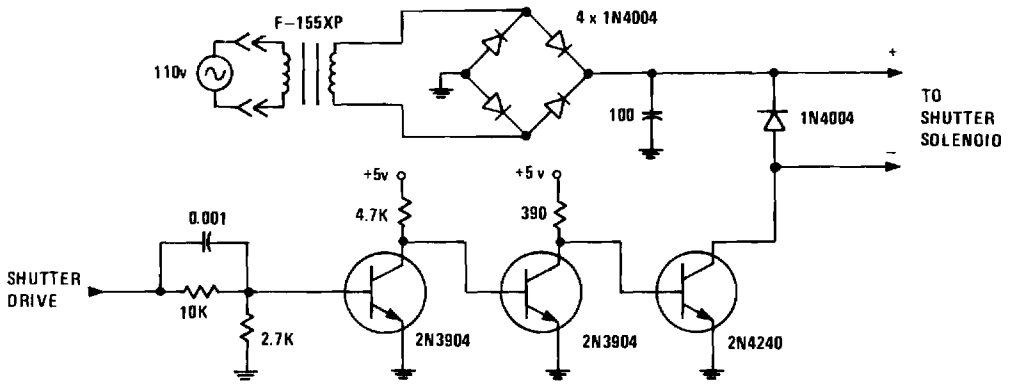

FIG. 6. Shutter drive circuit (for operating a single shutter) of the electronic system for optical shutter control.

counters (A8, A9, and A10). The voltage-to-frequency converter will give an output frequency of 0–10 kHz, with a linearity of better than 0.05%, when its input voltage (point marked X on Fig. 5) varies from 0 to −10 V.[5,6]

The output of the voltage-to-frequency converter (pin 3 on A13) is counted by a three-decade counter (A8, A9, and A10). Every 100 msec the count is latched into the bistable latches A5, A6, and A7 by a latch pulse of 0.8-μsec duration generated by the first monostable multivibrator of A1, which in turn is fed with a 10-Hz clock drive signal. Immediately following the latch pulse from A1, a reset pulse of 0.8 μsec from the second monostable multivibrator of A1 is used to reset the three-decade counters A8, A9, and A10 to zero. The latched count in A5, A6, and A7 is displayed on the three 7-segment LEDs, which are therefore updated ten times per second to indicate the integrator output voltage (EXPOSURE). This counter is activated only in the EXPOSURE mode.

The trimpot RV2 determines the full-scale calibration of the digital voltmeter EXPOSURE display and is set to ensure that the indicated count agrees with the setting on the EXPOSURE SET thumbwheel switches at the end of an integration operation. During calibration RV2 is adjusted to ensure agreement between the two at the high end of the scale, while RV3 is adjusted to ensure that the output frequency of the voltage-to-frequency convertor is zero when the integrator's output voltage is zero.

The output voltage of the integrator is also fed to the inverting input terminal of the level detector op amp A12, which switches when the integrator's output voltage equals the reference voltage (on the noninverting input) from the slider of the EXPOSURE SET three-decade thumbwheel voltage divider. When this happens, the shutter will close if the OPERATING MODE switch is in the EXPOSURE position. Since the integrator saturates at an output voltage of approximately −13 V, the reference voltage from the EXPOSURE SET voltage divider is limited to a value of less than −13 V by a 2.7-kΩ resistor connected in series with the top end of the voltage divider and the −15-V supply. A 1-MΩ resistor between the output of the level detector op amp A12 and its noninverting input ensures a small amount of hysteresis to prevent jitter on the shutter when it closes.

Should the integrator drift at the end of an integration operation, readjustment of RV1 is required. Drift, if present, can be observed on the EXPOSURE readout. In any case, it is desirable to operate the STOP switch when the shutter closes at the end of an integration run, to prevent reactivating the shutter in the presence of any residual long-term drift on the integrator. The use of a common grounding point for all integrator components is essential to prevent potential differences around ground loops from being integrated and causing drift in the integrator.

E. Shutter drive circuit

The shutter drive circuit is shown in Fig. 6. It consists of a two-stage direct coupled low-level transistor amplifier feeding a type 2N4240 driver power transistor, which is connected to the shutter solenoid. The dc voltage required by the output stage of the shutter drive will be determined by the type of shutter[7] used. The power dissipation of the power output transistor in the saturated "on" mode (shutter open) is small enough for most shutter currents not to require a heat sink, even for prolonged operation. The shutter is activated by a +5-V signal to the drive circuit.

V. DISCUSSION

The electronic instrument for optical shutter control described here was designed to have maximum accuracy and versatility. No commercial instrument exists with similar functional and accuracy characteristics. The basic electronic system is independent of the type of dc-driven shutter used. By changing a single printed circuit board (shutter drive circuit) any such shutter can be operated and controlled by this instrument. In fact, multiple shutters can be controlled by a single instrument. As an example, two spring-loaded shutters may be placed in series along a single light beam to provide shorter exposure times than are possible by a single shutter of the same type. One shutter that is initially closed is driven open at the beginning of the shutter drive pulse while a second shutter that is initially open is driven closed at the end of the shutter drive pulse. This allows the mechanical shutter blades each to be accelerated in only one direction, thus decreasing the exposure time possible with the system.

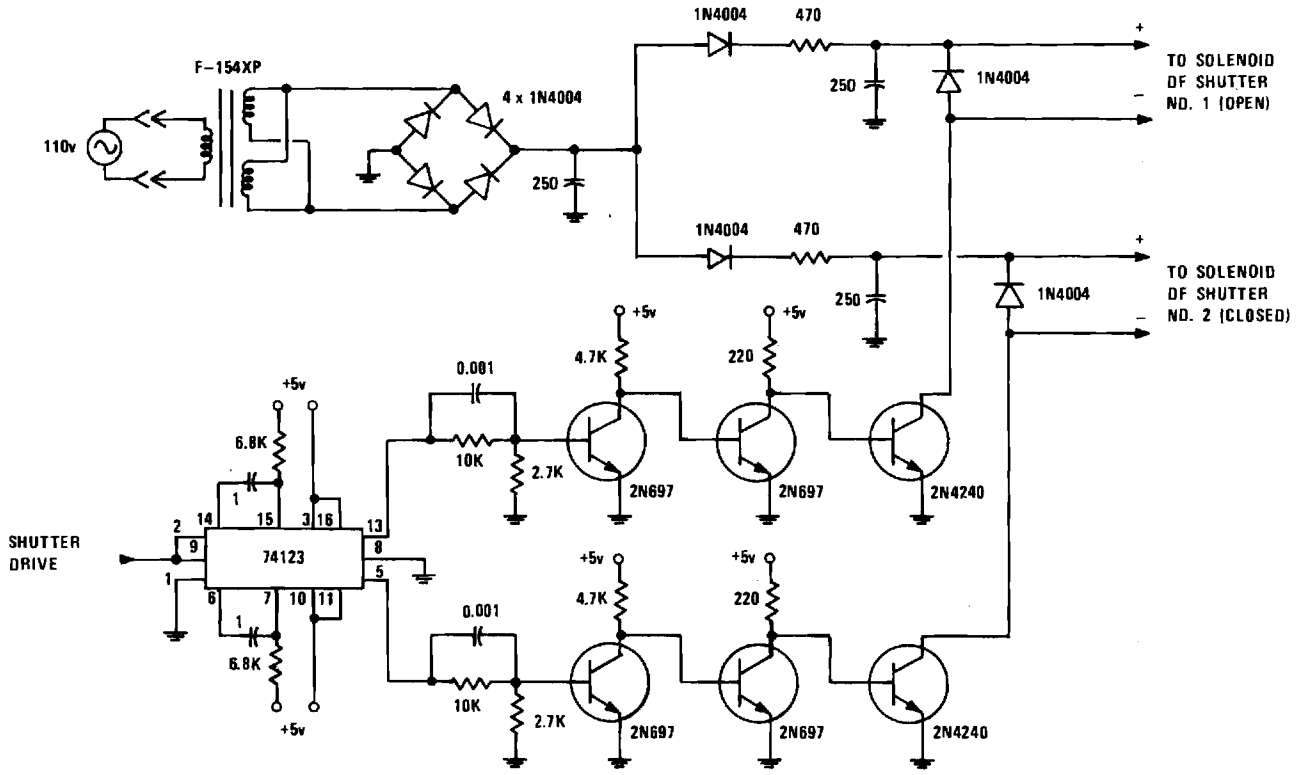

FIG. 7. Alternate shutter drive circuit for use in operating two shutters configured back to back. One shutter that is initially closed is triggered to open and the second shutter that is initially open is triggered to closed. This allows the minimum exposure time at full aperture to be as short as 1.5 msec for the shutters used here.

The circuit used to accomplish this is shown in Fig. 7. With it, a full aperture exposure time of 1.5 msec was achieved.

This shutter-control instrument was designed to use only the most readily available standard preferred values and types of electronic components. No unusual or uncommon components were used. The total cost of the components (excluding power meter and shutter) is about $350 based on present small-quantity prices. In addition, the design was formulated to produce minimum sensitivity to component tolerances. For example, all resistance values have a ±5% tolerance, the oscillator has assured self-starting characteristics, etc.

The instrument allows maximum use of normally existing peripheral equipment. For example, any optical meter can be used to provide a power monitoring signal. The monitor voltage level can be anywhere from about 10 mV to 50 V.

Power requirements for the instrument are +5 V (regulated) at 1.5 A, and +15 and −15 V (both regulated) at 20 mA, and 0–5 V (adjustable) at 600 mA. The high-voltage dc supply of the shutter drive circuit is determined by the type of shutter used. The complete instrument dissipates a total electrical power of about 20 W.

ACKNOWLEDGMENTS

The authors gratefully acknowledge the technical assistance of R. T. Beason, P. G. Branson, and J. A. Maynard during the design and construction of this equipment. This work was supported by the National Science Foundation under Grant No. ENG75-14456 and by the National Aeronautics and Space Administration under Grant No. NAS8-30246.

[1] For example, electronic instruments for exposure (optical energy) control of shutters are available from American Optical Corp., Buffalo, NY 14215.

[2] For example, electronic instruments for timing control of shutters are available from Newport Research Corp., Fountain Valley, CA 92708; Ilex Optical Co., Rochester, NY 14621; and Vincent Associates, Rochester, NY 14607.

[3] Words in small capitals are used throughout this paper to indicate a switch, a display, or a connector on the front or rear panels of the instrument.

[4] For example, solenoid-driven mechanical shutters are available from Electronic Mechanical Products Co., Atlantic City, NJ 08404; Vincent Associates, Rochester, NY 14607, and Herbach and Rademan, Inc., Philadelphia, PA 19134.

[5] B. Cole, Electronics **48**, 112 (21 August 1975).

[6] See *Linear Integrated Circuit Product Specifications, Voltage-to-Frequency Converter, October 1975* (available from Raytheon Semiconductor Division, Mountain View, CA 94042).

[7] In the construction of several units, the authors modified ac-operated shutters for dc operation by removing the bridge rectifier and the resistor–capacitor filter.

VII. PERSONNEL

BIOGRAPHICAL SKETCH

GAYLORD, THOMAS K. - Associate Professor of Electrical Engineering
Georgia Institute of Technology

EDUCATION

B.S. in Physics, University of Missouri-Rolla	1965
M.S. in E.E., University of Missouri-Rolla	1967
Ph.D. in E.E., Rice University	1970

EMPLOYMENT HISTORY

Western Electric Company (Kansas City, Missouri)	1964-1965
Special Technical Assistant	
Rice University	
Post Doctoral Fellow	1970
Research Associate	1971
Adjunct Assistant Professor of Electrical Engineering	1972
Georgia Institute of Technology	
Assistant Professor of Electrical Engineering	1972-1976
Associate Professor of Electrical Engineering	1976-Present

EXPERIENCE SUMMARY

At Western Electric Company, was engaged in solid state device and materials research (silicon alloy diode and thermistors). At Rice University, was engaged in research on high electric field effects in semiconductors, microelectronics, switching phenomena in semiconductor devices, optical recording of information in crystals, and development of new instrumentation techniques. At Georgia Tech, engaged in optical holographic recording in crystals, optical information processing, optical memories, semiconductor devices, microelectronics, and instrumentation. Teaching activities in the areas of solid state, optics, electromagnetics, and circuit analysis.

CURRENT FIELDS OF INTEREST

Optical holographic information storage, optical properties of solids, optical memory implementation, semiconductor materials and devices, microelectronics, and instrumentation techniques.

ENGINEERING CONSULTING

Rice University (optics instrumentation)
Vector Cable Company (electromagnetics)
Engineering and Scientific Consultants (solid state device modeling)
Western Electric Company (microelectronics instrumentation)
Modern Optics (optics instrumentation)
Spectra Physics (optics instrumentation)
Hewlett-Packard (electronics instrumentation)
Optical Publishing Company (optics technology)

TECHNICAL SOCIETIES

Sigma Pi Sigma, Tau Beta Pi, Kappa Mu Epsilon, Phi Kappa Phi, Sigma Xi (full member), Eta Kappa Nu, AAAS, AAUP, AIP, IEEE, and OSA.

PROFESSIONAL ENGINEER REGISTRATION

Missouri (EIT-12866-E)
Texas (PE-33921)

PUBLICATIONS

1. Lyon, D. H., and Gaylord T. K., "An electro-mechanical effect in the silicon alloy diode," American Physical Society meeting, Kansas City, Mo., March 1965, Bull. Am. Phy. Soc., vol. 10, no. 5, pg. 599, June 1965.

2. Gaylord, T. K., Shah, P. L., and Rabson, T. A., "Gunn effect bibliography," IEEE Trans. on Electron Devices, vol. ED-15, no. 10, pp. 777-778, October 1968.

3. Gaylord, T. K., "An engineer's obligation to society," The Rice Engineer, vol. 17, no. 2, pp. 13-21, Winter 1968.

4. Gaylord, T. K., Shah, P. L., and Rabson, T. A., "Gunn effect bibliography supplement," IEEE Trans. on Electron Devices, vol. ED-16, no. 5, pp. 490-494, May 1969.

5. Gaylord, T. K. and Rabson, T. A., "A method for estimating the location of energy minima near the Brillouin zone boundary and its application to gallium arsenide," Physics Letters, vol. 29A, no. 11, pp. 716-717, August 25, 1969.

6. Gaylord, T. K., "High electric field conduction anisotropies in semiconductors," (Ph.D. thesis, Rice University, 1970), Dissertation Abstracts International, vol. 31, no. 6, pp. 3393-B, December 1970.

PUBLICATIONS (continued)

7. Gaylord, T. K. and Rabson, T. A., "Anisotropy in the conductivity of gallium arsenide," Physics Letters, vol. 33A, no. 2, pp. 95-96, October 5, 1970.

8. Gaylord, T. K. and Rabson, T. A., and Tittel, F. K., "Optically erasable and rewritable solid state holograms," Applied Physics Letters, vol. 20, no. 1, pp. 47-49, January 1, 1972.

9. Gaylord, T. K. and Rabson, T. A., "On the possibility of transverse negative differential conductivity in semiconductors," Physics Letters, vol. 38A, no. 7, pp. 493-494, March 27, 1972.

10. Gaylord, T. K., "Microelectronics," Rice University Review, vol. 7, no. 2, pp. 10-13, Summer 1972.

11. Gaylord, T. K. and Rabson, T. A., "Determination of conduction anisotropies in semiconductors," Solid State Electronics, vol. 15, no. 9, pp. 953-960, September 1972.

12. Gaylord, T. K., "A laboratory photomask production facility," Review of Scientific Instruments, vol. 43, no. 9, pp. 1268-1271, September 1972.

13. Gaylord, T. K., "The high capacity storage problem: Is optical holography the answer?" Optical Spectra, vol. 6, no. 11, pp. 25-37, November 1972.

14. Gaylord, T. K., Rabson, T. A., Tittel, F. K., and Quick, C. R., "Self-enhancement of $LiNbO_3$ holograms," Journal of Applied Physics, vol. 44, no. 2, pp. 896-897, February 1973.

15. Gaylord, T. K., Rabson, T. A., Tittel, F. K., and Quick, C. R., "Pulsed writing of solid state holograms," Applied Optics, vol. 12, no. 2, pp. 414-415, February 1973.

16. Gaylord, T. K., "An economical microelectronics laboratory," Microelectronics, vol. 5, no. 1, pp. 3-11, Autum 1973.

17. Gaylord, T. K. and Tittel, F. K., "Angular selectivity of lithium niobate volume holograms," Journal of Applied Physics, vol. 44, no. 9, pp. 4771-4773, September 1973.

18. Harman, T. L., Gaylord, T. K., and Rabson, T. A., "Effects of intrinsic region width in Si(Li) p-i-n diodes," Solid State Electronics, vol. 17, no. 4, pp. 408-411, April 1974.

19. Gaylord, T. K. (editor), 1974 IEEE S-MIT International Microwave Symposium Digest of Technical Papers, Atlanta: IEEE, 1974.

PUBLICATIONS (continued)

20. Shah, P., Rabson, T. A., Tittel, F. K., and Gaylord, T. K., "Volume holographic recording and storage in Fe-doped $LiNbO_3$ using optical pulses," Applied Physics Letters, vol. 24, no. 3, pp. 130-131, February 1, 1974.

21. Magnusson, R., and Gaylord, T. K., "Laser scattering induced holograms in lithium niobate," Applied Optics, vol. 13, no. 7, pp. 1545-1548, July 1974.

22. Gaylord, T. K., "Optical memories," Optical Spectra, vol. 8, no. 6, pp. 29-34, June 1974.

23. Su, S. F. and Gaylord, T. K., "Calculation of arbitrary-order diffraction efficiencies of thick gratings with arbitrary grating shape," Journal of the Optical Society of America, vol. 65, no. 1, pp. 59-64, January 1975.

24. Gaylord, T. K., "Optical memory systems," 1975 Optical Industry and Systems Directory Encyclopedia, Pittsfield, Mass., Optical Publishing Co., pp. 132-136, 1975.

25. Gaylord, T. K., "An undergraduate optical engineering course," IEEE Trans. on Education, vol. E-18, no. 2, pp. 109-112, May 1975.

26. Gaylord, T. K., "Tensor description of physical properties of crystals," American Journal of Physics, vol. 43, no. 10, pp. 861-868, October 1975.

27. Su, S. F. and Gaylord, T. K., "Refractive index profiles and arbitrary-order diffraction efficiencies of lithium niobate holograms," Journal of the Optical Society of America, vol. 65, no. 10, pg. 1220, October 1975.

28. Magnusson, R. and Gaylord, T. K., "Application of dynamic theory to the description of experimental volume holography," Journal of the Optical Society of America, vol. 65, no. 10, pg. 1219, October 1975.

29. Maynard, J. A., Gaylord, T. K., and Rust, J. H., "Data acquisition system for laser Doppler velocimeters," Review of Scientific Instruments, vol. 46, pp. 1469-1473, November 1975.

30. Su, S. F. and Gaylord, T. K., "Unified approach to the formation of phase holograms in ferroelectric crystals," Journal of Applied Physics, vol. 46, pp. 5208-5213, December 1975.

PUBLICATIONS (continued)

31. Gaylord, T. K. and Linxwiler, J. N., "A method for calculating the Fermi energy and the carrier concentrations in semiconductors," American Journal of Physics, vol. 44, pp. 353-356, April 1976.

32. Gaylord, T. K., "Considerations in developing university micro-circuit fabrication laboratories," International Journal of Electrical Engineering Education, vol. 13, pp. 321-325, 1976.

33. Gaylord, T. K., Weaver, J. E., and Callen, W. R., "A mobile, rigid, vibration-isolated optics demonstration platform," American Journal of Physics, vol. 43, pp. 310-311, March 1976.

34. Magnusson, R. and Gaylord, T. K., "Use of dynamic theory to describe experimental results from volume holography," Journal of Applied Physics, vol. 44, pp. 190-199, January 1976.

35. Su, S. F. and Gaylord, T. K., "Determination of physical parameters and processes in hologram formation in ferroelectrics," Journal of Applied Physics, vol. 47, pp. 2757-2758, June 1976.

36. Gaylord, T. K., "Optical memory systems," Optical Industry and Systems Directory Encyclopedia, Pittsfield, Mass., Optical Publishing Co., pp. 198-203, 1976.

37. Gaylord, T. K., Magnusson, R., and Su, S. F., "Volume holographic recording and read-out in ferroelectrics," Journal of the Electro-chemical Society, vol. 123, pg. 116C, March 1976.

38. Su, S. F. and Gaylord, T. K., "Refractive-index profile and physical process determination in thick gratings in electro-optic crystals," Applied Optics, vol. 15, pp. 1947-1952, August 1976.

39. Viljoen, H. C. and Gaylord, T. K., "An electronic system for optical shutter control," Review of Scientific Instruments, vol. 47, pp. 1133-1141, September 1976.

40. Gaylord, T. K., "Optical configurations for close-up and macrophotography of lepidoptera," Lepidopterists' Society News, vol. 18, pp. 1-5, October 15, 1976.

41. Su, S. F. and Gaylord, T. K., "Time evolution and refractive-index profiles of phase holograms in electro-optic crystals," Journal of the Optical Society of America, vol. 66, pg. 1084, October 1976.

42. Magnusson, R. and Gaylord, T. K., "Dynamically-induced refractive-index nonuniformities in electro-optic holographic gratings," Journal of the Optical Society of America, vol. 66, pg. 1084, October 1976.

43. Magnusson, R. and Gaylord, T. K., "Dynamically produced refractive-index variations with thickness of volume holograms in electrooptic crystals," Applied Optics, vol. 15, pp. 3021-3024, December, 1977.

PUBLICATIONS (continued)

44. Gaylord, T. K., Magnusson, R., and Weaver, J. E., "Digital processing capabilities using holographically recorded data pages in electro-optic crystals," Optics Communications, vol. 20, 1977 (to appear).

CONFERENCE PAPERS

1. Lyon, D. H. and Gaylord, T. K., "An unusual electro-mechanical effect in the silicon alloy diode," American Physical Society meeting, Kansas City, Mo., March 1965.

2. Gaylord, T. K., "Research project selection by university engineering faculty," Proceedings of the 1975 IEEE Southeastern Conference, vol. 1, pp. 3B11-3B13, April 1975.

3. Alford, C. O. and Gaylord, T. K., "The potential of multi-port optical memories in digital computing," Digest of 1975 International Optical Computing Conference, pp. 121-123, Washington, D.C., April 1975.

4. Gaylord, T. K. and Linxwiler, J. N., "Computer-aided analysis of semiconductor materials," Proceedings of Fifth Annual Frontiers in Education Conference, pp. 114-117, Atlanta, Georgia, October 20, 1975.

5. Gaylord, T. K., "Macrophotography of lepidoptera in their natural habitat," The Lepidopterists' Society Annual Meeting, University of Massachusetts, August 22, 1975.

INVITED PAPERS

1. Gaylord, T. K., "Research in Optical Storage in Information," Electrical Engineering and Physics Departments, University of Missouri-Rolla, March 6, 1975.

2. Gaylord, T. K., "Dielectrics for Hologram Storage," Electrochemical Society Symposium, May 1976.

3. Gaylord, T. K., "Storage and Processing of Analog and Digital Data Using Solid State Holography," Battelle Columbus Laboratories, December 1976.

EDITORIAL AND REVIEWER WORK FOR TECHNICAL JOURNALS

1. Associate Editor, IEEE Transactions on Education

2. Editorial Advisory Board, Optical Publishing Company

EDITORIAL AND REVIEWER WORK FOR TECHNICAL JOURNALS

3. Reviewer, Journal of the Electrochemical Society

4. Reviewer, IEEE Transactions on Education

5. Reviewer, Optical Spectra

6. Reviewer, Optical Systems Directory and Encyclopedia

7. Reviewer, Applied Optics

8. Reviewer, Journal of the Optical Society of America

HONORS AND AWARDS

Received "Outstanding Young Faculty Research Award" from Sigma Xi, 1976.

Received "Outstanding Teacher Award" from Georgia Tech EE senior class of 1976.

Received "Outstanding Young Engineer of the Year" award for 1977 from the Georgia Society of Professional Engineers.

April 1977